

COMPUTATIONAL PERSPECTIVES ON TRIPLET EXCITON HARVESTING: A COMBINED AB INITIO AND MACHINE LEARNING INVESTIGATION

A Thesis

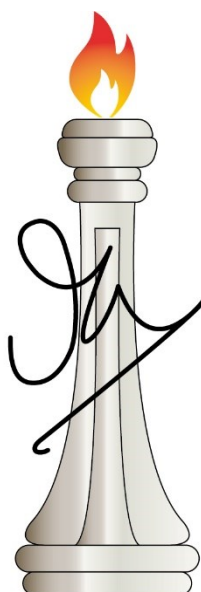
Submitted For the Degree of

DOCTOR OF PHILOSOPHY

In the Faculty of Science

By

BIDHAN CHANDRA GARAIN



J N C A S R

THEORETICAL SCIENCES UNIT (TSU)

JAWAHARLAL NEHRU CENTRE FOR ADVANCED SCIENTIFIC RESEARCH (JNCASR)

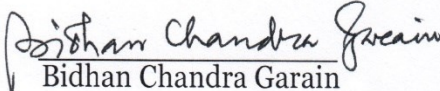
BANGALORE – 560 064, INDIA

MARCH 2023

To My Family and Teachers

Declaration

I hereby declare that the matter embodied in the thesis entitled “***Computational Perspectives on Triplet Exciton Harvesting: A Combined Ab Initio and Machine Learning Investigation***” is the result of investigations carried out by me at the Theoretical Sciences Unit, Jawaharlal Nehru Centre for Advanced Scientific Research, Bangalore, India under the supervision of Prof. Swapan K Pati and that it has not been submitted elsewhere for the award of any degree or diploma. In keeping with the general practice in reporting scientific observations, due acknowledgement has been made whenever the work described is based on the findings of other investigators. Any omission that might have occurred by oversight or error of judgement is regretted.


Bidhan Chandra Garain

Certificate

I hereby certify that the matter embodied in this thesis entitled "***Computational Perspectives on Triplet Exciton Harvesting: A Combined Ab Initio and Machine Learning Investigation***" has been carried out by Mr. Bidhan Chandra Garain at the Theoretical Sciences Unit, Jawaharlal Nehru Centre for Advanced Scientific Research, Bangalore, India under my supervision and that it has not been submitted elsewhere for the award of any degree or diploma.



Prof. Swapan K. Pati
(Research Supervisor)

Acknowledgments

First and foremost, I would like to acknowledge my research supervisor Prof. Swapan K Pati for giving me an opportunity to explore the exciting research area of photochemistry. I am thankful to him for his guidance, support, and encouragement throughout the journey of my Ph.D. career.

I convey my heartfelt gratitude to Prof. C. N. R. Rao for his vision of JNCASR. His presence & speeches are truly very inspiring. I thank all my course instructors in JNCASR for the useful courses.

I am very grateful to my excellent collaborators, Prof. Subi Jacob George, Prof. K. S. Narayan, Dr. Pralok K. Samanta, Dr. Shubhajit Das, Dr. Suman Kuila, Dr. Swadhin Garain.

I would also like to thank all the faculty members of Theoretical Sciences Unit. I thank CSIR for fellowship.

I sincerely acknowledge JNCASR for providing world-class research facilities. Especially, I thank all the academic, administrative, library, complab, mess, hostel staffs, and Dhanvantari for their support.

I am grateful to Anusooya ma'am and Sohan for all the support, love and affection.

I will take this opportunity to acknowledge all my past and present lab mates, Shubhajit da, Abhiroop da, Neha di, Raju da, Madhulika di, Pallavi di, Supriti, Anita, Mayank, Sayan, Soumya, Pralhad, Sougata, Utkarsh, Navamani anna, Sonu.

I would like to thank my JNC friends, Arpan, Prasenjit, Krishna, Debendra, Sinay, Soumik, Supriti, Debattam, Satyajit, Arindam, Anjana, Bidesh da, Parsanna, Ritam.

Finally, I thank my parents, who have sacrificed so much and always provided the safety-net for me.

Abbreviations

OLED	Organic Light Emitting Diode
IC	Internal Conversion
ISC	Intersystem Crossing
rISC	Reverse Intersystem Crossing
PF	Prompt Fluorescence
RTP	Room Temperature Phosphorescence
TADF	Thermally Activated Delayed Fluorescence
DFT	Density Functional Theory
TDDFT	Time Dependent Density Functional Theory
MCTDH	Multi Configuration Time Dependent Hartree
PS	Photosensitizer
IQE	Internal Quantum Efficiency
EQE	External Quantum Efficiency
SOCME	Spin Orbit Coupling Matrix Element
MCL	Mechanochromic Luminescence
SE	Schrödinger Equation
BO	Born-Oppenheimer
NTO	Natural Transition Orbitals
CT	Charge Transfer
LE	Locally Excited
FMO	Frontier Molecular Orbitals
XC	Exchange Corelation
NAMD	Non-Adiabatic Molecular Dynamics
ML	Machine Learning
DT	Decision Tree
SVM	Support Vector Machine
RF	Random Forest
GB	Gradient Boosting
XGB	Extreme Gradient Boosting
HOMO	Highest Occupied Molecular Orbital
LUMO	Lowest Unoccupied Molecular Orbital



Synopsis

In this thesis, we mainly focused on the triplet harvesting mechanisms that may be used in various applications, such as room temperature phosphorescence (RTP), thermally activated delayed fluorescence (TADF) and sensitization by triplet exciton energy transfer to another molecule. We particularly looked at the excitation properties of pertinent singlet and triplet states involved in inter-system crossing (ISC) or reverse inter-system crossing (rISC) processes as well as direct emissions. Quantum mechanical methods including excited state dynamics, time-dependent density functional theory (TDDFT), and density functional theory (DFT) are used in these computations. We also have investigated data-driven approaches (machine learning techniques) to the complete device efficiency problem in the final work chapter, as straight forward ab-initio solutions are not practical.

The thesis is divided into following seven chapters.

In the **chapter 1**, we have provided a brief overview of the excitation processes involved in triplet harvesting, the importance of harvesting the triplet states, fundamental theoretical perspective on how coherent mixing of states of different spin manifolds give rise to the process like phosphorescence, TADF, ISC, and rISC which are spin-forbidden processes and so cannot occur from the pure states. This chapter also includes computational methodologies used in the investigation. For ground state properties, we have used density functional theory (DFT). Excited-state properties and spin-orbit coupling matrix elements among various excited states were calculated within the time-dependent density functional theory (TDDFT) formalism. To check the effect of nuclear motion on the exciton population in various excited states, we have performed excited-state dynamics. While for data-driven approaches, we have used machine learning (ML) algorithms.

In **chapter 2**, a boron-based donor-spiro-acceptor organic chromophore that exhibits thermally activated delayed fluorescence (TADF) was used to study intersystem crossing and reverse intersystem crossing (rISC) activities. The HOMO and LUMO are spatially separated since the donor and acceptor moieties are in almost perpendicular arrangement, and the compound exhibits charge transfer (CT) transitions. The electron and hole wave functions are localized on the acceptor and

donor units, respectively, in both S_1 and T_1 excited states, which are CT in nature. T_2 , which is more energetic than S_1 and T_1 , is locally excited (i.e., both electron and hole wave functions are localized on an acceptor unit). The spin-orbit coupling matrix element between S_1 and T_1 is extremely small as both are CT states. Our simulation of quantum dynamics and time-dependent density functional theory results demonstrate the existence of a nearby local excited triplet state (T_2), which facilitates the rISC process from the T_1 state to the S_1 state via the T_2 state. The rISC pathway is effectively established when the energy difference between the T_1 and T_2 states is lower.

In the next two chapters (**Chapter 3 & Chapter 4**), we have investigated the dual phosphorescence and TADF in both mechanochromic luminescent material and PmDI derivatives.

Mechanochromic luminescent (MCL) materials, which change their behavior when exposed to external stimuli, have become one of the most promising possibilities for the next generation of effective OLEDs. Recently, a donor-acceptor-donor (D-A-D) triad with two phenothiazine units, separated by a dibenzo[*a,j*]phenazine motif was reported to exhibit mechanochromic luminescence. Based on the conformational flipping of the D units, the triad takes a variety of emissive paths, from phosphorescence to TADF. Using ground and excited states calculations, we examine the conformation-dependent photophysical behavior of this trio in chapter 3. We identify the impact of the conformational changes on their photophysical characteristics by examining the nature of the ground state, excited states, and parameters controlling the reverse ISC crossing rates connected with the relative orientation of the D and A units. The overlap between HOMO and LUMO is enhanced by the axial orientation of both donor groups, according to our findings. This results in a wide singlet-triplet gap, which drives phosphorescence emission. On the other hand, the donor groups' equatorial orientation is minimized to make it easier for rISC to activate the conformers' TADF. It is also emphasized how various geometrical elements affect the conformers' photophysical characteristics. Lastly, we demonstrate how to functionalize the triad in order to maximize TADF efficiency and control the population difference among conformers.

Effective light-emitting diodes benefit greatly from the realization of both thermally activated delayed fluorescence (TADF) and room temperature phosphorescence (RTP) from a single molecule (LEDs). In this research, we examined a derivative of

pyromellitic diimide (CzPhPmDI) that exhibits both RTP and TADF. Aside from CzPhPmDI, we have investigated methyl-substituted spacer and heavy atom substituted (on both donor and acceptor) CzPhPmDI for enhanced RTP and TADF emissions. The phenyl spacer is not entirely perpendicular to the donor and acceptor in the optimum shape of CzPhPmDI, and the dihedral angle is close to 60°. The singlet-triplet (ΔE_{ST}) gap first decreases with a steady increase in dihedral angle (more perpendicular to both Cz and PmDI), but eventually increases the singlet-triplet gap, which has been shown by the dihedral angle-dependent investigations of excited state properties (spacer is nearly perpendicular). The spacer (in CzMe₂PhPmDI) turns perpendicular to both the Cz and PmDI groups, when Me is substituted on it. Due to S₁ and T₁'s differing excitation characteristics, the ΔE_{ST} increases. Additional research reveals that this causes the spacer to become more coplanar with the Cz and PmDI units, resulting in the creation of a twisted intramolecular charge transfer (TICT) state, which finally results in TADF with red-shifted emission. Br substitution on PmDI improves intersystem and reverse intersystem crossing, which is helpful for efficient RTP and TADF, whereas heavy-atom substitution on the donor has little effect on the excited state properties.

In **Chapter 5**, we have probed the triplet sensitizers, which utilize the triplet excitons in photochemical reactions by transferring the energy to a substrate where direct excitation is not possible. For a society with an emphasis on sustainability, photochemical activation by triplet photosensitizers is extremely useful. Using the density functional theory (DFT) and time-dependent density functional theory (TDDFT), we have theoretically examined the excited state features of thioxanthone and its derivatives for the effectiveness of their triplet harvesting properties. The experimental data on this system are in good agreement with the absorption and triplet energies. According to our findings, the S₀ to S₁ transition has a strong oscillator strength since both the S₁ and T₁ states are predicted to be π - π^* in nature. Intersystem crossover (ISC) channel between the S₁ ($^1\pi - \pi^*$) and high energy $^3n - \pi^*$ states result in major triplet exciton conversion. In addition, the radiative and non-radiative channels from S₁ to S₀ compete with the ISC channel and lower the efficiency of triplet harvesting. The ISC channel is not energetically feasible for thioxanthenes with OMe (Me=Methyl) or F substitution at 2 or 2' locations, leading to sluggish intersystem crossing (ISC) quantum yield. The S₁-T₁ gap is small positive for the unsubstituted thioxanthone and for isopropyl substitution at the 2' position, results in a reduced

triplet harvesting efficiency. The $S_1-3n\pi^*$ gap turns negative for systems with buried states and high energy π^* states at the 3 or 3' location of the thioxanthone. This results in a high ISC (>0.9), which is essential for a photocatalyst to work.

Chapter 6 deals with the ML approach for the prediction of efficiency in TADF-based OLEDs. In terms of synthesis and applications in sensing and imaging, the TADF based OLEDs have experienced tremendous progress in recent years. Yet, the unpredictability of external quantum efficiency (EQE) still limits the device-level use. Internal quantum efficiency (IQE) and mechanical pathways for reverse intersystem crossing (rISC) in TADF systems have been the subject of rigorous theoretical research, but EQE has not received as much attention. We used ML models on 30 attributes of 123 samples taken from the literature to predict the EQE_{max} , with data-driven analysis emerging as the fourth paradigm of science (the other three being computational, theoretical, and empirical). On the one hand, the models in use capture device selectivity, but they also tend to be more common in chromophores that are more emissive. We have demonstrated that the ensemble learning model, Gradient Boosting (GB), with a r^2 score of $0.71\pm 0.04/0.84$ and a low RMSE of $4.22\pm 0.55/2.53$ for the train/test set, has been able to predict EQE_{max} . The best model that can predict TADF chromophores of any emissive range and outline the impact of device architecture, according to the state-of-the-art (SOTA), is the GB model. To make this so-called "black-box" model understandable, we also performed feature importance score analysis. This investigation has assisted in identifying key factors that contribute to increased EQE effectiveness.

The thesis ends with the summary (**Chapter 7**) and results obtained in chapters 2-6 along with an outlook towards possible future research ideas and developments in triplet exciton harvesting and its applications in optoelectronics and photocatalysis.

List of Publications

Publications related to the thesis work

1. *“Intersystem Crossing in Boron-Based Donor–Spiro–Acceptor Organic Chromophore: A Detailed Theoretical Study”*
Bidhan Chandra Garain, Pralok K Samanta, Swapan K Pati
The Journal of Physical Chemistry A, 2021, 125, 6674-6680.
2. *“Delineating Conformation Control in the Photophysical Behaviour of a Molecular Donor-Acceptor-Donor Triad”*
Bidhan Chandra Garain, Shubhajit Das, Swapan K Pati
ChemPhysChem, 2021, 22, 2297-2304.
3. *“Unraveling the Efficiency of Thioxanthone Based Triplet Sensitizers: A Detailed Theoretical Study”*
Bidhan Chandra Garain, Swapan K Pati
ChemPhysChem, 2022, e202200753.
4. *“Tailoring Dual Emissions from Pyromellitic Diimide Derivatives through Substitution: A Theoretical Perspective”*
Bidhan Chandra Garain, Swapan K Pati
(Submitted 2023).
5. *“Improved Prediction of Maximum EQE in TADF-based OLEDs Through Ensemble Learning”*
Bidhan Chandra Garain, Swapan K Pati
(Manuscript under preparation).

Other publications by the author

6. *“Nitric oxide sensing through 1, 2, 3, 4-oxatriazole formation from acylhydrazide: a kinetic study”*
Abu Saleh Musha Islam, Rahul Bhowmick, **Bidhan Chandra Garain**, Atul Katarkar, Muhammad Ali
The Journal of Organic Chemistry, 2018, 83, 13287-13295.

7. *“Ambient Room Temperature Phosphorescence and Thermally Activated Delayed Fluorescence from a Core-Substituted Pyromellitic Diimide Derivative”*
Suman Kuila, Swadhin Garain, Gangadhar Banappanavar, **Bidhan Chandra Garain**, Dinesh Kabra, Swapan K Pati, Subi J George
The Journal of Physical Chemistry B, 2021, 125, 4520-4526.

8. *“Arylene diimide phosphors: aggregation modulated twin room temperature phosphorescence from pyromellitic diimides”*
Swadhin Garain, Suman Kuila, **Bidhan Chandra Garain**, Meenal Kataria, Aditya Borah, Swapan K Pati, Subi J George
Angewandte Chemie International Edition, 2021, 60, 12323-12327.

9. *“Light-Harvesting Supramolecular Phosphors: Highly Efficient Room Temperature Phosphorescence in Solution and Hydrogels”*
Swadhin Garain, **Bidhan Chandra Garain**, Muthusamy Eswaramoorthy, Swapan K Pati, Subi J George
Angewandte Chemie International Edition, 2021, 60, 19720-19724.

10. *“Chiral arylene diimide phosphors: circularly polarized ambient phosphorescence from bischromophoric pyromellitic diimides”*
Swadhin Garain, Souvik Sarkar, **Bidhan Chandra Garain**, Swapan K Pati, Subi J George

11. *“Anion– π -induced room temperature phosphorescence from emissive charge-transfer states”*

Swadhin Garain, Sopan M Wagalgave, Anju Ajayan Kongasseri, **Bidhan Chandra Garain**, Shagufi Naz Ansari, Gopa Sardar, Dinesh Kabra, Swapan K Pati, Subi J George

Journal of the American Chemical Society, 2022, 144, 10854-10861.

12. *“Room temperature charge-transfer phosphorescence from organic donor–acceptor Co-crystals”*

Swadhin Garain, Shagufi Naz Ansari, Anju Ajayan Kongasseri, **Bidhan Chandra Garain**, Swapan K Pati, Subi J George

Chemical Science, 2022, 13, 10011-10019.

Contents

Acknowledgments.....	ix
Abbreviations.....	x
Synopsis	xii
List of Publications.....	xvi
Publications related to the thesis work	xvi
Other publications by the author	xvii
List of Figures	23
List of Tables	28
1 Introduction	1
1.1 Excitation processes	2
1.2 Importance of triplet harvesting	4
1.3 Theoretical perspectives on triplet exciton harvesting	5
1.3.1 Spin-Orbit Coupling	5
1.3.2 Perturbation theory in the context of singlet-triplet transition	7
1.4 Systems studied on the aspect of triplet harvesting	8
1.4.1 Mechanochromic luminescent (MCL) molecules	9
1.4.2 Spiro complex for TADF	10
1.4.3 Core-substituted Pyromellitic diimide derivative for dual emission (Phosphorescence and TADF)	11
1.4.4 Thioxanthone-based triplet sensitizers as efficient photocatalysts .	13
1.4.5 TADF-based OLED devices	14
1.5 Computational Methodology	15
1.5.1 Schrödinger equation for the solution of electronic structure	15
1.5.2 Born-Oppenheimer Approximation	16
1.5.3 Density Functional Theory	17
1.5.4 Time-Dependent Density Functional Theory	21
1.5.5 Exchange-Correlation Functionals	23
1.5.6 Non-adiabatic Dynamics	25
1.5.7 Machine Learning	27
1.6 Softwares Used	30
1.7 Scope of the thesis	31
Bibliography	33
2 Intersystem Crossing in Boron-Based Donor-Spiro-Acceptor Organic Chromophore: A Detailed Theoretical Study*	39

2.1	Introduction	40
2.2	Computational details	42
2.2.1	Spin-Vibronic Coupling Hamiltonian	43
2.2.2	Wavefunction Propagation	45
2.2.3	Intersystem Crossing rate	45
2.3	Results and Discussions	46
2.3.1	Geometry and Optical properties	46
2.3.2	Characteristics of Low Energy Excited States and Spin-orbit Coupling Interaction	48
2.3.3	Intersystem Crossing (ISC) and Reverse Intersystem Crossing (rISC) 50	
2.3.4	Quantum Dynamics of The Low Energy Excited States	51
2.4	Conclusions	54
	Bibliography	55
3	Delineating Conformation Control in the Photophysical Behaviour of a Molecular Donor-Acceptor-Donor Triad*	59
3.1	Introduction	60
3.2	Computational details	62
3.3	Results and Discussions	64
3.3.1	Ground state geometry and frontier molecular orbital analysis	64
3.3.2	Excitation energies and Natural Transition Orbitals (NTO)	66
3.3.3	Spin-Orbit Coupling and Reorganization energy	70
3.3.4	Creating population difference by functionalization	76
3.4	Conclusions	77
	Bibliography	78
4	Tailoring Dual Emissions from Pyromellitic Diimide Derivatives through Substitution: A Theoretical Perspective*	82
4.1	Introduction	83
4.2	Computational Methodology	85
4.2.1	Spin Orbit Coupling (SOC) Matrix Elements	86
4.2.2	Intersystem Crossing (ISC) rate	86
4.3	Results and Discussions	87
4.3.1	Dihedral angle dependent studies of CzPhPmDI and Geometrical aspects 87	
4.3.2	Absorption energies and Jablonski diagram	90
4.3.3	ISC vs rISC and comparison of excited state geometries	92
4.4	Conclusions	94

Bibliography	96
5 Unraveling the Efficiency of Thioxanthone Based Triplet Sensitizers: A Detailed Theoretical Study*	100
5.1 Introduction	101
5.2 Computational Methodology	103
5.2.1 Geometry Optimization and Optical Absorption	103
5.2.2 Spin-Orbit Coupling	104
5.2.3 Intersystem Crossing rate	104
5.2.4 Fluorescence decay rate	105
5.3 Results and Discussions	105
5.3.1 Ground state and Frontier Molecular Orbitals	105
5.3.2 Absorption Energy and Jablonski Profile	107
5.3.3 Excited state geometry comparison	111
5.3.4 Intersystem crossing rate constants and its comparison with fluorescence rates	113
5.4 Conclusions	116
Bibliography	117
6 Improved Prediction of Maximum EQE in TADF-based OLEDs Through Ensemble Learning*	122
6.1 Introduction	123
6.2 Computational Methodology	125
6.2.1 Cross Validation	126
6.2.2 Metrics	127
6.2.3 Hyperparameter Tuning	128
6.3 Results and Discussions	128
6.3.1 Exploratory Data Analysis	128
6.3.2 Machine Learning	130
6.4 Conclusions	137
Bibliography	139
7 Summary and Future Outlook	145
7.1 Retrospect	145
7.2 Prospects	148

List of Figures

Figure 1.1: Applications of Light-matter interaction	1
Figure 1.2: The Perrin-Jablonski diagram demonstrating most important transitions including S_1 , T_1 , S_n states along with their spin orientations.....	2
Figure 1.3: Different applications of triplet excitons.	5
Figure 1.4: Schematic representation of a specific case of mechanochromic luminescence	9
Figure 1.5: Investigated molecule PTZ-DBPHZ (1) and the relationship between MCL properties and conformers. Reprinted with permission from ref 25. Copyright 2014 Royal Society of Chemistry.	10
Figure 1.6: Design strategy for D–spiro–A structure and representative materials. Reprinted with permission from ref 29. Copyright 2021 American Chemical Society.	11
Figure 1.7: CzPhPmDI and its emission characteristics. Reprinted with permission from ref 37. Copyright 2021 American Chemical Society.....	12
Figure 1.8: (A) Simplified Jablonski diagram of a triplet mediated photochemical reaction: (1) Direct excitation of substrate to S_1 ; (2) Singlet decay by radiative and nonradiative processes; (3) ISC to reactive T_1 ; (4) Photoexcitation of sensitizer; (5) Rapid ISC to T_1 ; (6) Triplet energy transfer to substrate; and (7) Chemical reaction and relaxation to ground state. (B) UV absorption of BP and ITX at 1×10^{-4} M, overlaid with UVA emission from medium pressure Hg lamp and Isolated yields of [2 + 2]/retro-Mannich product 10 . Reprinted with permission from ref 53 Copyright 2021 American Chemical Society.	13
Figure 1.9: (a) Energy level diagrams, (b) OLED device structure and (c) the chemical structure of the materials used in the TADF devices. Ref 60	14
Figure 1.10: Types of machine learning and application of supervised learning	28
Figure 2.1: Schematic two-dimensional and ground state optimized (3D) structure of the boron-based donor-spiro-acceptor molecule.	41
Figure 2.2: Frontier Molecular Orbitals of the boron-based donor-spiro-acceptor molecule. Energy value of each molecular orbital is given in eV.	47
Figure 2.3: Natural transition orbitals and their symmetry calculated using TDA-DFT method.....	48

Figure 2.4: Potential energy fitting to the vibronic coupling Hamiltonian for S_1 (red), T_1 (blue) and T_2 (green) with four different low energy vibrational modes (a) ν_5 , (b) ν_6 , (c) ν_{17} and (d) ν_{24} which have coupling strength of $> 50 \text{ cm}^{-1}$	52
Figure 2.5: (a) Relative population of 1CT state with varying energy level of 3LE .; (b) Relative population of 1CT without the effect of SOC and without vibronic coupling (interstate coupling value is zero) at $E_{T_2} = 2.81 \text{ eV}$. All the cases 3CT (i.e., T_1) state	53
Figure 2.6: (a) Relative population of 3CT and 3LE at 3LE energy level at 3.17 eV (i.e., when the 3LE and 3CT gap is higher $\sim 0.36 \text{ eV}$); (b) Relative population of 3CT and 3LE at 3LE energy level at 2.81 eV (i.e., when the 3LE and 3CT gap is $\sim 0 \text{ eV}$).....	53
Figure 3.1: Molecular structure of the PTZ-DBPHZ D-A-D triad along with the 3D representation of three conformers.	60
Figure 3.2: Plot of J^2 vs ω for all three conformers using LC- ω *PBE functional in conjunction with 6-31+g(d,p) basis set.	63
Figure 3.3: Free energy profile for the interconversion between conformers of PTZ-DBPHZ D-A-D triad. All energy values are in kcal/mol.....	65
Figure 3.4: HOMO-LUMO of three conformers, PTZ, DBPHZ and their relative energy.....	66
Figure 3.5: Vertical excitation energies for the three conformers calculated at LC- ω *PBE/6-31+g(d,p) level of theory	67
Figure 3.6: Natural Transition Orbitals of the three conformers for low lying triplet and singlet excited states, λ is the highest coefficient of SVD.....	69
Figure 3.7: Relative RMSD of the structures with respect to their respective ground state structures	71
Figure 3.8: Mode-wise reorganization energy for the T_1 state for all three conformers	72
Figure 3.9: Hole and electron picture for the transition from S_1 to S_0 at S_1 optimized geometry.	73
Figure 3.10: Relative energies (eV) of both substituted and unsubstituted conformers	75
Figure 3.11: Optimized structures of the Me substituted conformers.....	76
Figure 4.1: CzPhPmDI and its derivatives studied in this work.....	85
Figure 4.2: Dihedral angle dependence of ΔE_{ST} , oscillator strength for S_0 to S_1 transition and spin-orbit coupling between the T_1 and $S_{1/0}$ in CzPhPmDI.....	88
Figure 4.3: Structures for angle-dependent studies	90

Figure 4.4: Jablonski diagram for CzPhPmDI and its derivatives. Blue lines indicate the singlet state while red lines indicate the triplet states	91
Figure 4.5: NTO diagram for low lying excited state of CzPhPmDI and its derivatives. λ denotes the highest value of singular value decomposition (SVD).	92
Figure 4.6: RMSD values of S_1 and T_1 states. These values are calculated with respect to S_0 geometries.	93
Figure 5.1: Systems studied in this work along with their ISC quantum yields (Φ_{ISC}). Φ_{ISC} were experimentally calculated from bleach recovery studies	103
Figure 5.2: +M effect of the Y or Y' substitution. Black and red lines indicate the presence of a node at π , π^* level respectively	106
Figure 5.3: FMO energies of the thioxanthone and its derivatives. Orange lines denote the n orbital energies, sky-blue lines denote the π energies and blue lines denote the π^* energies.	107
Figure 5.4: Relevant NTOs of the thioxanthone derivatives. Λ denotes the coefficient for the transition from HONTO to LUNTO after singular value decomposition (SVD)	109
Figure 5.5: Jablonski diagram of 1, 5 and 8.	111
Figure 5.6: S_0 , T_1 , S_1 state geometry and Root Mean Square Deviation (RMSD) values of T_1 and S_1 geometries with respect to its ground state S_0 geometry.....	112
Figure 6.1: (a) Pearson correlation heatmap in between variables and with the EQE_{max} (index 31), only those variables are shown which have $ r > 0.20$. (b) contour heatmap of PLQY and EQE_{max} with HOMO and LUMO offset.	129
Figure 6.2: Regression plot of EQE_{max} vs (a) PLQY (b) ΔEST (c) -LUMO energy of HTL1 (d) -HOMO energy of ETL2.....	130
Figure 6.3: (a) r_2 score plot for SVR model (b) Learning curve for SVR model	131
Figure 6.4: (a) r_2 score plot for DT regression model (b) Feature importance plot for the model	132
Figure 6.5: (a) r_2 score plot for K-NN regression model (b) Plot of hyperparameter tuning with $n_neighbour$ variation.....	132
Figure 6.6: Schematic Representations of the variations of ensemble-based learning, their nature and used model under each class in this work	133
Figure 6.7: (a) r_2 score plot for Random Forest regression model (b) Feature importance plot for RF model (c) Learning Curve for RF model.....	134

<i>Figure 6.8: (a) r2 score plot for AdaBoost regression model (b) Feature importance plot for AdaBoost model (c) Learning Curve for AdaBoost model.....</i>	<i>134</i>
<i>Figure 6.9: (a) r2 score plot for LightGBM regression model (b) Feature importance plot for LighGBM model (c) Learning Curve for LighGBM model.....</i>	<i>135</i>
<i>Figure 6.10: (a) r2 score plot for XGB regression model (b) Feature importance plot for XGB model (c) Learning Curve for XGB model.....</i>	<i>135</i>
<i>Figure 6.11: Comparison of GB, XGB, AdaBoost, LightGBM and RF with (a) r2 score (b) RMSE. Blue bar indicates train set result (cross-validated); orange bar indicates test set result. Black line indicates the variance.</i>	<i>136</i>
<i>Figure 6.12: Train/ test metrics (r2 score and RMSE) of GB Model. For train set, the evaluated metrics is the mean of cross-validation.....</i>	<i>136</i>
<i>Figure 6.13: a) Feature importance plot (b) Learning curve for GB.</i>	<i>137</i>

List of Tables

Table 2.1: Low absorption energies (nm) along with oscillator strength (f) using Gaussian 16.	42
Table 2.2: MCTDH details of normal mode, primitive basis and single-particle basis used in the dynamics.	45
Table 2.3: Ground State Optimized Geometry Parameters.....	46
Table 2.4: Optical Absorption Properties the Boron-Based Donor-Spiro-Acceptor Molecule	47
Table 2.5: Excitation Energies and Spin-orbit Coupling Matrix Elements (SOCME) of Low Energy Excited States.....	49
Table 2.6: Intersystem Crossing (ISC) and Reverse Intersystem Crossing (rISC) Rate Constants.....	50
Table 2.7: Fitting Parameters for All Four Modes in eV.....	51
Table 3.1: Selected bond lengths (\AA) and dihedral angles ($^\circ$) at the ground state optimized geometry (S_0) of the conformers of the PTZ-DBPHZ D-A-D triad computed at the B3LYP/6-31+g(d,p) level.....	65
Table 3.2: Vertical excitation energies and oscillator strengths (osc. str.) for the three conformers calculated at LC- ω *PBE/6-31+g(d,p) level of theory	66
Table 3.3: CT and LE percentage for the low-lying excited states for all three conformers	68
Table 3.4: Spin-Orbit Coupling Elements (cm^{-1}) $S_1HT_nS_2HT_n$ calculated using LCY- ω *PBE functional with TZP basis set at the T_1 and S_1 optimized structure	71
Table 3.5: Scheme for the characterization of photophysical behavior of each conformers	74
Table 3.6: qualitative comparison of rISC rates	75
Table 4.1: Dihedral angles between spacer and donor, acceptor (φ , ψ) and bond lengths (r_1 , r_2).....	87
Table 4.2: Vertical excitation energies (Singlet) in eV and corresponding oscillator strength in in parenthesis.....	89
Table 4.3: Excitation energies calculated using the B3LYP, CAM-B3LYP, Mo6, Mo62X, wb97xd and experimental absorption energies in toluene.....	90
Table 4.4: intersystem and reverse intersystem crossing rates between S_1 and T_1 states, where the adiabatic energy gap calculated using Mo62x functional.....	93

<i>Table 4.5: intersystem and reverse intersystem crossing rates between S_1 and T_1 states, where the adiabatic energy gap calculated using CAM-B3LYP functional...</i>	<i>94</i>
<i>Table 5.1: C=O, C-OMe and C-F bond length at the S_0 state</i>	<i>106</i>
<i>Table 5.2: theoretical and experimental absorption (in acetonitrile) and triplet energies calculated using MO6 functional in conjunction with 6-31+g(d) basis set calculated in acetonitrile.</i>	<i>108</i>
<i>Table 5.3: Theoretical absorption and triplet energies calculated using B3LYP functional in conjunction with 6-31+g(d) basis set.</i>	<i>110</i>
<i>Table 5.4: C=O, C-OMe and C-F bond length at the S_1 and T_1 state</i>	<i>112</i>
<i>Table 5.5: Dominating intersystem crossing rate constants and radiative decay rate constants</i>	<i>114</i>
<i>Table 5.6: Calculated singlet state lifetime for systems 1-5 where ISC rate is much higher than radiative and non-radiative decay rate ($k_{ISC} \gg k_{rad} + k_{nr}$).....</i>	<i>115</i>
<i>Table 6.1: Performance metrics of SVR, DT and K-NN</i>	<i>131</i>
<i>Table 6.2: Hyperparameters for the employed models</i>	<i>138</i>

Chapter 1

1 Introduction

Light-matter interaction refers to the ways in which light and matter interact with each other. This can include absorption, reflection, refraction, and scattering of light by matter. These interactions are important in many fields, including optics, photonics, and materials science. Applications of light-matter interaction include telecommunications, display technology, imaging, solar energy, and medicine (Figure 1.1). In medicine, for example, lasers are used for a wide range of applications such as surgery, cancer treatment, and diagnosis. In materials science, light is used to study the properties of materials, and in telecommunications, light is used to

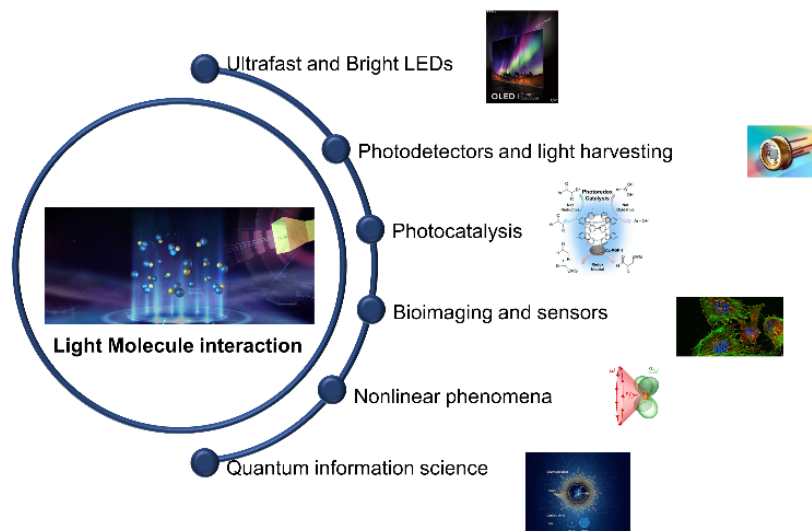


Figure 1.1: Applications of Light-matter interaction

transmit information over long distances. In this thesis, we will focus on triplet exciton harvesting. Triplet exciton harvesting refers to the process of capturing and utilizing triplet excitons, which are a type of exciton (a bound state of an electron and a hole in a semiconductor or a molecule) that have a longer lifetime than singlet excitons. This is done in order to improve the efficiency of organic photovoltaic cells, OLEDs, and other optoelectronic devices. The key to achieving this is to use materials that can efficiently convert triplet excitons into singlet excitons, which can then be harvested as electrical energy. This process is known as triplet-singlet harvesting, and it is an

active area of research in the field of photovoltaics and optoelectronics. In the next section, we will discuss the excitation processes which lead to the generation of triplet excitons.

1.1 Excitation processes

Due to their long lifespan and spin multiplicity, triplet excitons highlight a number of processes and technologies in organic molecules. Efficient triplet exciton harvesting has always been a major focus for scientists for better optoelectronic and photocatalytic applications.¹⁻¹² This section describes in great detail the various excitation processes which lead to the generation of triplet excitons in organic chromophores. Pauli exclusion principle in 1925 established electronic spin as fundamental property in quantum mechanics like mass and charge of electrons.¹³ The angular momentum of an electron is described by its spin state. For a two-electron system, there are four allowed spin orientations, which leads to two different quantum total spin states: (1) singlet (nondegenerate); (2) triplet (3-fold degenerate). If the spin orientation of both the electrons leads to total spin quantum number $S=0$, it is called singlet. While orientations leading to $S=1$, is called triplet state.

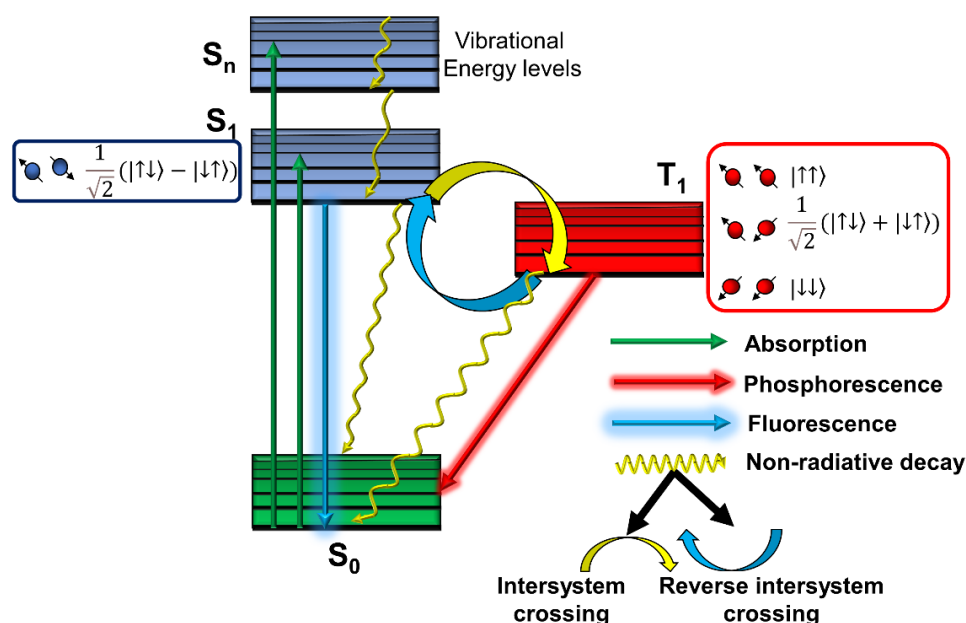


Figure 1.2: The Perrin-Jablonski diagram demonstrating most important transitions including S_1 , T_1 , S_n states along with their spin orientations.

Organic closed-shell molecules have a spin-paired singlet configuration in their ground state (S_0). Spin-allowed transitions to the singlet excited states (S_n) take place when light interacts with the ground state wavefunction. This process is very fast and occurs in the femtosecond range ($t \sim 10^{-15}$ s). This process takes place from the lowest vibrational energy level of ground state to some higher vibrational level of singlet excited electronic state. The system starts squandering the energy received through light absorption in an effort to return to equilibrium from the non-equilibrium high energy singlet state (Figure 1.2). First, it relaxes to the lowest vibrational state of the excited electronic state, which is done by releasing the thermal energy or transferring the energy to a neighbouring molecule within a timescale of 10^{-13} to 10^{-11} s. Further, the exciton relaxes back to the lowest excited singlet state (S_1) following Kasha's rule via internal conversion (IC) method.¹⁴ This non-radiative phenomenon occurs within a timescale of $\sim 10^{-12}$ s. At the S_1 state the fate of the excitons is three-fold: (1) radiative transition from S_1 to S_0 (fluorescence) (2) non-radiative decay from S_1 to S_0 (3) intersystem crossing (ISC) to neighbouring triplet excited state.¹⁵ ISC is a spin-forbidden process and as a result to conserve the total angular momentum, while the spin-angular momentum is changing a change in orbital angular momentum is also important (El-Sayed rule: which states that ISC between π - π^* to n - π^* is fast).^{16, 17} Such change in orbital type ensures that the spin-orbit coupling strength between two electronic states of different spin-manifolds is high. Another way to increase the spin-orbit coupling is to incorporate heavy atoms within the chromophore.

If radiative transition happens from T_1 state to S_0 state, it is called phosphorescence. Both radiative processes occur from the lowest vibrational level of S_1/T_1 . Although phosphorescence ($\sim 10^{-6}$ s to 10^{-3} s) occurs in a much slower time scale than prompt fluorescence. Nevertheless, triplet excitons are not stable enough. Quenching from molecular triplet oxygen and bimolecular collisions apart from non-radiative decay make phosphorescence quantum efficiency very low.

Even, the excitons from the triplet states can further go back to the singlet state via the help of thermal energy through a non-radiative process. This is termed reverse intersystem crossing (rISC) or up-conversion intersystem crossing since the T_1 state is lower in energy than the S_1 state (Hund's multiplicity rule), which is very important for thermally activated delayed fluorescence (TADF). Although, Domcke *et al.* have also reported exceptional adiabatic inverted singlet-triplet gap in closed-shell organic

molecules.¹⁸ The main focus of the thesis is to understand the underlying mechanism of triplet exciton harvesting in ambient conditions and improve that procedure.

1.2 Importance of triplet harvesting

According to the Fermi-Dirac spin statistics, 25% of the total excitons are singlet, and the rest of the 75% are triplet in nature. The conventional fluorescence OLEDs, which is based on prompt fluorescence (PF) molecules have a maximum internal quantum efficiency (IQE) of 25%. Other 75% of the generated excitons are dissipated through several processes, which limits the application of conventional fluorophores. On the contrary, if the other 75% of the excitons can be utilized apart from the 25% of the singlet excitons, the total IQE becomes 100, which significantly boosts the efficiency of triplet exciton-based fluorophores. Phosphorescent OLEDs can harness both 25 and 75 percent of the generated excitons, leading to its IQE \sim 100. These materials are called second-generation light emitters. But they use rare elements like Ir and Pt which leads to high device fabrication costs. Furthermore, there is still a need for the development of deep-blue phosphors that possess extended durations of luminescence. So, further development in this field has led to the generation of third-generation emitters, which are thermally activated delayed fluorescence (TADF). They convert the triplet excitons into singlet excitons via the help of thermal energy and thus have an IQE \sim 100. They are better prospects for OLEDs because of their effective use of triplet exciton, efficient quantum yield, simplicity in manufacturing, heavy atom free molecular design, and most crucially, low efficiency roll-off. However, organic fluorophores are not stable enough to be of practical use as TADF-OLED and so has not been able to come out for practical use yet. Even bimolecular triplet collision (triplet-triplet annihilation) also leads to the generation of delayed fluorescence but limits its IQE only to 62.5 %. The research into chromophores connected to the triplet excited state or the photophysical processes is less developed than that of fluorophores. Apart from luminescence, the triplet excitons can also be utilized for molecular sensing, photodynamic therapy, photoinduced polymerization, and photocatalytic reactions via the help of triplet photosensitizers (PSs) (Figure 1.3).

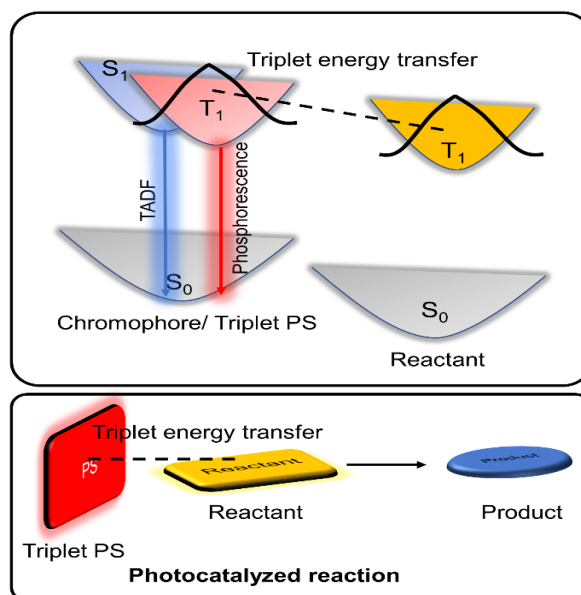


Figure 1.3: Different applications of triplet excitons.

1.3 Theoretical perspectives on triplet exciton harvesting

Under electric-dipole approximations, absorption happens between ground state and excited singlet state (S_n ; $n \geq 1$). These transitions are spin-allowed and follow the orbital symmetry selection rule. While triplet harvesting processes like phosphorescence (radiative transition from T_1 to S_0), ISC (non-radiative transition from singlet manifold to triplet manifold), rISC (non-radiative transition from T_1 state to higher energy S_1) are all spin-forbidden in nature and become possible via the help of singlet-triplet mixing. In the next section, we will discuss spin-orbit coupling, and perturbation theory for singlet-triplet transitions.

1.3.1 Spin-Orbit Coupling

Without spin-orbit coupling or any other relativistic effects the wave-function of a singlet state can be represented as, a product of symmetrical spatial wave-function (Φ_+) and antisymmetric spin wave-function (Ω_-),

$${}^1\Psi = \Phi_+ \Omega_- \quad (1.1)$$

A singlet state for a two-electron system (simple representation; molecules contain more than two electrons), the spatial and spin wave function can be written as,

$$\Phi_+ = \frac{1}{\sqrt{2}} [\varphi_a(1)\varphi_b(2) + \varphi_a(2)\varphi_b(1)] \quad (1.2)$$

$$\Omega_- = \frac{1}{\sqrt{2}} [\alpha\beta - \beta\alpha] \quad (1.3)$$

Where $\varphi_a(1), \varphi_b(2)$ are spatial orbitals for electron 1 and 2 respectively and depends on spatial coordinates x, y, z . α and β are one-electron eigenfunction of S_z operator with quantum numbers $\pm\frac{1}{2}$.

The triplet state can similarly be represented as the product of antisymmetric spatial wave-function and symmetrical spin wave-function,

$${}^3\Psi = \Phi_- \Omega_+ \quad (1.4)$$

In case of triplet state, there are total 3 symmetric spin wave-function,

$$\Phi_- = \frac{1}{\sqrt{2}} [\varphi_a(1)\varphi_b(2) - \varphi_a(2)\varphi_b(1)] \quad (1.5)$$

$$\Omega_-^0 = \frac{1}{\sqrt{2}} [\alpha\beta - \beta\alpha] \quad (1.6)$$

$$\Omega_-^{+1} = \alpha\alpha \quad (1.7)$$

$$\Omega_-^{-1} = \beta\beta \quad (1.8)$$

In this example, singlet and triplet state correspond to the same electronic configuration (same spatial orbitals). And ‘-’ in the triplet state spatial wave function ensures that the triplet state energy will always be lower than singlet state energy.

Neither ${}^1\Psi$ nor ${}^3\Psi$ are “pure” singlet or triplet states for real systems (even for helium and noble gases).^{16, 19-22} Spin-orbit coupling ensures mixing between these ${}^1\Psi$ and ${}^3\Psi$ states and helps in spin-flip transitions; these are called mixed or coherent states (e.g., phosphorescence, ISC and rISC). The relationship between spin-angular momentum (S) and spin-magnetic momentum is (μ),

$$\mu = -\frac{|e|\hbar}{mc} S \quad (1.9)$$

Where, e , m , and c are universal constants.

Under relativistic approximation and considering equation 1.9, the spin-orbit coupling operator can be written as,²³

$$\hat{H}_{SO} = \frac{Ze^2}{2m^2c^2r^3}LS \quad (1.10)$$

L is the orbital angular momentum and r denotes the distance between electron and nucleus. For a molecular system containing many electrons and accounting for the summation of i electrons and A nuclei the operator can be expressed as,²⁴

$$\hat{H}_{SO} = a^2 \sum_A \sum_i \frac{Z_A}{r_{Ai}^3} \vec{l}_{Ai} \vec{s}_i \quad (1.11)$$

a is the the fine structure constant ($a \approx 1/137$ if l , s and r are in atomic units). Z_A is effective nuclear charge for each atom. The expectation value of $\frac{1}{r^3}$ with Slater type orbitals comes out to be Z^3 and SOC dependence becomes Z^4 . This explains why inclusion of heavy atom increases the spin-orbit coupling between singlet and triplet states.

1.3.2 Perturbation theory in the context of singlet-triplet transition

1.3.2.1 Phosphorescence

Due to spin-orbit coupling, both singlet and triplet states get contaminated by triplet and singlet states respectively. Under first-order perturbation theory, any perturbed state can be represented as, the sum of the unperturbed state (pure) state and admixture of wavefunction from the other states (n th singlet-state wave functions S_n). A simple example of T_1 perturbed states is given below,

$$\tilde{T}_1 = T_1 + \sum_n \delta_n S_n \quad (1.12)$$

Where the admixture coefficient can be expressed as,

$$\delta_n = \frac{\langle S_n | H_{SO} | T_1 \rangle}{E(S_n) - E(T_1)} \quad (1.13)$$

A similar kind of mixing is also possible for ground state (S_0) by T_m states and phosphorescence is proportional to the square of $\langle \tilde{S}_0 | M | \tilde{T}_1 \rangle$. M is the electric dipole moment operator.

1.3.2.2 Non-radiative transitions (ISC and rISC)

Intersystem and reverse intersystem crossing rates were calculated using the Fermi-Golden rule:^{25, 26}

$$k_{ISC/rISC}^{nm} = 2\pi/\hbar \rho_{FC} |\langle n | \hat{H}_{SOC} | m \rangle|^2 \quad (1.14)$$

where, $\langle n | \hat{H}_{SOC} | m \rangle$ is the SOC matrix element between two electronic states n and m of different spin-manifolds. ρ_{FC} is Frank-Condon weighted density of states. ρ_{FC} is approximated using semiclassical Marcus theory,²⁷

$$\rho_{FC} = \frac{1}{\sqrt{4\pi\lambda_M k_B T}} \exp \left[-\frac{(\Delta E_{nm} + \lambda_M)^2}{4\lambda_M k_B T} \right] \quad (1.15)$$

where λ_M , k_B , T and ΔE_{nm} are the Marcus reorganization energy, Boltzmann constant, temperature and adiabatic energy gap between n and m state, respectively.

1.4 Systems studied on the aspect of triplet harvesting

We have studied a series of systems ranging from luminescent molecules (consisting of TADF, dual phosphorescence-TADF, and mechanochromic luminescent molecules) and devices to triplet sensitizers-based photocatalysts. In this section, we will give a brief overview of the studied systems.

1.4.1 Mechanochromic luminescent (MCL) molecules

Mechanochromic luminescent materials are kind of materials that change their emission spectra (colour) upon the application of mechanical force (grinding, crushing, rubbing,

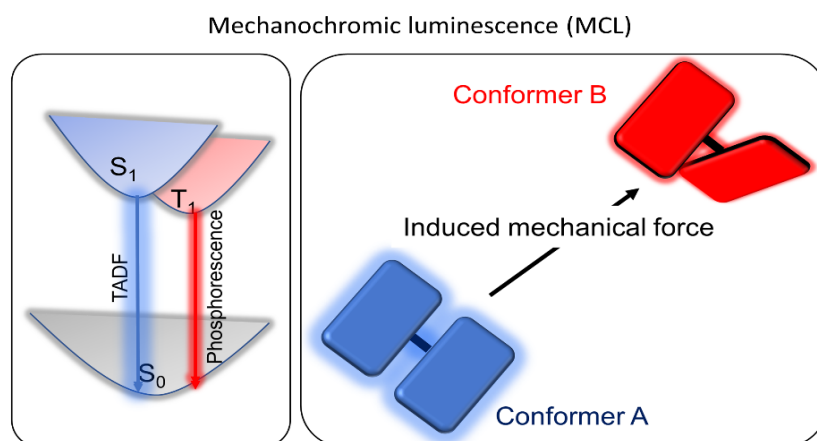


Figure 1.4: Schematic representation of a specific case of mechanochromic luminescence

extrusion).²⁸⁻³² These materials revert back to their original state upon another application of external stimuli (Figure 1.4). As a result, they are considered smart materials and are prospects for luminescence switches, mechanosensors, security papers, data storage and in various optoelectronic devices.³³ As we previously mentioned phosphorescence and TADF are completely opposite and competing processes. But recent literature shows that dual phosphorescence and TADF are possible from some chromophore. Recently, Data, Tadeka *et al.* reported mechanochromic luminescence from a U-shaped donor-acceptor-donor (D-A-D molecular triad), where one type of conformer is correlated with one type of luminescence characteristics (Figure 1.5).³⁴⁻³⁷ The axial arrangement between donor and acceptor makes room temperature phosphorescence more dominant. While the equatorial arrangement enhances TADF. Therefore, it is essential to theoretically investigate the mechanistic pathways for photophysical characteristics of organic emitters in order to identify their distinct luminescent functionalities and subsequently give a proposal for better MCL materials.

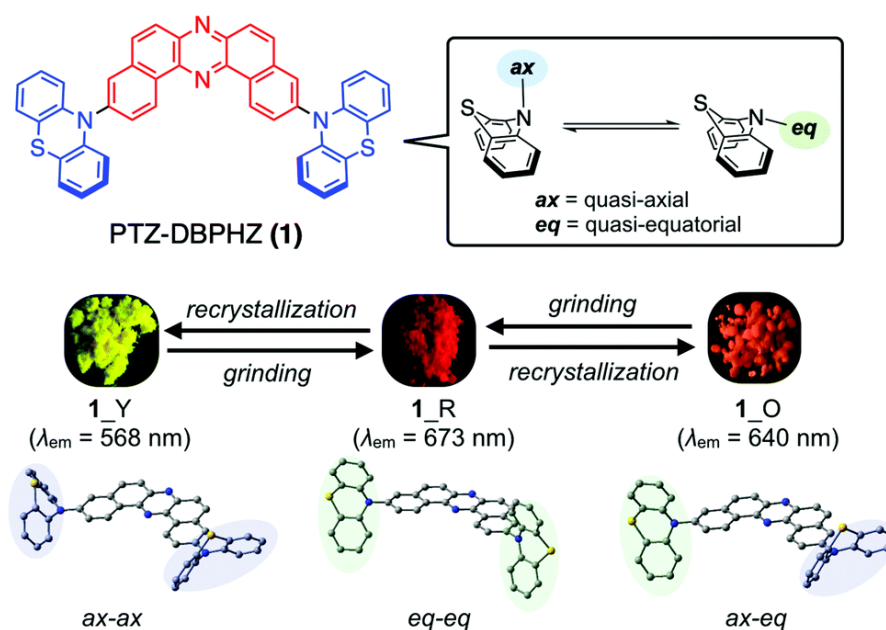


Figure 1.5: Investigated molecule PTZ-DBPHZ (**1**) and the relationship between MCL properties and conformers. Reprinted with permission from ref 25. Copyright 2014 Royal Society of Chemistry.

1.4.2 Spiro complex for TADF

As we already mentioned in the earlier sections third-generation light emitters (TADF) are the best candidates for organic light emitting-diodes which is vital for next-generation display and lighting technologies. In this regard, three types of organic structures are the most important: (1) perpendicular donor-acceptor system connected via a bond (2) spiro complex, and (3) multiresonant CT systems. The three-dimensional (3D) architectures of spiro-type units, which create perpendicular arrangements of the two molecular halves, set them apart from other organic units. Significantly, the introduction of a spiro junction in the orthogonal and rigid molecular structure, resulting in a doubling of the molecular weight, leads to entanglement in the amorphous state and creates obstacles for recrystallization which is useful for OLEDs.³⁸ The 9,9'-spiro-bifluorene (SBF) fragment, which was initially created by Clarkson and Gomberg in 1930, should serve as the starting point for the success story of the spiro-type optoelectronic materials.^{39, 40} Apart from that such arrangement caused by the orthogonal spiro-type structure, which aids in achieving high out-coupling efficiency, they discovered that the horizontal dipole ratio (θ_{\parallel}) of the spiro-

type emitters is rather high. Generally, spiro complexes have low ΔE_{ST} . But this lowered singlet-triplet gap (Figure 1.6) comes with a curse low spin-orbit coupling between the S_1 and the T_1 state due to the charge-transfer (CT) nature in both of their excitations. So, we have studied a boron-based donor-spiro-acceptor complex which shows TADF developed by Stanoppi *et al.*⁴¹

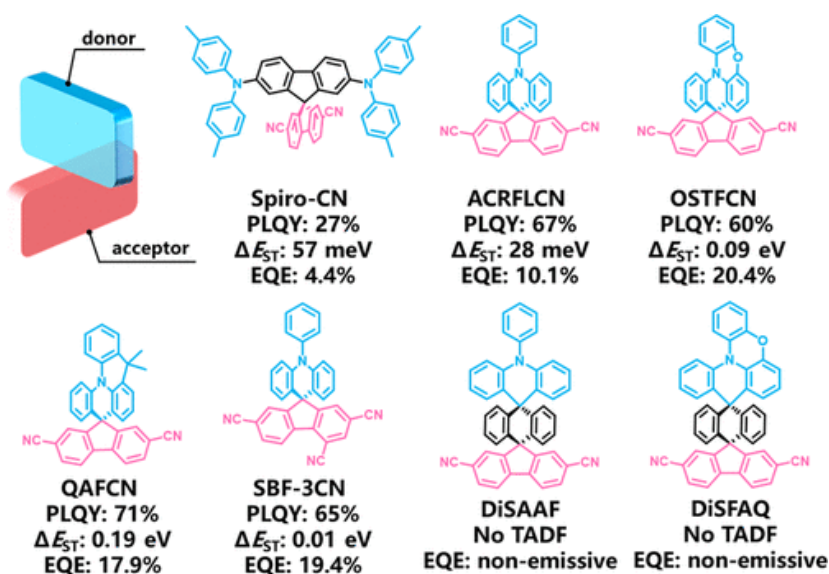


Figure 1.6: Design strategy for D–spiro–A structure and representative materials. Reprinted with permission from ref 29. Copyright 2021 American Chemical Society.

1.4.3 Core-substituted Pyromellitic diimide derivative for dual emission (Phosphorescence and TADF)

Pyromellitic diimides (PmDI) are one class of compounds with four carbonyl groups and as a result, the system is electron deficient by nature. PmDI along with other arylene diimides are an excellent choice for n -type electron transport materials. Apart from that, these materials are also prospects for organic field effect transistors, organic photovoltaics, and batteries for their high air stability. Recently George *et al.* have explored PmDI and its derivatives for triplet harvesting via both phosphorescence and TADF.^{42–46} PmDI with heavy atom substitution are excellent phosphors and have one of the highest IQE reported. While core substitution with a donor-like carbazole moiety also makes PmDI derivatives harness TADF ability and have overall high efficiency (Figure 1.7).⁴⁷ In this regard, dual emissive PmDI derivatives have been explored for their exceptional photophysics.

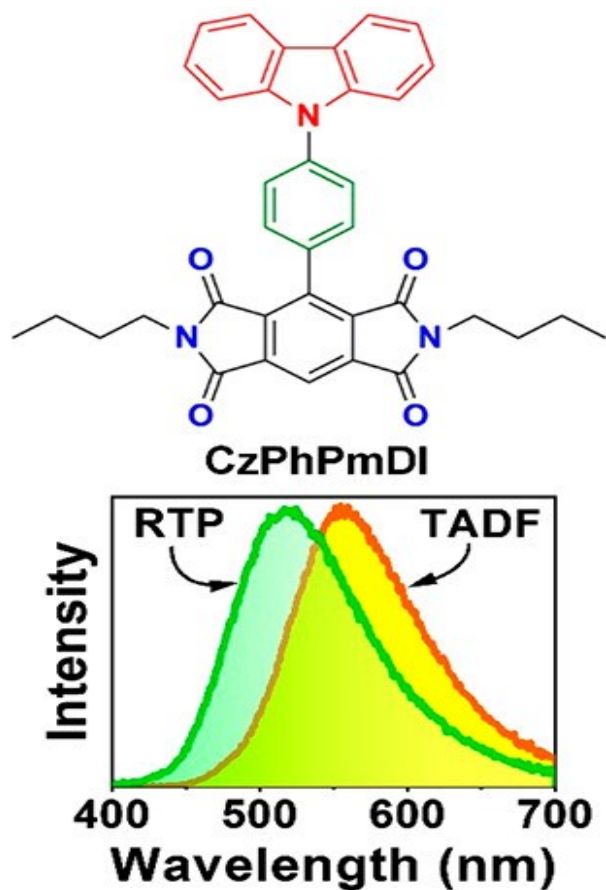


Figure 1.7: CzPhPmDI and its emission characteristics. Reprinted with permission from ref 37. Copyright 2021 American Chemical Society.

1.4.4 Thioxanthone-based triplet sensitizers as efficient photocatalysts

Apart from OLED applications triplet excitons play a huge role in excited state photochemistry. Excited state photochemistry encompasses the process wherein bonds are formed through the interaction of molecules in an electronically excited state. This phenomenon can occur without the involvement of catalysts or reagents, simply through exposure to ultraviolet (UV) light, typically within the range of 250 nm to 400 nm. In a society that is more focused on the economy and the environment, this “reagentless” method of synthesis is very desired.

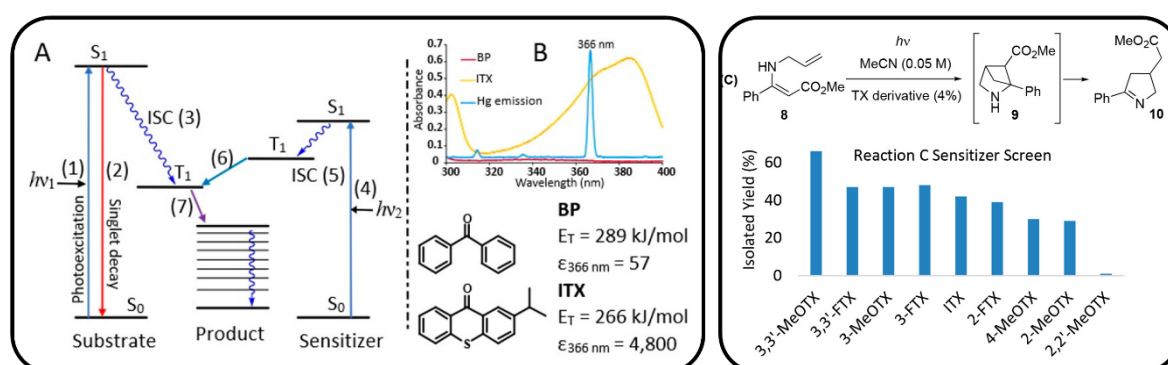


Figure 1.8: (A) Simplified Jablonski diagram of a triplet mediated photochemical reaction: (1) Direct excitation of substrate to S_1 ; (2) Singlet decay by radiative and nonradiative processes; (3) ISC to reactive T_1 ; (4) Photoexcitation of sensitizer; (5) Rapid ISC to T_1 ; (6) Triplet energy transfer to substrate; and (7) Chemical reaction and relaxation to ground state. (B) UV absorption of BP and ITX at 1×10^{-4} M, overlaid with UVA emission from medium pressure Hg lamp and Isolated yields of [2 + 2] retro-Mannich product **10**. Reprinted with permission from ref 53 Copyright 2021 American Chemical Society.

These reactions generally occur at first excited singlet (S_1) and triplet states (T_1). The Relative lifetime of these states compared to the overall reaction rate becomes too important. Specifically short lifetime of the S_1 state makes photochemical reactions quite difficult to control. In this regard, a reaction's total quantum efficiency can be greatly increased by taking advantage of the T_1 state's extended lifespan. Triplet sensitizers are a class of compounds that enhance the population of T_1 state of the reactant by energy transfer, wherever the direct excitation of reactant is not possible. Sensitizers have also made it possible for photoinitiated processes to be scaled up effectively using alternate techniques in addition to providing a conduit for the transmission of energy.⁴⁸⁻⁵¹ Aromatic ketones are key prospects for this kind of

sensitized reaction. One such aromatic ketone, thioxanthone (TX) has a high triplet state energy and long-lived triplet state is a promising candidate for triplet sensitization.⁵² Recently, Elliot *et al.* have synthesized a series of TX derivatives, which have varied absorption energies.⁵³ But the absorption energy is correlated with their ISC quantum yield which in turn determines the efficiency of TX derivative in triplet photosensitization. We have studied detailed excited state characteristics to unravel this phenomenon (Figure 1.8).

1.4.5 TADF-based OLED devices

Since their first discovery in 1987 by Tang and Van Slyke, organic light-emitting diodes (OLEDs) have been the subject of significant research because they represent an extraordinary leap in both display and lighting technology.^{11, 54-59} OLEDs offer better image clarity and contrast, quicker response times and refresh rates, are viewable over larger viewing angles, and are thinner and lighter than current liquid-crystal displays (LCDs).

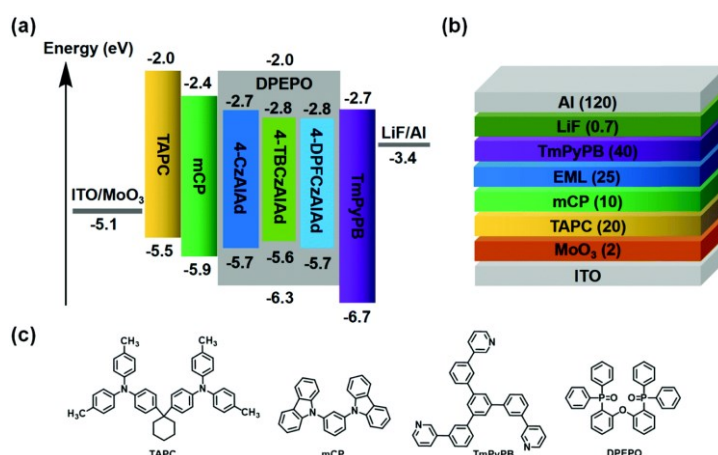


Figure 1.9: (a) Energy level diagrams, (b) OLED device structure and (c) the chemical structure of the materials used in the TADF devices. Ref 60

OLEDs utilise less energy since they don't need a backlighting system, which makes them more energy efficient. If OLEDs are widely used as lighting technology, a large amount of electricity can be saved given that lighting accounts for about 20% of the world's electricity usage. In addition to lowering production costs, there are a number of obstacles that must be solved for OLEDs to be commercially viable for lighting applications, where the cost per unit must be comparable with currently available technology. In this context, significant advancements have been made in the field of

molecular design and the understanding of the electroluminescence (EL) mechanism in thermally activated delayed fluorescence (TADF)-based organic light-emitting diodes (OLEDs). These developments have greatly contributed to the progress in this area. One crucial requirement for achieving high external quantum efficiency (EQE) in TADF-based OLEDs is the favourable alignment of energy levels between the host, guest, hole and electron transporting materials, which promotes efficient energy transfer and improves carrier balance (Figure 1.9).⁶⁰ However, the current strategies aimed at optimizing the performance of TADF-based OLEDs through the selection of suitable host-guest systems in the light-emitting layer and proper electron-hole transporting layers are still insufficient. With the recent development of data-driven approaches (Machine Learning and Deep Learning), we have used ML to predict device efficiency because of significant growth in the research in TADF-based OLED devices.

1.5 Computational Methodology

1.5.1 Schrödinger equation for the solution of electronic structure

Searching for approximate solutions to the non-relativistic time-independent Schrödinger equation (SE) is one of the primary objectives of quantum chemical computations.

$$\hat{H}\Psi = E\Psi \quad (1.16)$$

Where \hat{H} , Ψ and E are the many-body Hamiltonian operator, corresponding wavefunction respectively, which contains all the information of the system and the total energy of the system respectively. For a system containing N_e electrons and N_n nuclei which are interacting with each other, the complete Hamiltonian can be expressed as,

$$\begin{aligned} \hat{H} = & - \sum_{i=1}^{N_e} \frac{\hbar^2 \nabla_i^2}{2m_e} - \sum_{I=1}^{N_I} \frac{\hbar^2 \nabla_I^2}{2M_I} \\ & - \sum_{i=1}^{N_e} \sum_{I=1}^{N_I} \frac{Z_I e^2}{|r_i - R_I|} + \sum_{i=1}^{N_e-1} \sum_{j>i}^{N_e} \frac{e^2}{|r_i - r_j|} + \sum_{I=1}^{N_I-1} \sum_{J>I}^{N_I} \frac{Z_I Z_J e^2}{|R_I - R_J|} \end{aligned} \quad (1.17)$$

Where m_e and M_I are the mass of an electron and mass of the I -th nucleus. The first and second terms of equation 1.17 contain Laplacian operators ∇_i^2 and ∇_I^2 are the kinetic energy operators for the i -th electron and I -th nucleus. The charge of an electron and I -th nucleus are denoted by e and Z_I respectively. The 3rd term denotes the potential energy of the electrostatic attraction of an electron and I -th nucleus. The 4th and 5th term expresses the potential energy electrostatic repulsion between two electron and two nuclei respectively. A simpler complete many-body Hamiltonian from an electron's point of view can be given by the equation,

$$\widehat{H} = \widehat{T}_e + \widehat{T}_N + \widehat{V}_{ext} + \widehat{V}_{int} + \widehat{V}_{nn} \quad (1.18)$$

The electrostatic potential energy term containing both electrons and nuclei is considered external potential, while the term containing only electrons is regarded as internal potential. The SE is analytically solvable for one-electron systems like H-atom and He⁺ systems only in Born-Oppenheimer approximation. In practice, approximations are employed either into the Hamiltonian or wavefunction to get the solution of the SE for a system of our interest (molecules or solids).

1.5.2 Born-Oppenheimer Approximation

The first approximation to simplify the Hamiltonian (equation 1.2) is Born-Oppenheimer (BO) approximation, which considers the nuclei are much heavier than the electron thus separating the electronic and the nuclear motions. Basically, the nuclei will remain effectively stationary during electronic motion and kinetic energies of the nuclei will be negligible compared to that of the electrons. So, within the BO approximation, it is possible to treat the electronic part of the SE independently. The total wavefunction can be expressed as a product of electronic wavefunction and nuclear wavefunction leading to two different SE,

$$\Psi_{tot}(r_i; R_I) = \Psi_e(r_i; R_I)\Psi_N(R_I) \quad (1.19)$$

Where $\Psi_e(r_i; R_I)$ and $\Psi_N(R_I)$ are the electronic wavefunction and nuclear wavefunction respectively. The electronic part of the SE becomes,

$$\widehat{H}_e\Psi_e(r_i; R_I) = E_e(r_i)\Psi_e(r_i; R_I) \quad (1.20)$$

Where $\widehat{H}_e = \widehat{T}_e + \widehat{V}_{ext} + \widehat{V}_{int} + \widehat{V}_{nn}$ and E_e is the electronic eigenvalue and also depends on the nuclear coordinates. Since, fixed nuclear coordinates provide a constant shift to the total energy, \widehat{V}_{nn} is often excluded from the Hamiltonian. Also, it can be added later to get the total energy of the entire system. While the nuclear part can be expressed as,

$$[\widehat{T}_N + E_e(R_I)]\Psi_N(R_I) = E\Psi_N(R_I) \quad (1.21)$$

Where, E is the total energy of the entire system. This way, BO approximation reduces the complexity of the equation 1.3.

1.5.3 Density Functional Theory

Although BO approximation simplifies the problem, finding a solution to SE remains challenging because of the interaction terms. Density functional theory (DFT) is a ground-state quantum mechanical model which reformulates the problem of replacing the information-heavy electronic wavefunction with simple electron density. Since the electronic and nuclear motions are separated because of BO approximation, electrons relax within a static potential $\widehat{V}_{ext}(\mathbf{r})$ created by nuclei. Finally, the electronic Hamiltonian is given by,

$$\widehat{H}_e = -\sum_{i=1}^{N_e} \frac{\hbar^2 \nabla_i^2}{2m_e} + \sum_{i=1}^{N_e-1} \sum_{j>i}^{N_I} \frac{e^2}{|r_i - r_j|} + \widehat{V}_{ext}(\mathbf{r}) \quad (1.22)$$

Still, equation 1.7 is not solvable due to its electron-electron repulsive term. Now, with the help of the Hohenberg-Kohn theorem which couples ground-state electronic density with any physical properties of the system, an approximate solution can be achieved.

1.5.3.1 Hohenberg-Kohn Theorem

Two ingenious theorems proposed by Hohenberg and Kohn in 1964 form the foundations of the DFT.⁶¹⁻⁶³

- **Theorem 1:** *In any system of interacting particles, the external potential $\widehat{V}_{ext}(\mathbf{r})$ is uniquely determined (up to a constant) by the ground state electron density $n_0(\mathbf{r})$.*
- **Theorem 2:** *For any given $\widehat{V}_{ext}(\mathbf{r})$ we can define the energy functional, $E[n(\mathbf{r})]$, in terms of electron density $n(\mathbf{r})$. The density which minimizes the energy functional variationally is the true ground state electron density $n_0(\mathbf{r})$.*

Only the first two terms in equation 1.22 are only dependent on the electrons and obviously similar to any N_e electron system. This is followed by the fact the ground state electron density uniquely determines the remaining term of equation 1.7, which is the external potential $\widehat{V}_{ext}(\mathbf{r})$. So, in principle, any properties of the quantum many-body systems can be calculated using the ground state electron density. But the major problem is, the function that maps the electron density to properties is not trivial to find. Excluding the nuclear kinetic energy and potential energy from nuclear repulsion, equation 1.3 can be rewritten as,

$$\begin{aligned} E_{HK}[n(\mathbf{r})] &= \widehat{T}_e[n(\mathbf{r})] + \widehat{V}_{int}[n(\mathbf{r})] + \int d^3\mathbf{r} \widehat{V}_{ext}(\mathbf{r})n(\mathbf{r}) \\ &= \widehat{F}_{HK}[n(\mathbf{r})] + \int d^3\mathbf{r} \widehat{V}_{ext}(\mathbf{r})n(\mathbf{r}) \end{aligned} \quad (1.23)$$

Where $\widehat{F}_{HK}[n(\mathbf{r})]$ is given by

$$\widehat{F}_{HK}[n(\mathbf{r})] = \widehat{T}_e[n(\mathbf{r})] + \widehat{V}_{int}[n(\mathbf{r})] \quad (1.24)$$

The term $\widehat{F}_{HK}[n(\mathbf{r})]$ contains the kinetic energy of electrons and potential energy arising from electron-electron coulomb repulsion. This term is universal density-dependent and known. In reality, the exact ground state density for a truly interacting system can be determined by performing total energy minimization with respect to $n(\mathbf{r})$ variationally. However, the exact form of external potential limits its ability. Although in 1965 Kohn and Sham formulated a smart way to circumvent this problem, which lead to the substratum of practical use of DFT.

1.5.3.1.1 Kohn-Sham Approach

The main aim of DFT is to find the true ground state electron density which minimizes the total energy of the system. Kohn and Sham proposed that it is possible to find an auxiliary non-interacting system whose ground state electron density exactly resembles the interacting system of our interest. It will be easier to find the solution of the auxiliary system because electrons are independent particles. This non-interacting picture leads to transformation of many-body problem into one particle electron problem, where each electron experiences an effective potential which depends on electron density. With the Kohn-Sham approximation, the SE can be written as a set of independent particle SE,

$$\hat{H}_{KS}\varphi_i(\mathbf{r}) = \left[-\frac{\hbar^2}{2m_e}\nabla_i^2 + V_{KS} \right] \varphi_i(\mathbf{r}) = \varepsilon_i\varphi_i(\mathbf{r}) \quad (1.25)$$

Where φ_i is the independent electron orbital for i -th electron. This is also known as Kohn-Sham orbitals. For a system containing N_e electrons, there are total N_e independent particle SE, which leads to the solution of the entire system. Each Kohn-Sham orbital is occupied by one particle (electron) with the eigenvalue of ε_i , which is the lowest energy of that electron. The electron density of this auxiliary system can be calculated by the following equation,

$$n(\mathbf{r}) = \sum_{i=1}^N |\varphi_i(\mathbf{r})|^2 \quad (1.26)$$

Subjected to the condition $\int n(\mathbf{r})d\mathbf{r} = N$. This density reproduces the density of interacting many-body system.

The kinetic energy functional for the non-interacting auxiliary system is given by,

$$T_S[n(\mathbf{r})] = -\frac{\hbar^2}{2m_e} \sum_{i=1}^N \langle \varphi_i(\mathbf{r}) | \nabla^2 | \varphi_i(\mathbf{r}) \rangle \quad (1.27)$$

Finally, the universal $F_{HK}[n(\mathbf{r})]$ becomes,

$$F_{HK}[n(\mathbf{r})] = T_S[n(\mathbf{r})] + E_H[n(\mathbf{r})] + E_{XC}[n(\mathbf{r})] \quad (1.28)$$

$E_H[n(\mathbf{r})]$ contains the classical Coulomb self-interaction term, which is denoted as, Hartree energy $E_H[n(\mathbf{r})]$. $E_{XC}[n(\mathbf{r})]$ term comes because of the consideration of auxiliary non-interacting system instead of interacting many-body system. This term fills the gap for the kinetic energy difference between interacting many-body system and auxiliary non-interacting system along with the non-classical electron-electron interaction. So, $E_{XC}[n(\mathbf{r})]$ can be expressed as,

$$E_{XC}[n(\mathbf{r})] = (T_e[n(\mathbf{r})] - T_S[n(\mathbf{r})]) + (E_{int}[n(\mathbf{r})] + E_H[n(\mathbf{r})]) \quad (1.29)$$

So, within Kohn-Sham approximation, the ground state energy functional can be expressed as,

$$E_{KS}[n(\mathbf{r})] = T_S[n(\mathbf{r})] + \int d^3r V_{ext}(\mathbf{r})n(\mathbf{r}) + E_H[n(\mathbf{r})] + E_{XC}[n(\mathbf{r})] \quad (1.30)$$

The only unknown term in equation 1.15 is the exchange-correlation term and the success of DFT lies on how good the approximation of $E_{XC}[n(\mathbf{r})]$, so that many-body effects of a fully interacting system can be recovered, which is missing due to the consideration of auxiliary non-interacting system. However, Kohn-Sham formalism provides a practical way to solve the many-body interacting system and calculate the ground state properties.

In DFT, the ground state energy functional is minimized with respect to the constraint $N_e = \text{constant}$. Initially, a particle density is guessed to calculate the effective potential, which is done by differentiating the total energy functional. The effective potential is given by the following expression,

$$V_{KS} = V_{ext} + \int d\mathbf{r}' \frac{n(\mathbf{r}')}{|\mathbf{r} - \mathbf{r}'|} + \frac{\delta E_{XC}[n(\mathbf{r})]}{\delta n(\mathbf{r})} \quad (1.31)$$

From the calculated V_{KS} , equation 1.10 is solved for N_e electrons. The solution of the eigenvalue problem provides the eigenfunctions (Kohn-Sham orbitals). New Kohn-Sham orbitals are used to calculate the new particle density using equation 1.11. Rather than taking the new density, an admixture of old density and new density as the new guess density. This iterative process is performed until a self-consistent

solution is obtained and final density is taken as ground-state electron density. This ground-state electron density is used for further calculations.

1.5.4 Time-Dependent Density Functional Theory

It is evident that DFT explicitly describes an electronic system through the knowledge of its ground state density. Through this approach time-dependent Schrödinger equation (TDSE) cannot be solved. Time-dependent density functional theory reformulates the TDSE, the exact way DFT has done the reformulation of SE by replacing density as a fundamental variable than many-body wavefunction. The TDSE equation for a non-relativistic system can be expressed as,

$$i\hbar \frac{\partial \Psi}{\partial t} = \hat{H} \Psi \quad (1.32)$$

Again, \hat{H} is the Hamiltonian operator of the system. This equation can be considered an initial value problem, which is different from eigenvalue problem required in DFT. The initial information of the system at time $t=0$, enable us to calculate the information (Ψ) at a later time. Within the time-dependent formalism, the equation 1.7 can be rewritten as,

$$\hat{H}_e = - \sum_{i=1}^{N_e} \frac{\hbar^2}{2m_e} \nabla_i^2 + \sum_{i=1}^{N_e-1} \sum_{j>i}^{N_I} \frac{e^2}{|r_i - r_j|} + \widehat{V}_{ext}(\mathbf{r}, t) \quad (1.33)$$

Now the external potential $\widehat{V}_{ext}(\mathbf{r}, t)$ also depends on time. This term can be decomposed as the sum of single-particle potentials,

$$\widehat{V}_{ext}(\mathbf{r}, t) = \sum_{i=1}^{N_e} v_{ext}(r_i; t) \quad (1.34)$$

External potential describing the coulombic interaction between electron and nuclei can be written as,

$$v_{ext}(\mathbf{r}; t) = - \sum_{I=1}^{N_n} \frac{Z_I}{|\mathbf{r} - \mathbf{R}_I(t)|} \quad (1.35)$$

Where Z_I and $\mathbf{R}_I(t)$ denotes the charge and position of the I -th nucleus.

1.5.4.1 Runge-Gross and van Leeuwen's Theorem

While HK theorem laid the foundation of DFT, similar foundation for TDDFT has been established by Runge-Gross in 1984 and practical use of TDDFT became possible because of van Leeuwen's theorem.^{64, 65}

- **Runge-Gross theorem:** *For a given initial state, the time-evolving one-body density $n(\mathbf{r}; t_0)$ has a one-to-one correspondence with the time dependent external potential $\widehat{V}_{ext}(\mathbf{r}, t)$ of the time-evolving interacting electronic system.*
- **van Leeuwen's theorem:** *For a given initial state and time-dependent external potential there exists another initial state and potential generated from non-interacting system such that the density of interacting system is similar to the density of auxiliary non-interacting system at all times.*

Now, constructing the time-dependent Kohn-Sham equation is rather a simple process, with the introduction of auxiliary non-interacting electron which is under the effect of an external local potential V_{KS} . Now, the TDSE for these Kohn-Sham electrons can be written as,

$$i\hbar \frac{\partial \varphi_i(\mathbf{r}; t)}{\partial t} = \widehat{H}_{KS} \varphi_i(\mathbf{r}; t) \quad (1.36)$$

Under the time-dependent formalism, the Kohn-Sham Hamiltonian can be expressed as,

$$\widehat{H}_{KS} = \left[-\frac{\hbar^2}{2m_e} \nabla_i^2 + V_{KS}[n(\mathbf{r}; t)] \right] \quad (1.37)$$

The density of the interacting system at any time can be obtained from the Kohn-Sham orbitals,

$$n(\mathbf{r}; t) = \sum_{i=1}^{N_e} |\varphi_i(\mathbf{r}; t)|^2 \quad (1.38)$$

Similarly, the time dependent effective Kohn-Sham potential can be given by sum of three terms and equation 1.16 can be modified as follows,

$$V_{KS}[n(\mathbf{r}; t)] = V_{ext}(\mathbf{r}; t) + \int d\mathbf{r}' \frac{n(\mathbf{r}'; t)}{|\mathbf{r} - \mathbf{r}'|} + V_{XC}[n(\mathbf{r}; t)] \quad (1.39)$$

In DFT, ground state electron density can be obtained through minimization of total energy. However, in the time-dependent formalism, there is no variational principle based on total energy as the total energy is not conserved. Although the quantum mechanical action is analogous to energy, which is given by,

$$A[\Psi] = \int_{t_0}^{t_1} dt \langle \Psi(t) | i\hbar \frac{\partial}{\partial t} - \hat{H}(t) | \Psi(t) \rangle \quad (1.40)$$

The xc potential can be written as,

$$V_{XC}(\mathbf{r}; t) = \frac{\delta A_{XC}}{\delta n(\mathbf{r}; t)} \quad (1.41)$$

1.5.5 Exchange-Correlation Functionals

1.5.5.1 XC functionals in the context of DFT

DFT becomes exact if the exact form of exchange-correlation functional is known. However, even with approximated exchange-correlation functional it became possible to get the quite accurate description of the exact ground-state density and observables. Few of such approximation will be discusses used widely in the literatures.

- **Local Density Approximation (LDA)**

It is the simplest approximation to the exchange-correlation functional.⁶⁶ The energy per electron is approximated to be equal to the XC energy of a homogeneous electron gas (HEG) of same density. The expression for XC energy functional can be written as,

$$E_{XC}^{LDA}[n(\mathbf{r})] = \int d\mathbf{r} \epsilon_{XC}^{HEG}(n(\mathbf{r}))n(\mathbf{r}) \quad (1.42)$$

For a spin-polarized system, the expression can be rewritten as,

$$E_{XC}^{LDA}[n_{\uparrow}, n_{\downarrow}] = \int dr \epsilon_{XC}^{HEG}(n_{\uparrow}, n_{\downarrow}) n(\mathbf{r}) \quad (1.43)$$

This is also known as the local spin density approximation (LSDA).

Even with such simplification, LSDA works describes bulk solid well. Since inhomogeneity is ignored in the approximation LSDA fails for describing systems where there are sudden density variations occur (e.g. defects in solids). Apart from that binding energies are overestimated. While ground state energies, ionization energies and band gaps of semiconductor materials are severely underestimated in LSDA. Next section focuses on consideration of inhomogeneity in the expression of XC functional which led to further developments.

- **Generalised gradient approximations (GGA)**

Due to local nature of LSDA, the potential value at a given point only depends on the spin densities on that very point. A simple approach to get the variations of spin densities, gradient of spin densities at a given point is also incorporated apart from spin densities. The expression for GGA-XC functional can be written as,

$$E_{XC}^{GGA}[n_{\uparrow}, n_{\downarrow}] = \int dr \epsilon_{XC}^{GGA}(n_{\uparrow}, n_{\downarrow}, \nabla n_{\uparrow}, \nabla n_{\downarrow}) n(\mathbf{r}) \quad (1.44)$$

Widely used GGA functionals are B88 proposed by Becke, PBE proposed by Perdew, Burke, Enzerhof.⁶⁷⁻⁷² GGAs have been used extensively by Quantum Chemistry communities. It showed improvement over the calculations of binding energies and structural aspects. Recently, more accurate functionals based on GGA have been proposed – the meta GGAs.

- **Meta-GGA functionals**

The form of meta-GGA functional can written as,^{73, 74}

$$E_{XC}^{MGGA}[n_{\uparrow}, n_{\downarrow}] = \int dr \epsilon_{XC}^{GGA}(n_{\uparrow}, n_{\downarrow}, \nabla n_{\uparrow}, \nabla n_{\downarrow}, \nabla^2 n_{\uparrow}, \nabla^2 n_{\downarrow}, \tau_{\uparrow}, \tau_{\downarrow}) n(\mathbf{r}) \quad (1.45)$$

Where, $\tau_{\sigma}(\mathbf{r})$ denotes the kinetic energy density.

- **Hybrid Functionals**

Hartree-Fock exchange is combined with XC from many sources, frequently incorporating several kinds of LDA and GGA, leading to the generation of hybrid functionals. B3LYP is an example of hybrid functional ubiquitous in DFT.⁷⁵ B3LYP has the following description,

$$E_{XC}^{B3LYP} = E_X^{LDA} + a_0[E_X^{HF} - E_X^{LDA}] + a_X[E_X^{GGA} - E_X^{LDA}] + a_C[E_C^{GGA} - E_C^{LDA}] + E_C^{LDA} \quad (1.46)$$

Where $a_0=0.20$, $a_X=0.72$, and $a_C=0.81$.

- **Long-range corrected functionals**

Exchange functionals' non-Coulomb component often decays quickly and loses precision over great distances. Therefore, the simulation of processes like electron excitations to higher energy orbitals must be more accurate. To address systems having considerable dispersive interactions, many formalisms have been used. The widely used long-range corrected functionals are ω b97xd, CAMB3LYP, LC- ω b97xd.⁷⁶

77

1.5.6 Non-adiabatic Dynamics

1.5.6.1 Beyond Born-Oppenheimer Approximation

Organic conjugated polymers and biological systems, as well as other optically active molecular materials, are characterised by their high coupling between the electrical and vibrational degrees of freedom. To take into consideration non-adiabatic coupling between excited states, simulations typically need to go beyond the Born-Oppenheimer approximation. In fact, exciton dynamics, photo physics including charge and energy transfer, as well as exciton dissociation and charge recombination, are frequently related to non-adiabatic dynamics. It is essential to comprehend the photoinduced dynamics in such materials in order to accurately describe the emergence, development, and decay of exciton.

1.5.6.2 Equation of motion (EOM) for non-adiabatic dynamics

We have performed the non-adiabatic dynamics (NAMD) simulation using Multi Configuration Time Dependent Hartree (MCTDH) package. Within MCTDH, the wavefunction is written as,

$$\Psi(q_1, q_2, \dots, q_f, t) = \sum_{j_1=1}^{n_1} \dots \sum_{j_f=1}^{n_f} A_{j_1 \dots j_f}(t) \prod_{k=1}^f \varphi_{j_k}^{(K)}(q_k, t) = \sum_J A_J \Phi_J \quad (1.47)$$

f defines the number of degrees of freedom (DOF) and $K=1 \dots f$ labels them. φ are defined as single particle functions (SPFs) and there are n_k SPFs from the DOF labelled as k .

SPFs are expressed as a series sum of product of time dependent coefficients and time independent basis sets,

$$\varphi_{j_k}^{(K)}(q_k, t) = \sum_{l=1}^{N_k} c_{j_k}^{(K)}(t) \chi_l^{(K)}(q_k) \quad (1.48)$$

N_k denotes the number of primitive basis function for K -th DOF.

Considering the Dirac-Frenkel variational principle and with the help of standard gauge condition $i\langle \varphi_l^{(K)} | \dot{\varphi}_j^{(K)} \rangle = 0$, MCTDH's equation of motion can be derived,

$$i\dot{A}_j = \sum_L \langle \Phi_j | H | \Phi_L \rangle A_L \quad (1.49)$$

$$i\dot{\varphi}_j^{(K)} = (1 - P^{(K)}) \sum_{k,l=1}^K (\rho^{(K)-1})_{jl} \langle H \rangle_{lk}^{(K)} \varphi_k^{(K)} \quad (1.50)$$

Within the MCTDH formalism, the projector operator is given as,

$$P^{(k)} = \sum_{j=1}^{n_k} |\varphi_j^{(K)}\rangle \langle \varphi_j^{(K)}| \quad (1.51)$$

This projector operator not only ensures SPFs remain orthogonal but also ensures partial propagation of A -vector is not done in equation 1.50 while SPFs are propagated through the equation 1.51.

Next, we will introduce, singlet hole functions to define the density matrix and mean-field operator.

$$\Psi_l^{(K)} = \sum_{J^K} A_{J^K,l} \Phi_{J^K} \quad (1.52)$$

Where

$$J^K = (j_1, \dots, j_{K-1}, j_{K+1}, j_f) \quad (1.53)$$

$$\Phi_{J^K} = \prod_{v=1, v \neq K}^f \varphi_{j_v}^{(v)} \quad (1.54)$$

$$A_{J^K,l} = A_{j_1, \dots, j_{K-1}, l, j_{K+1}, j_f} \quad (1.55)$$

Now, the density matrix and the mean fields are read as,

$$\rho_{jl}^{(K)} = \langle \Psi_j^{(K)} | \Psi_l^{(K)} \rangle \quad (1.56)$$

$$\langle H \rangle_{jl}^{(K)} = \langle \Psi_j^{(K)} | H | \Psi_l^{(K)} \rangle \quad (1.57)$$

1.5.7 Machine Learning

Machine Learning is a field of computer science that uses algorithms and statistical models to learn through inference and patterns without being explicitly programmed. Mainly, there are three types of machine learning algorithms: (1) Supervised learning; (2) Unsupervised learning; (3) Reinforcement learning (Figure 1.10). In the context of this thesis, we will discuss only about a few supervised learning algorithms for their use in regression problems.

1.5.7.1 Supervised Machine Learning

Supervised machine learning is one of the most common types of machine learning which is used for either regression or classification problems. Each input data is associated with the output data. The main objective of this type of machine learning is to fit the input data to the output data. Next, we will briefly introduce some of the common supervised machine learning algorithms.

1.5.7.1.1 Support Vector Machine

Feature vectors $x_i \in R^p$ of the training samples and output vector $y \in R^m$ solves a primal problem of the following form:

$$\min_{w,b,\zeta,\zeta^*} \frac{1}{2} w^T w + C \sum_{i=1}^n (\zeta_i + \zeta_i^*) \quad (1.58)$$

$$\text{subject to } y_i - w^T \phi(x_i) - b \leq \varepsilon + \zeta_i$$

$$w^T \phi(x_i) + b - y_i \leq \varepsilon + \zeta_i^*$$

$$\zeta_i, \zeta_i^* \geq 0, i = 1, \dots, n$$

Predictions are penalized when they are ε away from a true prediction by ζ_i, ζ_i^* depending upon the positions of the predictions. The further reformulation of primal form into the dual form leads to a solution of the following form:

$$\sum_{i \in SV} (\alpha_i - \alpha_i^*) K(x_i, x) + b \quad (1.59)$$

Where, α_i and α_i^* are the dual coefficients, their difference holds the support vectors and b is the intercept. $K(x_i, x)$ is the kernel, which varies depending on the functionality used in the model.⁷⁸

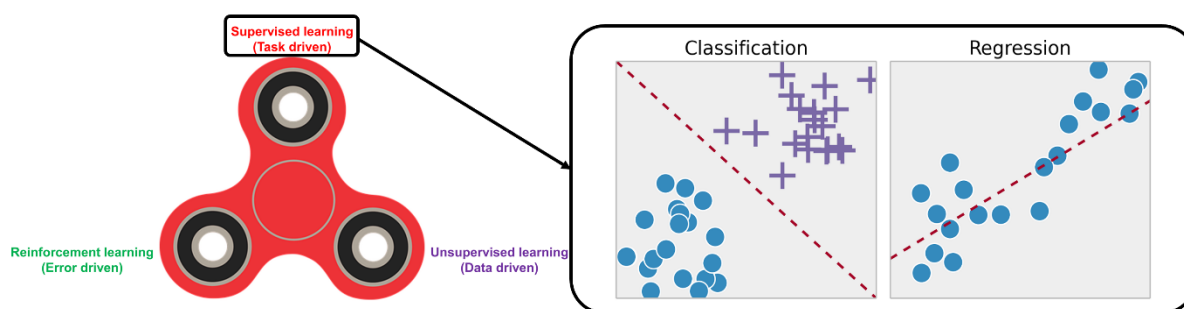


Figure 1.10: Types of machine learning and application of supervised learning

1.5.7.1.2 Decision Tree Regression

For the same feature vectors and output vector of the sample, DT recursively divides the feature space in such a way that similar targets can be grouped together.⁷⁹ A particular node m with N samples, represented by Q_m splits the data based on $\theta =$

j, t_m consisting of a feature j with a threshold t_m into right or left subsets represented by $Q_m^{left}(\theta)$ and $Q_m^{right}(\theta)$,

$$Q_m^{left}(\theta) = (x, y) | x_j \leq t_m \quad (1.60)$$

$$Q_m^{right}(\theta) = Q_m \setminus Q_m^{left}(\theta) \quad (1.61)$$

Split at the given node m is evaluated by a loss function H , which is square loss function in our case,

$$G(Q_m, \theta) = \frac{N_m^{left}}{N} H(Q_m^{left}(\theta)) + \frac{N_m^{right}}{N} H(Q_m^{right}(\theta)) \quad (1.62)$$

Now, optimum parameter has to be calculated,

$$\theta^* = \operatorname{argmin}_{\theta} G(Q_m, \theta) \quad (1.63)$$

1.5.7.1.3 Gradient Boosting

The method was originated by Breiman and developed by Friedman.^{80, 81} GB are additive models, whose predictions y_i for a x_i is of the following form,

$$\hat{y}_i = F_m(x_i) = \sum_{m=1}^M h_m(x_i) \quad (1.64)$$

Where, h_m are the weak learners, in this case, they are DT regressors of finite sizes and like other boosting algorithms GB also works in a greedy fashion.

$$F_m(x) = F_{m-1}(x) + h_m(x) \quad (1.65)$$

The newly added tree h_m are added to reduce the loss function generated by the previous ensemble.

$$h_m(x) = \operatorname{argmin}_h L_m = \operatorname{argmin}_h \sum_{i=1}^n l(y_i, F_m(x)) \quad (1.66)$$

And $l(y_i, F_m(x))$ is the loss parameter. By default, the initial model F_0 is taken to be constant, and the value of l can be approximated as follows,

$$l(y_i, F_{m-1}(x_i) + h_m(x_i)) = l(y_i, F_{m-1}(x_i)) + h_m(x_i) \left[\frac{\partial l(y_i, F(x_i))}{\partial F(x_i)} \right]_{F=F_{m-1}} \quad (1.67)$$

1.5.7.1.4 Extreme gradient boosting

It is highly scalable than GB and Sparsity-aware algorithm that handles sparse data including missing values.⁸² The loss function has a regularization term, so the newly added trees h_m are as follows,

$$h_m(x) = \operatorname{argmin}_h L_m = \operatorname{argmin}_h \sum_{i=1}^n l(y_i, F_m(x)) + \sum_{m=1}^M \Omega(h_m(x)) \quad (1.68)$$

This time objective function has 2nd order term also

$$l(y_i, F_{m-1}(x_i) + h_m(x_i)) = l(y_i, F_{m-1}(x_i)) + h_m(x_i) \left[\frac{\partial l(y_i, F(x_i))}{\partial F(x_i)} \right]_{F=F_{m-1}} + h_m^2(x_i) \left[\frac{\partial^2 l(y_i, F(x_i))}{\partial F(x_i)^2} \right]_{F=F_{m-1}} \quad (1.69)$$

1.6 Softwares Used

The result reported in this thesis obtained from various packages. Major electronic structure calculations (ground and excited state optimization, excitation energy calculations) were done using Gaussian 16 revision A.03 package.⁸³ Spin-orbit coupling matrix elements were calculated using ADF 2017 and ADF 2022 package.⁸⁴ Excited state dynamics were performed using Multi Configuration Time Dependent Hartree (MCTDH) package.⁸⁵ Some postprocessing were done using Multiwfn package.⁸⁶ While the machine learning algorithms were implemented using scikit-learn package. Normal data analysis and plotting were done by numpy, pandas,

matplotlib and seaborn. While visualizations were mostly done by GaussView and VMD.⁸⁷ Whenever required home-grown codes were used to analyse the data.

1.7 Scope of the thesis

In this thesis, we chiefly dealt with the triplet harvesting processes which can be utilized in the form of phosphorescence, TADF by direct emission or sensitization via energy transfer to some other molecule where direct irradiation is not possible. We primarily investigated the excitation nature of relevant singlet or triplet states responsible to direct emissions and also in ISC or rISC processes. These calculations include quantum chemistry algorithms like DFT, TDDFT and excited state dynamics. To the end, we also explored data-driven solutions (Machine learning algorithms) to the device efficiency related problem where direct ab-initio solutions are impracticable.

In the present chapter (**Chapter 1**), we have provided a brief overview of the excitation processes involved in triplet harvesting, importance of triplet harvesting, theoretical perspective on how perturbative missing of states of different spin manifolds give rise the process like phosphorescence, TADF, ISC and rISC which are spin-forbidden in nature. This chapter also includes computational methodologies used in the investigation. In the subsequent chapter (**Chapter 2**), we have explored the rISC mechanism in boron-based donor-spiro-acceptor complex, where low-lying excitations are CT in nature. This leads to drop in spin-orbit coupling matrix elements (SOCME) in the states, which hampers the rISC mechanism. We have shown that an existence of energetically close LE state in triplet manifold establishes the rISC mechanism through a second-order perturbative way. Phosphorescence and TADF are two completely opposite and competing phenomena. In the next two chapters (**Chapter 3 & Chapter 4**), we have investigated the dual phosphorescence and TADF in both mechanochromic luminescent material and PmDI derivatives. We have provided theoretical perspective how different substitution on these systems might enhance the overall internal quantum efficiencies of those systems. In **Chapter 5**, we have probed triplet sensitizers which utilize the triplet excitons in photochemical reaction by transferring the energy to a substrate where direct excitation is not possible. We have delineated the effect of substitution with groups having a mesomeric effect on 3 or 3'

position on TX leads to superior intersystem crossing quantum yield. **Chapter 6** deals with the ML approach for the prediction of efficiency in TADF-based OLEDs.

The thesis ends with the summary (**Chapter 7**) and result obtained in the chapter 2-6 along with an outlook towards possible future research ideas and developments in triplet exciton harvesting and its applications in optoelectronics and photocatalysis.

Bibliography

- [1] D. A. K. Vezzu, D. Ravindranathan, A. W. Garner, L. Bartolotti, M. E. Smith, P. D. Boyle, S. Huo *Inorganic Chemistry*. **2011**, *50*, 8261-8273.
- [2] J. A. G. Williams in *Photochemistry and Photophysics of Coordination Compounds: Platinum, Vol.* (Eds.: V. Balzani, S. Campagna), Springer Berlin Heidelberg, Berlin, Heidelberg, **2007**, pp.205-268.
- [3] Y. Chi, P.-T. Chou *Chemical Society Reviews*. **2010**, *39*, 638-655.
- [4] L. Flamigni, A. Barbieri, C. Sabatini, B. Ventura, F. Barigelletti in *Photochemistry and Photophysics of Coordination Compounds: Iridium, Vol.* (Eds.: V. Balzani, S. Campagna), Springer Berlin Heidelberg, Berlin, Heidelberg, **2007**, pp.143-203.
- [5] A. J. Hallett, B. M. Kariuki, S. J. A. Pope *Dalton Transactions*. **2011**, *40*, 9474-9481.
- [6] J. C. Deaton, R. H. Young, J. R. Lenhard, M. Rajeswaran, S. Huo *Inorganic Chemistry*. **2010**, *49*, 9151-9161.
- [7] A. F. Rausch, H. H. H. Homeier, H. Yersin in *Organometallic Pt(II) and Ir(III) Triplet Emitters for OLED Applications and the Role of Spin-Orbit Coupling: A Study Based on High-Resolution Optical Spectroscopy, Vol.* (Ed. A. J. Lees), Springer Berlin Heidelberg, Berlin, Heidelberg, **2010**, pp.193-235.
- [8] H. Yersin, A. F. Rausch, R. Czerwieniec, T. Hofbeck, T. Fischer *Coordination Chemistry Reviews*. **2011**, *255*, 2622-2652.
- [9] S. C. F. Kui, F.-F. Hung, S.-L. Lai, M.-Y. Yuen, C.-C. Kwok, K.-H. Low, S. S.-Y. Chui, C.-M. Che *Chemistry – A European Journal*. **2012**, *18*, 96-109.
- [10] V. W.-W. Yam, E. C.-C. Cheng *Chemical Society Reviews*. **2008**, *37*, 1806-1813.
- [11] M. Y. Wong, E. Zysman-Colman *Advanced Materials*. **2017**, *29*, 1605444.
- [12] Q. Zhao, F. Li, C. Huang *Chemical Society Reviews*. **2010**, *39*, 3007-3030.
- [13] W. Pauli *Zeitschrift für Physik*. **1925**, *31*, 373-385.
- [14] M. Kasha *Discussions of the Faraday Society*. **1950**, *9*, 14-19.
- [15] A. Köhler, H. Bässler *Materials Science and Engineering: R: Reports*. **2009**, *66*, 71-109.
- [16] S. K. Lower, M. A. El-Sayed *Chemical Reviews*. **1966**, *66*, 199-241.
- [17] M. A. El-Sayed *The Journal of Chemical Physics*. **1963**, *38*, 2834-2838.
- [18] J. Ehrmaier, E. J. Rabe, S. R. Pristash, K. L. Corp, C. W. Schlenker, A. L. Sobolewski, W. Domcke *The Journal of Physical Chemistry A*. **2019**, *123*, 8099-8108.

- [19] H. Ågren, O. Vahtras, B. Minaev in *Response Theory and Calculations of Spin-Orbit Coupling Phenomena in Molecules*, Vol. 27 (Eds.: P.-O. Löwdin, J. R. Sabin, M. C. Zerner), Academic Press, **1996**, pp.71-162.
- [20] C. M. Marian *WIREs Computational Molecular Science*. **2012**, *2*, 187-203.
- [21] D. G. Fedorov, S. Koseki, M. W. Schmidt, M. S. Gordon *International Reviews in Physical Chemistry*. **2003**, *22*, 551-592.
- [22] C. M. Marian in *Spin-Orbit Coupling in Molecules*, Vol., **2001**, pp.99-204.
- [23] P.S *Journal of Molecular Structure*. **1972**, *12*, 310.
- [24] D. R. Yarkony *International Reviews in Physical Chemistry*. **1992**, *11*, 195-242.
- [25] V. Lawetz, G. Orlandi, W. Siebrand *The Journal of Chemical Physics*. **1972**, *56*, 4058-4072.
- [26] G. W. Robinson, R. P. Frosch *The Journal of Chemical Physics*. **1963**, *38*, 1187-1203.
- [27] D. Beljonne, Z. Shuai, G. Pourtois, J. L. Bredas *The Journal of Physical Chemistry A*. **2001**, *105*, 3899-3907.
- [28] X. Zhang, Z. Chi, Y. Zhang, S. Liu, J. Xu *Journal of Materials Chemistry C*. **2013**, *1*, 3376-3390.
- [29] Y. Q. Dong, J. W. Y. Lam, B. Z. Tang *The Journal of Physical Chemistry Letters*. **2015**, *6*, 3429-3436.
- [30] W. A. Morris, T. Liu, C. L. Fraser *Journal of Materials Chemistry C*. **2015**, *3*, 352-363.
- [31] G. Li, Y. Xu, W. Zhuang, Y. Wang *RSC Advances*. **2016**, *6*, 84787-84793.
- [32] Q.-F. Liang, H.-W. Zheng, D.-D. Yang, X.-J. Zheng *CrystEngComm*. **2022**, *24*, 543-551.
- [33] X.-M. Cai, Z. Tang, X. Chen, Y. Lin, X. Zhang, S. Huang *Dyes and Pigments*. **2022**, *204*, 110454.
- [34] P. Data, M. Okazaki, S. Minakata, Y. Takeda *Journal of Materials Chemistry C*. **2019**, *7*, 6616-6621.
- [35] M. Okazaki, Y. Takeda, P. Data, P. Pander, H. Higginbotham, A. P. Monkman, S. Minakata *Chemical Science*. **2017**, *8*, 2677-2686.
- [36] Y. Takeda, T. Kaihara, M. Okazaki, H. Higginbotham, P. Data, N. Tohnai, S. Minakata *Chemical Communications*. **2018**, *54*, 6847-6850.
- [37] Y. Takeda, P. Data, S. Minakata *Chemical Communications*. **2020**, *56*, 8884-8894.

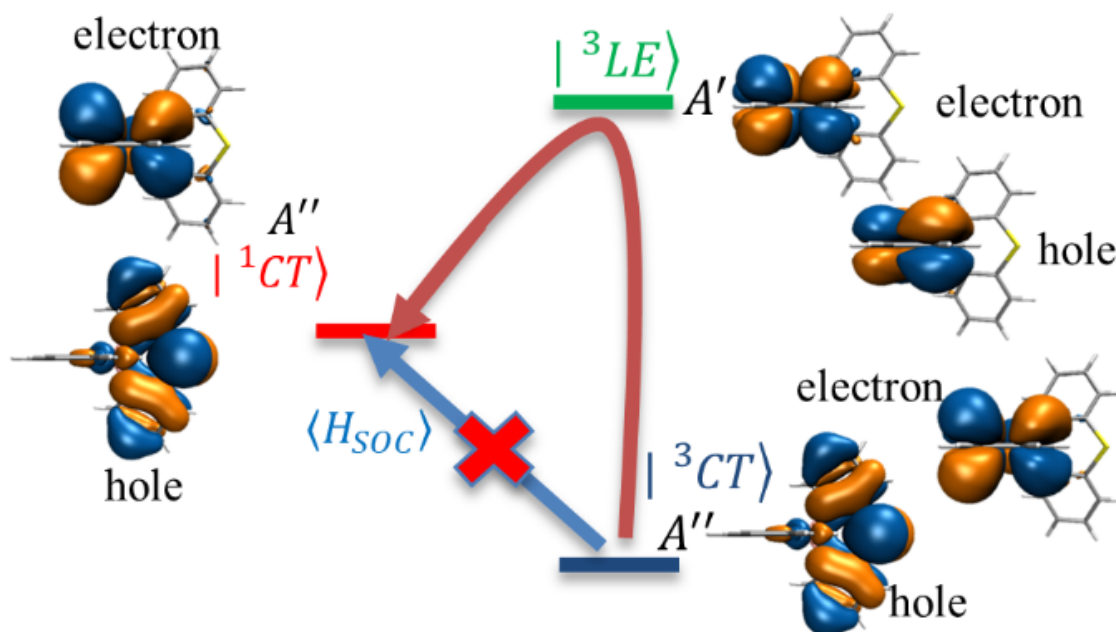
- [38] Y.-K. Qu, Q. Zheng, J. Fan, L.-S. Liao, Z.-Q. Jiang *Accounts of Materials Research*. **2021**, *2*, 1261-1271.
- [39] L. J. Sicard, H.-C. Li, Q. Wang, X.-Y. Liu, O. Jeannin, J. Rault-Berthelot, L.-S. Liao, Z.-Q. Jiang, C. Poriel *Angewandte Chemie International Edition*. **2019**, *58*, 3848-3853.
- [40] L. Sicard, C. Quinton, F. Lucas, O. Jeannin, J. Rault-Berthelot, C. Poriel *The Journal of Physical Chemistry C*. **2019**, *123*, 19094-19104.
- [41] M. Stanoppi, A. Lorbach *Dalton Transactions*. **2018**, *47*, 10394-10398.
- [42] S. Garain, S. M. Wagalgave, A. A. Kongasseri, B. C. Garain, S. N. Ansari, G. Sardar, D. Kabra, S. K. Pati, S. J. George *Journal of the American Chemical Society*. **2022**, *144*, 10854-10861.
- [43] S. Garain, S. Kuila, B. C. Garain, M. Kataria, A. Borah, S. K. Pati, S. J. George *Angewandte Chemie International Edition*. **2021**, *60*, 12323-12327.
- [44] S. Garain, B. C. Garain, M. Eswaramoorthy, S. K. Pati, S. J. George *Angewandte Chemie International Edition*. **2021**, *60*, 19720-19724.
- [45] S. Garain, S. N. Ansari, A. A. Kongasseri, B. Chandra Garain, S. K. Pati, S. J. George *Chemical Science*. **2022**, *13*, 10011-10019.
- [46] X. Zhao, Y. Hou, L. Liu, J. Zhao *Energy & Fuels*. **2021**, *35*, 18942-18956.
- [47] S. Kuila, S. Garain, G. Banappanavar, B. C. Garain, D. Kabra, S. K. Pati, S. J. George *The Journal of Physical Chemistry B*. **2021**, *125*, 4520-4526.
- [48] J. Zhao, W. Wu, J. Sun, S. Guo *Chemical Society Reviews*. **2013**, *42*, 5323-5351.
- [49] N. A. Romero, D. A. Nicewicz *Chemical Reviews*. **2016**, *116*, 10075-10166.
- [50] T. C. Pham, V.-N. Nguyen, Y. Choi, S. Lee, J. Yoon *Chemical Reviews*. **2021**, *121*, 13454-13619.
- [51] K. Chen, Y. Dong, X. Zhao, M. Imran, G. Tang, J. Zhao, Q. Liu. **2019**, *7*.
- [52] N. F. Nikitas, P. L. Gkizis, C. G. Kokotos *Organic & Biomolecular Chemistry*. **2021**, *19*, 5237-5253.
- [53] L. D. Elliott, S. Kayal, M. W. George, K. Booker-Milburn *Journal of the American Chemical Society*. **2020**, *142*, 14947-14956.
- [54] A. Endo, K. Sato, K. Yoshimura, T. Kai, A. Kawada, H. Miyazaki, C. J. A. P. L. Adachi. **2011**, *98*, 42.
- [55] S. Youn Lee, T. Yasuda, H. Nomura, C. Adachi *Applied Physics Letters*. **2012**, *101*, 093306.

- [56] Y. Tao, K. Yuan, T. Chen, P. Xu, H. Li, R. Chen, C. Zheng, L. Zhang, W. Huang *Advanced Materials*. **2014**, *26*, 7931-7958.
- [57] T. Hatakeyama, K. Shiren, K. Nakajima, S. Nomura, S. Nakatsuka, K. Kinoshita, J. Ni, Y. Ono, T. Ikuta *Adv. Mater.* **2016**, *28*, 2777-2781.
- [58] M. K. Etherington, J. Gibson, H. F. Higginbotham, T. J. Penfold, A. P. J. N. c. Monkman. **2016**, *7*, 1-7.
- [59] G. Méhes, H. Nomura, Q. Zhang, T. Nakagawa, C. Adachi *Angewandte Chemie International Edition*. **2012**, *51*, 11311-11315.
- [60] Q. Feng, X. Zheng, H. Wang, H. Zhang, Y. Qian, K. Tan, H. Cao, L. Xie, W. Huang *Materials Advances*. **2021**, *2*, 4000-4008.
- [61] P. Hohenberg, W. Kohn *Physical Review*. **1964**, *136*, B864-B871.
- [62] W. Kohn, L. J. Sham *Physical Review*. **1965**, *140*, A1133-A1138.
- [63] W. Kohn *Reviews of Modern Physics*. **1999**, *71*, 1253-1266.
- [64] E. Runge, E. K. U. Gross *Physical Review Letters*. **1984**, *52*, 997-1000.
- [65] R. van Leeuwen in *Beyond the Runge-Gross Theorem, Vol.* (Eds.: M. A. L. Marques, C. A. Ullrich, F. Nogueira, A. Rubio, K. Burke, E. K. U. Gross), Springer Berlin Heidelberg, Berlin, Heidelberg, **2006**, pp.17-31.
- [66] D. M. Ceperley, B. J. Alder *Physical Review Letters*. **1980**, *45*, 566-569.
- [67] J. P. Perdew, K. Burke, M. Ernzerhof *Physical Review Letters*. **1996**, *77*, 3865-3868.
- [68] J. P. Perdew, Y. Wang *Physical Review B*. **1992**, *45*, 13244-13249.
- [69] J. P. Perdew, J. A. Chevary, S. H. Vosko, K. A. Jackson, M. R. Pederson, D. J. Singh, C. Fiolhais *Physical Review B*. **1992**, *46*, 6671-6687.
- [70] A. D. Becke *Physical Review A*. **1988**, *38*, 3098-3100.
- [71] F. A. Hamprecht, A. J. Cohen, D. J. Tozer, N. C. Handy *The Journal of Chemical Physics*. **1998**, *109*, 6264-6271.
- [72] A. D. Boese, N. L. Doltsinis, N. C. Handy, M. Sprik *The Journal of Chemical Physics*. **2000**, *112*, 1670-1678.
- [73] Y. Zhao, D. G. Truhlar *Theoretical Chemistry Accounts*. **2008**, *120*, 215-241.
- [74] Y. Zhao, D. G. Truhlar *Journal of Chemical Theory and Computation*. **2011**, *7*, 669-676.
- [75] A. D. Becke *The Journal of Chemical Physics*. **1993**, *98*, 5648-5652.
- [76] T. Yanai, D. P. Tew, N. C. Handy *Chemical Physics Letters*. **2004**, *393*, 51-57.

- [77] J.-D. Chai, M. Head-Gordon *Physical Chemistry Chemical Physics*. **2008**, *10*, 6615-6620.
- [78] D. A. Pisner, D. M. Schnyer in *Chapter 6 - Support vector machine, Vol.* (Eds.: A. Mechelli, S. Vieira), Academic Press, **2020**, pp.101-121.
- [79] A. J. Myles, R. N. Feudale, Y. Liu, N. A. Woody, S. D. Brown *Journal of Chemometrics*. **2004**, *18*, 275-285.
- [80] J. H. Friedman *The Annals of Statistics*. **2001**, *29*, 1189-1232.
- [81] J. H. Friedman *Computational Statistics & Data Analysis*. **2002**, *38*, 367-378.
- [82] R. P. Sheridan, W. M. Wang, A. Liaw, J. Ma, E. M. Gifford *Journal of Chemical Information and Modeling*. **2016**, *56*, 2353-2360.
- [83] M. J. Frisch, G. W. Trucks, H. B. Schlegel, G. E. Scuseria, M. A. Robb, J. R. Cheeseman, G. Scalmani, V. Barone, G. A. Petersson, H. Nakatsuji, X. Li, M. Caricato, A. V. Marenich, J. Bloino, B. G. Janesko, R. Gomperts, B. Mennucci, H. P. Hratchian, J. V. Ortiz, A. F. Izmaylov, J. L. Sonnenberg, Williams, F. Ding, F. Lipparini, F. Egidi, J. Goings, B. Peng, A. Petrone, T. Henderson, D. Ranasinghe, V. G. Zakrzewski, J. Gao, N. Rega, G. Zheng, W. Liang, M. Hada, M. Ehara, K. Toyota, R. Fukuda, J. Hasegawa, M. Ishida, T. Nakajima, Y. Honda, O. Kitao, H. Nakai, T. Vreven, K. Throssell, J. A. Montgomery Jr., J. E. Peralta, F. Ogliaro, M. J. Bearpark, J. J. Heyd, E. N. Brothers, K. N. Kudin, V. N. Staroverov, T. A. Keith, R. Kobayashi, J. Normand, K. Raghavachari, A. P. Rendell, J. C. Burant, S. S. Iyengar, J. Tomasi, M. Cossi, J. M. Millam, M. Klene, C. Adamo, R. Cammi, J. W. Ochterski, R. L. Martin, K. Morokuma, O. Farkas, J. B. Foresman, D. J. Fox in *Gaussian 16 Rev. C.01*, Vol. (Ed. ^Eds.: Editor), City, **2016**.
- [84] G. te Velde, F. M. Bickelhaupt, E. J. Baerends, C. Fonseca Guerra, S. J. A. van Gisbergen, J. G. Snijders, T. Ziegler *Journal of Computational Chemistry*. **2001**, *22*, 931-967.
- [85] H. D. Meyer, U. Manthe, L. S. Cederbaum *Chemical Physics Letters*. **1990**, *165*, 73-78.
- [86] T. Lu, F. Chen *Journal of Computational Chemistry*. **2012**, *33*, 580-592.
- [87] W. Humphrey, A. Dalke, K. Schulten *Journal of Molecular Graphics*. **1996**, *14*, 33-38.

Chapter 2

2 Intersystem Crossing in Boron-Based Donor-Spiro-Acceptor Organic Chromophore: A Detailed Theoretical Study*



*Work reported in this chapter is published in: Bidhan Chandra Garain, P. K. Samanta, S. K. Pati, *The Journal of Physical Chemistry A*, 2021, 125 (31), 6674-6680.

2.1 Introduction

Organic light-emitting diodes (OLEDs) are drawing broad attention as they display highly efficient electroluminescence, while they can be prepared with low manufacturing cost and they have lower toxicity.¹⁻⁵ In electroluminescent OLED, charges (electron and hole) are injected from the electrodes, which recombine and generate excitons (hole and electron pairs). The triplet and singlet excitons are generated in a 3:1 ratio according to spin-statistics since there is no spin-correlation during the injection time for electrons and holes. For conventional fluorescence OLEDs, the 25% of singlet excitons decay radiatively, whereas, the 75% of triplet excitons decay non-radiatively. Thus, the internal quantum efficiency (IQE) of conventional fluorescence OLEDs is limited to 25%. Although with the help of triplet-triplet annihilation (TTA), the IQE of conventional fluorescence emitters can be increased to 62.5%, TTA becomes negligible in presence of a large number of hosts (matrix).⁶ Phosphorescent and thermally activated delayed fluorescent (TADF) materials laid a significant foundation in achieving high efficiency (i.e., IQE~100%) with low-cost production. Interestingly, radiative decay occurs from the triplet state in the case of phosphorescent materials, where 25% of singlet excitons can be converted to triplet excitons via intersystem crossing (ISC), making the triplet population 100%. In fact, the TADF materials exploits 75% triplet excitons by converting them to singlet excitons via reverse ISC (rISC) and hence increases the population of singlet states to 100% and shows delayed fluorescence. The rISC is the process of conversion of triplet excitons to singlet excitons.

In TADF materials, the lower energy gap (ΔE_{ST}) and higher spin-orbit coupling (SOC) between the first excited singlet state (S_1) and lowest excited triplet-state (T_1) is very crucial for effective rISC. Standard TADF molecular architecture is made of by the conjunction of donor-acceptor subunits twisted through a single bond or spiro-junction.⁷⁻¹² This induces charge transfer (CT) characteristics in low energy singlet and triplet states and reduces the singlet-triplet energy gap (ΔE_{ST}). On the contrary, SOC matrix element between the CT singlet (1CT) and CT triplet (3CT) state becomes negligible and hence the rISC becomes negligible from 3CT to 1CT .^{13, 14} A few recently synthesized systems have clearly shown quite higher efficiency even violating the above requirement.¹⁵⁻¹⁷ Spiro-CN systems, although have a lower SOC interaction strength between S_1 and T_1 state due to the high CT nature of the excited state, show a

considerable amount of efficiency, which have been explained through an equilibrium thermal population transfer from T_1 to T_2 .^{13, 14}

Hatakeyama *et al.* have synthesized boron-based chromophores which show high quantum efficiency and Northey *et al.* have shown that the exciton transfer pathway occurs from T_2 , which explains its high efficiency although there is a large S_1 - T_1 gap.^{18, 19} Ogiwara *et al.* have proposed that the hyperfine coupling mechanism is required for high rISC between two CT states through electron paramagnetic resonance (EPR) spectroscopy.²⁰ However, recent theoretical studies have shown that the role of vibronic coupling between T_1 (CT) and nearby triplet manifolds is very important apart from the SOC.²¹⁻²⁵ Recently, Stanoppi *et al.* have synthesized boron-based donor-spiro-acceptor chromophores (see Figure 2.1) and observed thermally activated delayed fluorescence (TADF).²⁶ Due to spiro structural arrangement, the highest occupied molecular orbital (HOMO) and lowest unoccupied molecular orbital (LUMO) are spatially separated which leads to CT characteristics in both S_1 and T_1 states.²³ The SOC matrix element between singlet and triplet states with similar CT characteristics (e.g., ^1CT and ^3CT) is quite negligible. However, T_2 is locally excited (LE) and the SOCME between S_1 (i.e., ^1CT) and T_2 (i.e., ^3LE) is significantly higher. Since, both S_1 and T_1 are CT in nature, consideration of ΔE_{ST} and SOC are not enough to calculate rISC from T_1 to S_1 . One needs also to consider the spin-vibronic coupling as well.²¹⁻²³

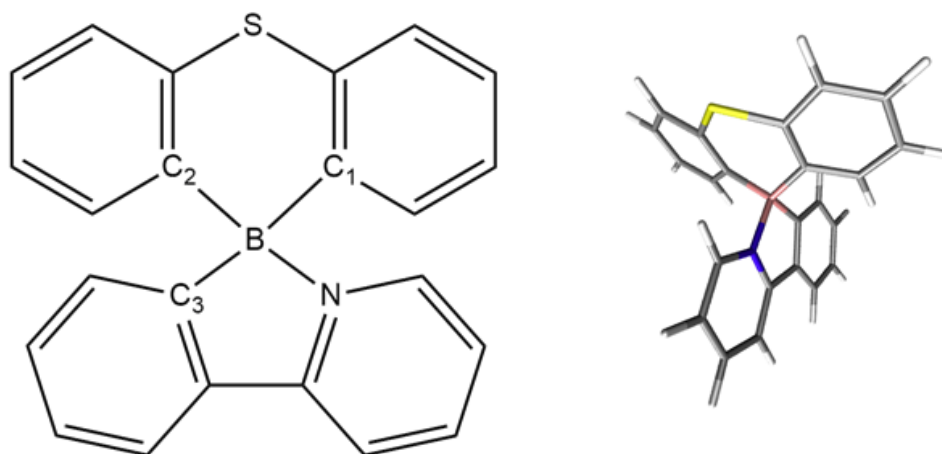


Figure 2.1: Schematic two-dimensional and ground state optimized (3D) structure of the boron-based donor-spiro-acceptor molecule.

In this chapter, we demonstrate that the rISC occurs through a second-order perturbation process where more than two states are involved. Neither the SOC nor the vibronic coupling alone is responsible for the rISC process for the system studied in our work. We believe this study will further be fruitful for understanding the rISC process in TADF systems, where both S_1 and T_1 states are CT in nature and T_2 is LE in nature. rISC occurs from T_1 state to S_1 state through vibronic coupling between T_2 (LE) and T_1 (CT).

2.2 Computational details

The Ground state (S_0) geometry of the molecule was optimized using the density functional theoretical (DFT) method with B3LYP functional and 6-31+g(d,p) basis set.²⁷⁻³⁰ After geometry optimization, frequency calculations were done to confirm the absence of any unstable normal modes. Excited-state potential energy surfaces were constructed using time-dependent DFT (TDA-DFT) method using the above-mentioned functional and basis set which closely corroborates with the experimentally found absorption spectra (Result with other functionals are also given in Table 2.1).

Table 2.1: Low absorption energies (nm) along with oscillator strength (f) using Gaussian 16.

State	B3LYP	Mo6	Mo6-2X	Mo6-HF	CAM-B3LYP	Expt. a [Ref.26]
S_1	436.82 ($f=0.0002$)	414.92 ($f=0.0004$)	320.72 ($f=0.0016$)	285.45 ($f=0.2189$)	313.86 ($f=0.0018$)	
S_2	369.79 ($f=0.0072$)	354.47 ($f=0.0093$)	281.37 ($f=0.0341$)	257.09 ($f=0.0450$)	280.39 ($f=0.3403$)	
S_3	322.66 ($f=0.0235$)	313.97 ($f=0.0863$)	276.87 ($f=0.3260$)	251.82 ($f=0.0185$)	273.30 ($f=0.0406$)	~325
S_4	305.81 ($f=0.0039$)	298.83 ($f=0.1467$)	260.51 ($f=0.0832$)	243.50 ($f=0.0307$)	260.38 ($f=0.0992$)	
S_5	302.74 ($f=0.1458$)	294.48 ($f=0.0026$)	258.53 ($f=0.0295$)	239.61 ($f=0.0517$)	258.31 ($f=0.0124$)	

a) Experimentally observed significant lowest energy peak.

The Tamm-Dancoff approximation (TDA) to TDDFT was used to overcome triplet instability issues.^{31, 32} All the calculations were performed in toluene ($\epsilon = 2.37$) solvent using polarizable continuum model (PCM) to mimic the solvent.³³ These calculations were performed using Gaussian 16, Revision A.03 Package.³⁴ Spin-Orbit Coupling

constants were calculated using ADF package using the B3LYP functional with TZP basis set in conjunction with the COSMO continuum solvation model for toluene.^{35, 36} Spin-orbit coupling effects were considered as a perturbation on the scalar relativistic (SR) orbitals after the SCF and TD-DFT calculations (pSOC-TDDFT).³⁷ Natural transition-orbital (NTO) analysis was performed to characterize the nature of the excited states.³⁸ The quantum dynamics part was performed using the Heidelberg Multi Configuration Time-Dependent Hartree (MCTDH) package.³⁹

2.2.1 Spin-Vibronic Coupling Hamiltonian

The Hamiltonian used for quantum dynamics simulation is proposed by Gibson *et al.* which was based on well-established Linear-Vibronic-Coupling (LVC) mechanism.^{22, 40} The Hamiltonian is given below,

$$\begin{pmatrix} E_{T_1}(Q_0) + \sum_i \frac{\omega_i}{2} \partial_{Q_i}^2 + \frac{\omega_i}{2} Q_i^2 + \frac{\gamma^{T_1}}{2} Q_i^2 + \frac{\varepsilon^{T_1}}{24} Q_i^4 & E_{Soc}^{S1T1} & \sum_i \lambda_i Q_i \\ E_{Soc}^{S1T1} & E_{S1}(Q_0) + \sum_i \frac{\omega_i}{2} \partial_{Q_i}^2 + \frac{\omega_i}{2} Q_i^2 + \frac{\gamma^{S1}}{2} Q_i^2 + \frac{\varepsilon^{S1}}{24} Q_i^4 & E_{Soc}^{S1T2} \\ \sum_i \lambda_i Q_i & E_{Soc}^{S1T2} & E_{T_2}(Q_0) + \sum_i \frac{\omega_i}{2} \partial_{Q_i}^2 + \frac{\omega_i}{2} Q_i^2 + \frac{\gamma^{T_2}}{2} Q_i^2 + \frac{\varepsilon^{T_2}}{24} Q_i^4 \end{pmatrix}$$

The diagonal entries of the diabatic basis are expanded around the Franck-Condon point (Q_0),

$$H_{nn} = E_n(Q_0) + \sum_i \frac{\omega_i}{2} \partial_{Q_i}^2 + \frac{\omega_i}{2} Q_i^2 + \frac{\gamma_i^n}{2} Q_i^2 + \frac{\varepsilon_i^n}{24} Q_i^4 \quad (2.1)$$

where $E_n(Q_0)$ is vertical excitation energy of ground state optimized structure. The ground state energy incorporates both the kinetic energy ($\sum_i \frac{\omega_i}{2} \partial_{Q_i}^2$) and zeroth-order diabatic potential energy ($\frac{\omega_i}{2} Q_i^2 + \frac{\gamma_i^n}{2} Q_i^2 + \frac{\varepsilon_i^n}{24} Q_i^4$) which was assumed to be quartic for the fitting purpose for v_5, v_6, v_{24} . The interstate coupling (off-diagonal term of the LVC Hamiltonian) is defined as,

$$H_{nm} = \sum_i \lambda_i^{nm} Q_i \quad (2.2)$$

At FC point,

$$\lambda_i^{nm} = \sqrt{\frac{1}{8} \frac{\partial^2}{\partial Q_i^2} [V_m(Q) - V_n(Q)]^2} \quad (2.3)$$

V_n and V_m are excited-state adiabatic potential energies of n and m electronic states, respectively. Note that, since the ground state geometry is in C_s point group, the triplet states (T_1 and T_2) considered have A'' and A' symmetry respectively. We have considered only A'' vibrational modes according to Frank-Condon Principle.

Details of the Hamiltonian

Since, both the electron and atoms are moving, we used diabatic representation, best for non-adiabatic dynamics by fixing a point where both diabatic and adiabatic potential energies are same, which is Q_0 (Franck-Condon point). The Hamiltonian is then expanded as a Taylor series around Q_0 using dimensionless normal mode coordinates:

$$H = H^{(0)} + W^{(0)} + W^{(1)} \quad (2.4)$$

$H^{(0)}$ contains adiabatic state energies at Q_0 basically absorption energies at Franck-Condon point. $W^{(0)}$ is the zeroth-order diabatic potential, generally, people consider harmonic oscillator approximation. Only 2nd order based on Q^2 . In this case, potential energy surfaces have plateau at the Franck-Condon point, we used quartic potential (written in the computational details). Since, double well potential is often expressed as,

$$-\frac{Q^2}{4} + \frac{Q^4}{2} \quad (2.5)$$

Plateaus are basically in between harmonic oscillator and double-well. We did it for fitting purposes except for mode 17. The first-order linear coupling matrix is ($W^{(1)}$) written as:

$$W_{ij}^1 = \sum_{\alpha} \left\langle \Phi_i(Q_0) \left| \frac{\partial H_{el}}{\partial Q_{\alpha}} \right| \Phi_j(Q_0) \right\rangle Q_{\alpha} \quad (2.6)$$

In our case, T_1 is A'' and T_2 is A' . So, the vibrations that can couple them according to symmetry rule is A'' :

$$\Gamma_{T1} \times \Gamma_{T2} \times \Gamma_{vib} = A' \quad (2.7)$$

For A' , on diagonal coupling terms are zero. Only off-diagonal elements will be present. We refer to them as λ .

2.2.2 Wavefunction Propagation

In MCTDH, the wave function is approximated as the linear combination of Hartree products.

$$\Psi(Q_1, \dots, Q_f, t) = \sum_1^{n_1} \dots \sum_1^{n_f} A_{j_1 \dots j_f}(t) \prod_{k=1}^f \phi_{j_k}^{(k)}(Q_k, t) \quad (2.8)$$

where Q_1, \dots, Q_f are the nuclear coordinates. $A_{j_1 \dots j_f}(t)$ is the time-dependent expansion coefficient and $\phi_{j_k}^{(k)}$ are the basis functions for k^{th} degrees of freedom which are also time-dependent, known as single-particle functions (SPFs, see Table 2.2).

Table 2.2: MCTDH details of normal mode, primitive basis and single-particle basis used in the dynamics.

modes	Primitive Basis	SPF basis
ν_5	25	(12,12,12)
ν_6	25	(12,12,12)
ν_{17}	25	(12,12,12)
ν_{24}	25	(12,12,12)

2.2.3 Intersystem Crossing rate

Intersystem and reverse intersystem crossing rates were calculated using the Fermi-Golden rule:^{14, 41-44}

$$k_{ISC/rISC}^{nm} = 2\pi/\hbar \rho_{FC} |\langle n | \hat{H}_{SOC} | m \rangle|^2 \quad (2.9)$$

where, $\langle n | \hat{H}_{SOC} | m \rangle$ is the SOC matrix element between two electronic states of different spin-manifolds n and m . ρ_{FC} is Frank-Condon weighted density of states. ρ_{FC} is approximated using semiclassical Marcus theory,⁴⁵⁻⁴⁷

$$\rho_{FC} = \frac{1}{\sqrt{4\pi\lambda_M k_B T}} \exp \left[-\frac{(\Delta E_{nm} + \lambda_M)^2}{4\lambda_M k_B T} \right] \quad (2.10)$$

where λ_M , k_B , T and ΔE_{nm} are the Marcus reorganization energy, Boltzmann constant, temperature and adiabatic energy gap between n and m state, respectively.

2.3 Results and Discussions

2.3.1 Geometry and Optical properties

The molecule under investigation is a boron-based donor-spiro-acceptor organic chromophore. Initial optimized geometry reveals the molecule under investigation is of C_s point group. The B-C bond length is ~ 1.62 Å and B-N bond length is 1.66 Å. Important geometry parameters are given in Table 2.3.

Table 2.3: Ground State Optimized Geometry Parameters.

Bond/Angle	Values
B-C(1)	1.62 Å
B-C(2)	1.62 Å
B-C(3)	1.61 Å
B-N	1.66 Å
C(1)-C(2)-N-C(3) Dihedral Angle ^{a)}	$\sim 74^\circ$

a) C(1)-C(2)-N-C(3) Dihedral angle is close to 90° . It is not 90° due to the non-planar structure of dibenzo-thioborinine.

The HOMO and LUMO are spatially separated π -orbitals with no significant overlap (see Figure 2.2). The HOMO is localized on the donor moiety and the LUMO is localized on the acceptor moiety with an energy gap of 3.45 eV. Calculated absorption energies are provided in Table 2 with detailed electronic configurations. Since S_1 excitation is CT in nature as evident from HOMO (i.e., hole and resides on the donor

part) and LUMO (i.e., electron and resides on the acceptor part), the optical excitation has very low oscillator strength ($f = 0.0001$, see Table 2.4). Initial TDA-DFT investigation shows a major absorption peak at 323 nm to the S_3 excited state with a relatively high oscillator strength ($f = 0.016$) and this is very close to the experimentally observed value of ~ 325 nm.

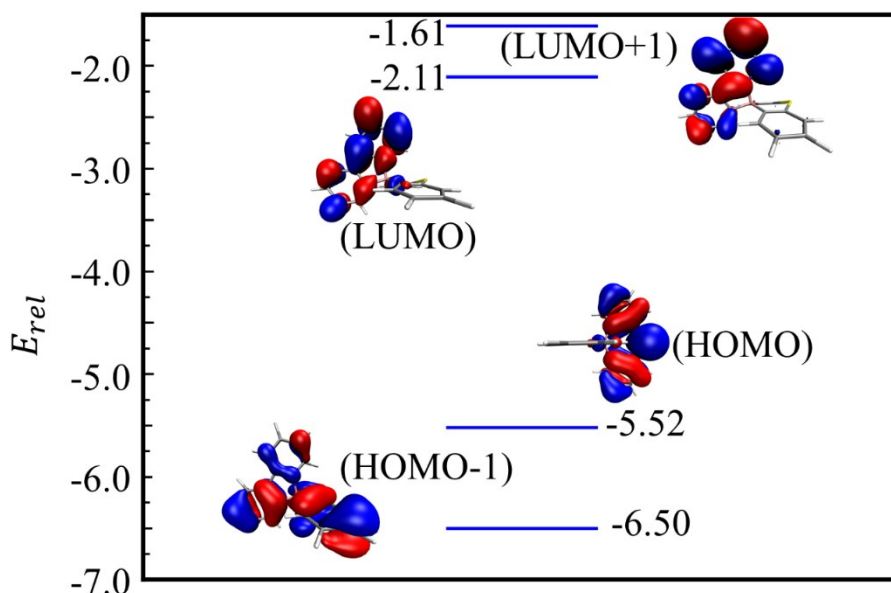


Figure 2.2: Frontier Molecular Orbitals of the boron-based donor-spiro-acceptor molecule. Energy value of each molecular orbital is given in eV.

Table 2.4: Optical Absorption Properties the Boron-Based Donor-Spiro-Acceptor Molecule

State	Symmetry	Energy (eV)	Oscillator strength(f)	Configurations
S_1	A''	2.83	0.0001	$H \rightarrow L$ (99 %)
S_2	A''	3.41	0.0049	$H \rightarrow [L+1]$ (99 %)
S_3	A'	3.81	0.0157	$[H-1] \rightarrow [L+1]$ (96%)

2.3.2 Characteristics of Low Energy Excited States and Spin-orbit Coupling Interaction

Excited state energies along with their transition type and SOCME between states are listed in Table 2.5. The S_1 state energy is 2.83 eV above the energy of the ground state. While, in the case of triplet manifolds, there exist two states; one (T_1) is at 2.81 eV (i.e., below the S_1 state) and is a CT state with an electron-hole distribution similar to the S_1 state and another (T_2) state is at 3.17 eV (i.e., above the S_1 state) and is locally excited (LE) in nature (see Figure 2.3). For the T_2 state, both

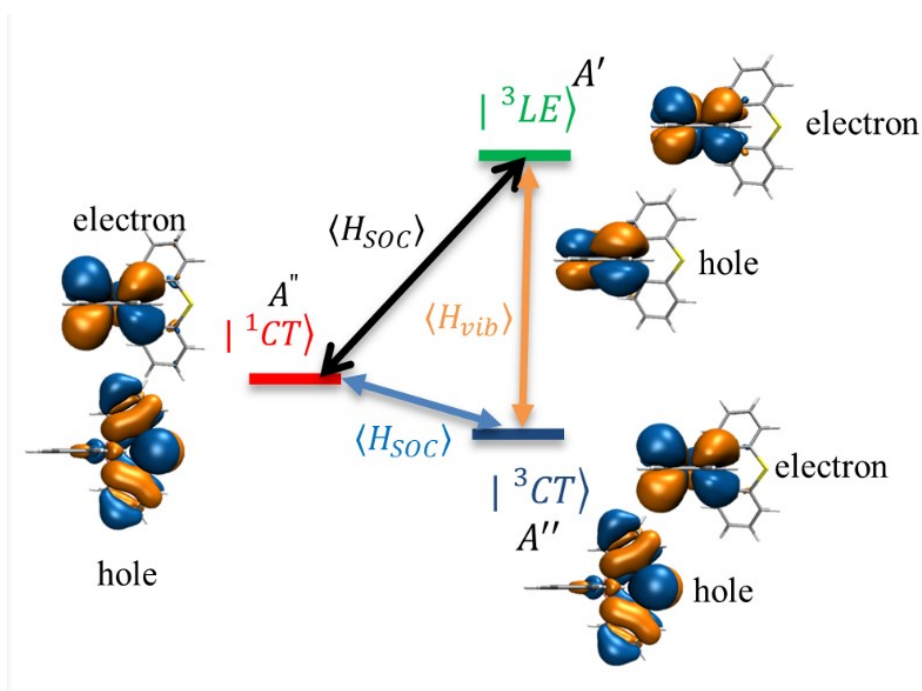


Figure 2.3: Natural transition orbitals and their symmetry calculated using TDA-DFT method.

hole and electron are predominantly localized on the acceptor unit. Since, both S_1 and T_1 are CT in nature, the SOC matrix element is very low (0.078 cm^{-1}). In fact, there is a significant increment in the SOC matrix element between S_1 and T_2 (1.452 cm^{-1}) as they are different in nature (S_1 is CT and T_2 is LE). Such change in the SOC matrix element values can be explained with the help of the \hat{H}_{SO} operator. Under central field approximation, the SOC operator reads as,

$$\hat{H}_{SO} = \sum_{\mu} \sum_i \frac{2c^2}{(2c^2 - V_{\mu i})^2} \frac{1}{r_{\mu i}} \frac{\partial V_{\mu i}}{\partial r_{\mu i}} \left[\frac{1}{2} (\hat{l}_{\mu i+} \hat{s}_{\mu i-} + \hat{l}_{\mu i-} \hat{s}_{\mu i+}) + \hat{l}_{\mu i z} \hat{s}_{\mu i z} \right] \quad (2.11)$$

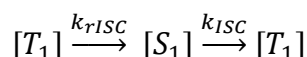
where, $V_{\mu i}$ is the r -dependent potential energy function between electron i and nucleus μ . $\hat{l}_{\pm}[\hat{s}_{\pm}]$ is creation and annihilation operator for the orbital [spin] angular momentum. $\hat{l}_z[\hat{s}_z]$ is the z component of the orbital [spin] angular momentum operator. The operator form implies that the spin-flipping should (either up or down) should be accompanied by orbital flipping (down or up respectively) to conserve the total orbital angular momentum. The system under investigation uses just the p -orbitals for the creation of frontier molecular orbitals. So, accordingly, only the p -orbitals will be affected by the \hat{l}_{\pm} operator. Therefore, upon spin flipping, the orbital arrangement should change. But in the case of S_1 and T_1 states, there is almost no change in the form of the wavefunctions (i.e., hole and electron wavefunctions are very similar for both cases). Thus, SOC matrix element is negligible in the absence of change in orbital angular momentum to conserve total angular momentum. While a certain change in the hole distribution during the spin-flip of S_1 to T_2 makes the SOC matrix element higher.

Table 2.5: Excitation Energies and Spin-orbit Coupling Matrix Elements (SOCME) of Low Energy Excited States.

States/SOCME	Energy	Nature of transition
E_{T_1} (eV)	2.81	CT
E_{S_1} (eV)	2.83	CT
E_{T_2} (eV)	3.17	LE
SOCME between S_1 and T_2 (cm^{-1})	1.452	-
SOCME between S_1 and T_1 (cm^{-1})	0.078	-

2.3.3 Intersystem Crossing (ISC) and Reverse Intersystem Crossing (rISC)

Since we find that the S_1 and T_1 states are quite close by in energy (with small ΔE_{ST}), there is a possibility of intersystem and reverse intersystem crossing between these two states. We have modeled a population transfer (both forward and reverse) between T_1 and S_1 states using Marcus theory for the calculation of k_{ISC} and k_{rISC} .



So, S_1 state population at time t is given by the following expression,

$$[S_1] = [T_1]_0 - \frac{[T_1]_0}{(k_{rISC} + k_{ISC})} (k_{ISC} + k_{rISC} \times e^{-(k_{ISC} + k_{rISC})t}) \quad (2.12)$$

The overall Marcus reorganization energy (λ_M in Eq. 2.10) due to low-frequency intramolecular vibrations and the surrounding medium-induced relaxations can be expected to fall in the range of ~ 0.3 – 0.4 eV. Approximating ΔE_{ST} to be similar to vertical energy difference, for Marcus reorganization energy, $\lambda_M = 0.4$ eV,^{48, 49} the calculated intersystem and reverse intersystem crossing rates are found to be (using Eqn. 2.9 and 2.10), k_{ISC} is $8.12 \times 10^4 \text{ s}^{-1}$, and k_{rISC} is $3.21 \times 10^4 \text{ s}^{-1}$ (see Table 2.6). Although both the k_{ISC} and k_{rISC} are of same order (10^4 s^{-1}), the S_1 state decays non-radiatively, and hence an effective population transfer occurs from T_1 state to S_1 state.

Table 2.6: Intersystem Crossing (ISC) and Reverse Intersystem Crossing (rISC) Rate Constants

Reorganization energy (λ_M)	k_{ISC}	k_{rISC}
$\lambda_M = 0.3 \text{ eV}$	$2.45 \times 10^5 \text{ s}^{-1}$	$9.70 \times 10^4 \text{ s}^{-1}$
$\lambda_M = 0.4 \text{ eV}$	$8.12 \times 10^4 \text{ s}^{-1}$	$3.21 \times 10^4 \text{ s}^{-1}$

Considering, $[T_1]_0 = 100.0$ as the initial population, we get, $[S_1] = 0.0003$ after 100 ps (using Eq. 2.12 and Table 2.6), which is quite negligible based on first-order

perturbation theory. However, the quantum dynamics simulation, which is based on second-order perturbation theory showed that the T_2 state plays a significant role during the population transfer from T_1 to S_1 state. Based on the model mentioned in the computational methodology (Section 2.2.1), we have used four A" vibrations (ν_5 , ν_6 , ν_{17} , ν_{24}) to calculate the inter-state vibrational coupling parameters (see Table 2.7) between T_1 and T_2 states (see Figure 2.4).

Table 2.7: Fitting Parameters for All Four Modes in eV

	ν_5	ν_6	ν_{17}	ν_{24}
ω	0.0118	0.0135	0.0433	0.0587
λ_{13}	0.0226	0.0166	0.0100	0.0309
ϵ^{T1}	0.0054	0.0045	--a	0.0004
γ^{T1}	-0.0049	-0.0016	--a	-0.0096
ϵ^{S1}	0.0054	0.0046	--a	-0.0007
γ^{S1}	-0.0076	-0.0025	--a	-0.0125
ϵ^{T2}	0.0051	0.0048	--a	0.0001
γ^{T2}	-0.0045	-0.0014	--a	-0.0095

a) corresponds to the zeroth order diabatic potential approximation within Harmonic oscillator.

2.3.4 Quantum Dynamics of The Low Energy Excited States

The relative population percentage of 1CT state after 100 ps is shown in Figure 2.5 (initially populated at 3CT state). In Figure 2.5a, we find that as the gap between the 3LE (i.e., T_2) state with the corresponding 1CT (i.e., S_1) and 3CT (i.e., T_1) states are decreased, there occurs significant exciton transfer. When 3LE is very high in energy (3.17 eV), after 100ps the total 1CT population is 0.0007% (similar to what we obtained from the semi-classical calculation). But, at similar energy of T_1 and T_2 , the total population of 1CT state is 0.20% (~600 times increment although the energy gap between 1CT and 3CT remains the same). Following the above trend, we investigated the role of both SOC and vibronic coupling when 3LE is close to 1CT state. Figure 2.5b

reveals that neither the SOC nor the vibronic coupling is alone responsible to increase the population in ^1CT state from ^3CT state. Thus, it is clear that both the SOC and vibronic coupling are required for the rISC processes from ^3CT state to ^1CT state.

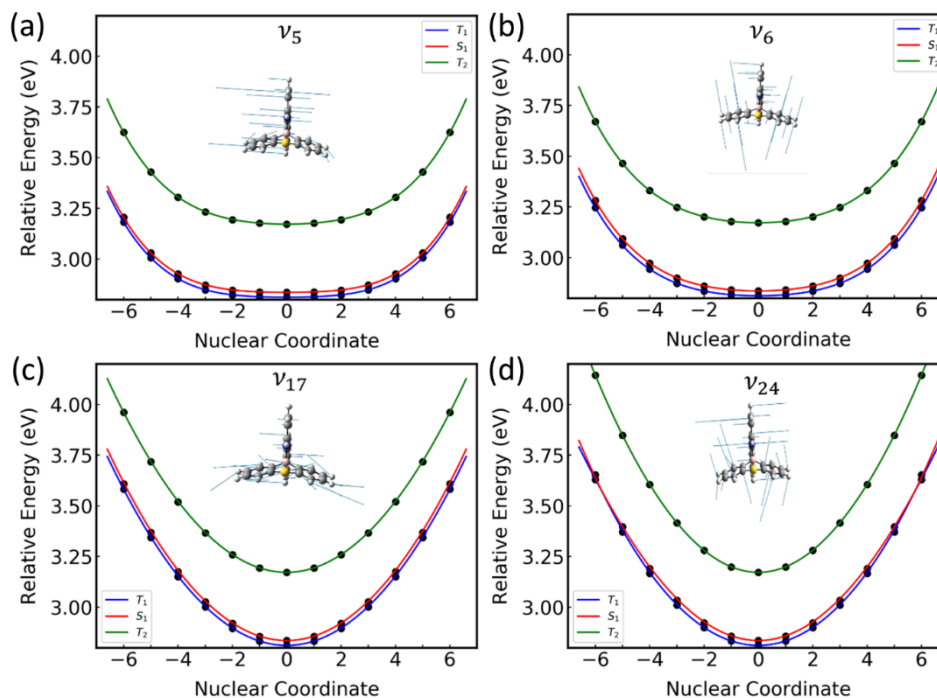


Figure 2.4: Potential energy fitting to the vibronic coupling Hamiltonian for S_1 (red), T_1 (blue) and T_2 (green) with four different low energy vibrational modes (a) v_5 , (b) v_6 , (c) v_{17} and (d) v_{24} which have coupling strength of $> 50 \text{ cm}^{-1}$.

Further analysis of triplet states at two extreme energy values of ^3LE state (see Figure 2.6), reveals that at a very high energy gap, ^3LE state is not getting populated significantly, which is responsible for such lower exciton transfer to ^1CT state and thereby reducing the efficiency of the chromophore. However, if the gap can be

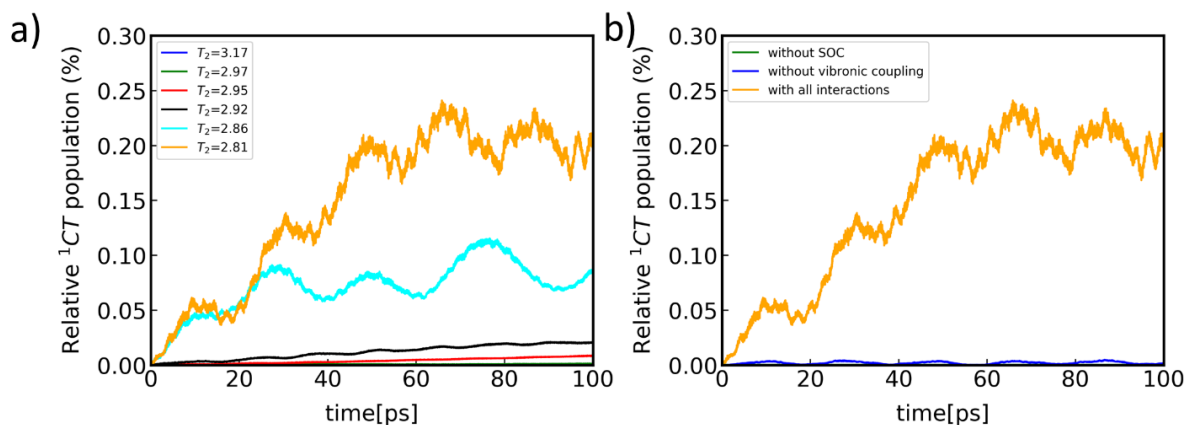


Figure 2.5: (a) Relative population of ^1CT state with varying energy level of ^3LE .; (b) Relative population of ^1CT without the effect of SOC and without vibronic coupling (interstate coupling value is zero) at $E_{T_2} = 2.81$ eV. All the cases ^3CT (i.e., T_1) state

reduced between ^3CT and ^3LE , ^3CT can efficiently populate ^3LE , which later on can transfer the exciton to ^1CT through SOC interaction and at similar energy a rapid transfer is happening from T_1 to T_2 and throughout the rest of the simulation time they maintain almost a constant population ($\sim 50\%$). Based on this argument, it is very important to generate a ^3LE state in the proximity of the CT states for an improved exciton transfer through rISC. Even a recent study of Santos *et al* on a DAD-triad, DPO-TXO₂ showed that triplet-singlet state arrangement engineering can be done through the embedding of different environments.²⁶

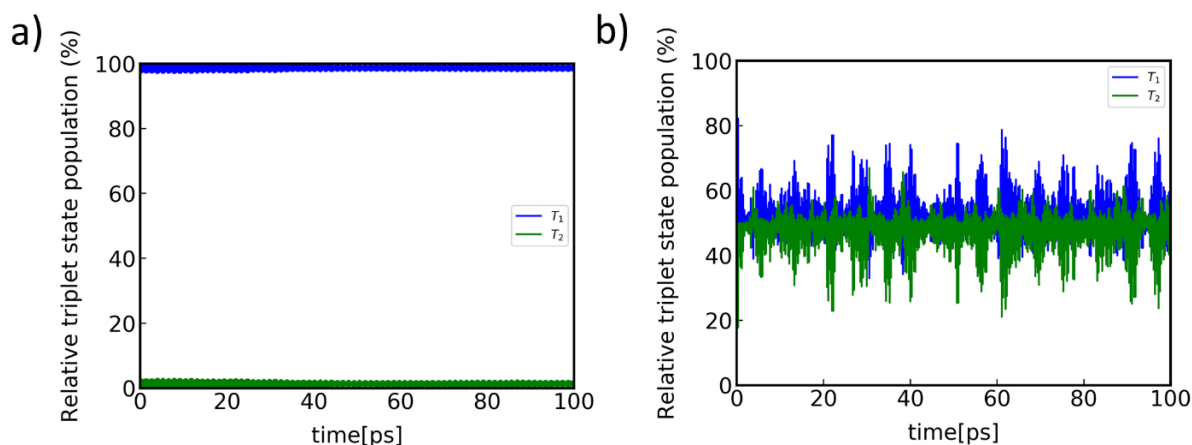


Figure 2.6: (a) Relative population of ^3CT and ^3LE at ^3LE energy level at 3.17 eV (i.e., when the ^3LE and ^3CT gap is higher ~ 0.36 eV); (b) Relative population of ^3CT and ^3LE at ^3LE energy level at 2.81 eV (i.e., when the ^3LE and ^3CT gap is ~ 0 eV).

Thus, the vibronic coupling cannot efficiently populate T_2 state and rISC process from T_1 to S_1 through T_2 fails for the high energy gap between T_1 and T_2 states. A

smaller gap (<0.1 eV) between T_1 and T_2 states efficiently establishes the rISC route in boron-based donor-spiro-acceptor organic chromophores.

2.4 Conclusions

In this chapter, we have investigated the rISC pathway in a boron-based donor-spiro-acceptor organic chromophore which shows TADF properties. Due to the perpendicular arrangement between donor and acceptor moiety, HOMO and LUMO are spatially separated and show CT transition. Although both S_1 and T_1 excited states are CT in nature, T_2 which is above the S_1 and T_1 , and is locally excited in nature (both electron and hole wavefunction are localized on acceptor unit). Because of the same nature of excitation (i.e., CT), the SOC matrix elements between S_1 and T_1 are very low and thus negligibly small exciton transfer occurs from T_1 state to S_1 state (and vice versa). Our quantum dynamics simulation shows rISC process from T_1 state to S_1 state can be improved by the presence of a nearby local excited triplet state (i.e., T_2 state here). But, if there is a high energy gap between T_1 and T_2 states, the vibronic coupling cannot efficiently populate T_2 state and rISC process from T_1 to S_1 through T_2 fails. A smaller gap between T_1 and T_2 states is required to efficiently establish rISC route. The results should promote the development of boron based TADF emitters for applications in organic optoelectronic technologies.

Bibliography

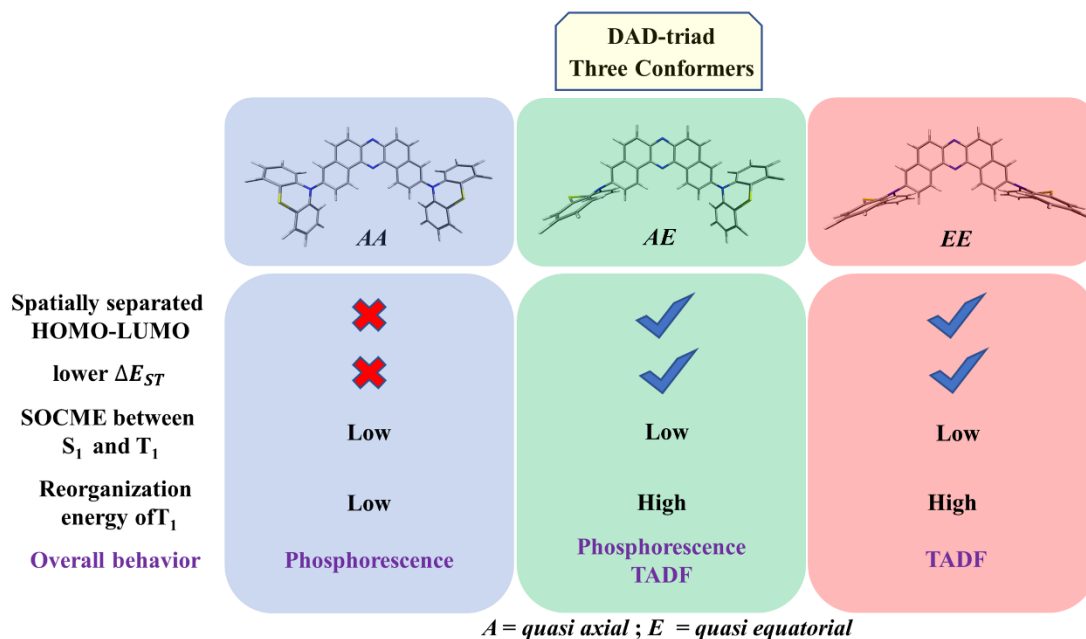
- [1] M. Baldo, M. E. Thompson, S. Forrest *Nature*. **2000**, *403*, 750-753.
- [2] R. C. Evans, P. Douglas, C. J. Winscom *Coord. Chem. Rev.* **2006**, *250*, 2093-2126.
- [3] K. T. Kamtekar, A. P. Monkman, M. R. Bryce *Adv. Mater.* **2010**, *22*, 572-582.
- [4] S. Lamansky, P. Djurovich, D. Murphy, F. Abdel-Razzaq, H.-E. Lee, C. Adachi, P. E. Burrows, S. R. Forrest, M. E. Thompson *J. Am. Chem. Soc.* **2001**, *123*, 4304-4312.
- [5] Y. Sun, N. C. Giebink, H. Kanno, B. Ma, M. E. Thompson, S. R. Forrest *Nature*. **2006**, *440*, 908-912.
- [6] C. J. Chiang, A. Kimyonok, M. K. Etherington, G. C. Griffiths, V. Jankus, F. Turksoy, A. P. Monkman *Adv. Funct. Mater.* **2013**, *23*, 739-746.
- [7] G. Méhes, H. Nomura, Q. Zhang, T. Nakagawa, C. Adachi *Angew. Chem. Int. Ed.* **2012**, *51*, 11311-11315.
- [8] H. Nakanotani, T. Higuchi, T. Furukawa, K. Masui, K. Morimoto, M. Numata, H. Tanaka, Y. Sagara, T. Yasuda, C. Adachi *Nat. Commun.* **2014**, *5*, 1-7.
- [9] K. Nasu, T. Nakagawa, H. Nomura, C.-J. Lin, C.-H. Cheng, M.-R. Tseng, T. Yasuda, C. Adachi *Chem. Commun.* **2013**, *49*, 10385-10387.
- [10] R. Dhali, D. A. Phan Huu, F. Terenziani, C. Sissa, A. Painelli *J. Chem. Phys.* **2021**, *154*, 134112.
- [11] R. Dhali, D. A. P. Huu, F. Bertocchi, C. Sissa, F. Terenziani, A. Painelli *Phys. Chem. Chem. Phys.* **2021**, *23*, 378-387.
- [12] A. K. Pal, K. Bhattacharyya, A. Datta *J. Phys. Chem. A*. **2020**.
- [13] T. Nakagawa, S.-Y. Ku, K.-T. Wong, C. Adachi *Chem. Commun.* **2012**, *48*, 9580-9582.
- [14] P. K. Samanta, D. Kim, V. Coropceanu, J.-L. Brédas *J. Am. Chem. Soc.* **2017**, *139*, 4042-4051.
- [15] X.-K. Chen, B. W. Bakr, M. Auffray, Y. Tsuchiya, C. D. Sherrill, C. Adachi, J.-L. Brédas *J. Phys. Chem. Lett.* **2019**, *10*, 3260-3268.
- [16] T. Hatakeyama, K. Shiren, K. Nakajima, S. Nomura, S. Nakatsuka, K. Kinoshita, J. Ni, Y. Ono, T. Ikuta *Adv. Mater.* **2016**, *28*, 2777-2781.
- [17] H. Tsujimoto, D.-G. Ha, G. Markopoulos, H. S. Chae, M. A. Baldo, T. M. Swager *J. Am. Chem. Soc.* **2017**, *139*, 4894-4900.
- [18] C.-Y. Chan, M. Tanaka, Y.-T. Lee, Y.-W. Wong, H. Nakanotani, T. Hatakeyama, C. Adachi *Nat. Photon.* **2021**, *15*, 203-207.
- [19] T. Northey, T. Penfold *Org. Electron.* **2018**, *59*, 45-48.

- [20] T. Ogiwara, Y. Wakikawa, T. Ikoma *J. Phys. Chem. A.* **2015**, *119*, 3415-3418.
- [21] X.-K. Chen, S.-F. Zhang, J.-X. Fan, A.-M. Ren *J. Phys. Chem. C.* **2015**, *119*, 9728-9733.
- [22] J. Gibson, A. P. Monkman, T. J. Penfold *ChemPhysChem.* **2016**, *17*, 2956.
- [23] C. M. Marian *J. Phys. Chem. C.* **2016**, *120*, 3715-3721.
- [24] Q. Peng, Y. Niu, Q. Shi, X. Gao, Z. Shuai *J. Chem. Theory Comput.* **2013**, *9*, 1132-1143.
- [25] M. K. Etherington, J. Gibson, H. F. Higginbotham, T. J. Penfold, A. P. Monkman *Nat. Commun.* **2016**, *7*, 1-7.
- [26] M. Stanoppi, A. Lorbach *Dalton Trans.* **2018**, *47*, 10394-10398.
- [27] A. D. Becke *J. Chem. Phys.* **1993**, *98*, 5648-5646.
- [28] C. Lee, W. Yang, R. G. Parr *Phys. Rev. B.* **1988**, *37*, 785.
- [29] P. J. Stephens, F. J. Devlin, C. F. Chabalowski, M. J. Frisch *J. Phys. Chem.* **1994**, *98*, 11623-11627.
- [30] S. H. Vosko, L. Wilk, M. Nusair *Can. J. Phys.* **1980**, *58*, 1200-1211.
- [31] S. Hirata, M. Head-Gordon *Chem. Phys. Lett.* **1999**, *314*, 291-299.
- [32] M. J. Peach, M. J. Williamson, D. J. Tozer *J. Chem. Theory Comput.* **2011**, *7*, 3578-3585.
- [33] G. Scalmani, M. J. Frisch *J. Chem. Phys.* **2010**, *132*, 114110.
- [34] M. J. Frisch, G. W. Trucks, H. B. Schlegel, G. E. Scuseria, M. A. Robb, J. R. Cheeseman, G. Scalmani, V. Barone, G. A. Petersson, H. Nakatsuji, X. Li, M. Caricato, A. V. Marenich, J. Bloino, B. G. Janesko, R. Gomperts, B. Mennucci, H. P. Hratchian, J. V. Ortiz, A. F. Izmaylov, J. L. Sonnenberg, Williams, F. Ding, F. Lipparini, F. Egidi, J. Goings, B. Peng, A. Petrone, T. Henderson, D. Ranasinghe, V. G. Zakrzewski, J. Gao, N. Rega, G. Zheng, W. Liang, M. Hada, M. Ehara, K. Toyota, R. Fukuda, J. Hasegawa, M. Ishida, T. Nakajima, Y. Honda, O. Kitao, H. Nakai, T. Vreven, K. Throssell, J. A. Montgomery Jr., J. E. Peralta, F. Ogliaro, M. J. Bearpark, J. J. Heyd, E. N. Brothers, K. N. Kudin, V. N. Staroverov, T. A. Keith, R. Kobayashi, J. Normand, K. Raghavachari, A. P. Rendell, J. C. Burant, S. S. Iyengar, J. Tomasi, M. Cossi, J. M. Millam, M. Klene, C. Adamo, R. Cammi, J. W. Ochterski, R. L. Martin, K. Morokuma, O. Farkas, J. B. Foresman, D. J. Fox in *Gaussian 16 Rev. C.01*, Vol. (Ed. ^Eds.: Editor), City, **2016**.
- [35] G. t. Te Velde, F. M. Bickelhaupt, E. J. Baerends, C. Fonseca Guerra, S. J. van Gisbergen, J. G. Snijders, T. Ziegler *J. Comput. Chem.* **2001**, *22*, 931-967.
- [36] URL: <http://www.scm.com>. **2017**.

- [37] F. Wang, T. Ziegler *The Journal of chemical physics*. **2005**, *123*, 154102.
- [38] R. L. Martin *J. Chem. Phys.* **2003**, *118*, 4775-4777.
- [39] M. H. Beck, A. Jäckle, G. A. Worth, H.-D. Meyer *Phys. Rep.* **2000**, *324*, 1-105.
- [40] H. Köppel, W. Domcke, L. S. Cederbaum *Adv. Chem. Phys.* **1984**, *57*, 59-246.
- [41] V. Lawetz, G. Orlandi, W. Siebrand *J. Chem. Phys.* **1972**, *56*, 4058-4072.
- [42] G. W. Robinson, R. Frosch *J. Chem. Phys.* **1963**, *38*, 1187-1203.
- [43] K. Schmidt, S. Brovelli, V. Coropceanu, D. Beljonne, J. Cornil, C. Bazzini, T. Caronna, R. Tubino, F. Meinardi, Z. Shuai, J.-L. Brédas *J. Phys. Chem. A*. **2007**, *111*, 10490-10499.
- [44] P. K. Samanta, N. J. English *J. Phys. Chem. C*. **2020**, *124*, 8178-8185.
- [45] P. L. Santos, J. S. Ward, P. Data, A. S. Batsanov, M. R. Bryce, F. B. Dias, A. P. Monkman *J. Mater. Chem. C*. **2016**, *4*, 3815-3824.
- [46] D. Beljonne, Z. Shuai, G. Pourtois, J. Bredas *J. Phys. Chem. A*. **2001**, *105*, 3899-3907.
- [47] Q. Ou, J. E. Subotnik *J. Phys. Chem. C*. **2013**, *117*, 19839-19849.
- [48] S. V. K. Isukapalli, R. Lekshmi, P. K. Samanta, S. R. Vennapusa *J. Chem. Phys.* **2020**, *153*, 124301.
- [49] P. K. Samanta, S. K. Pati *J. Mol. Model.* **2018**, *24*, 1-11.

Chapter 3

3 Delineating Conformation Control in the Photophysical Behaviour of a Molecular Donor-Acceptor-Donor Triad*



*Work reported in this chapter is published in: Bidhan Chandra Garain, Shubhajit Das, Swapan K. Pati, *ChemPhysChem*, 2021, 22 (22), 2297-2304.

3.1 Introduction

In the past few years, research on designing OLED based on small organic chromophore (through mainly Phosphorescence or thermally activated delayed fluorescence) has shown significant escalation.¹⁻⁴ In fact, the field has witnessed significant activity in OLED-research based on small organic chromophores exhibiting Room Temperature Phosphorescence (RTP) or Thermally Activated Delayed Fluorescence (TADF). These systems are synthetically viable for large-scale production and usually manifest high internal quantum efficiency.⁵⁻⁷ Phosphorescent materials directly utilize the triplet excitons for luminescence while materials with TADF properties deploy the same through reverse inter-system crossing (rISC) by converting them to singlet excitons. The synthetic blueprint of a phosphorescent material typically involves the inclusion of heavy atoms to increase the spin-orbit coupling (SOC) promoting ISC.⁸ Although smaller organic chromophores lack this component, an alternative strategy is to increase the SOC through the incorporation of hetero-atoms to induce change in orbital type ($n-\pi^*$ or $\pi-\pi^*$) during electronic transitions between singlet and triplet manifolds.⁹

The most common strategy for synthesizing a TADF material is to construct donor (D)-acceptor (A) systems with an appropriate arrangement (twisted bond or spiro-junction) between them so that they have less overlap between their HOMO and LUMO. This will ensure CT characteristics in singlets and triplet states and due to

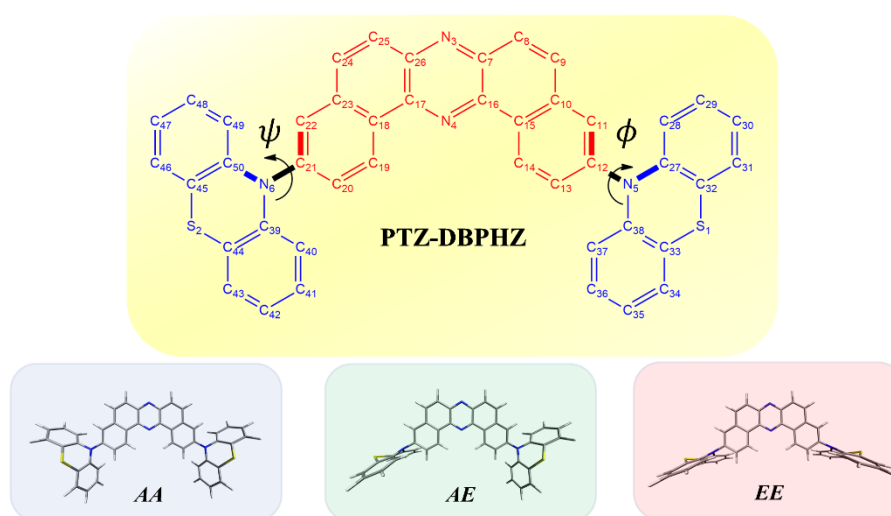


Figure 3.1: Molecular structure of the PTZ-DBPHZ D-A-D triad along with the 3D representation of three conformers.

negligible overlap, the singlet-triplet gap also reduces. Along with donor and acceptor arrangements, variation of units based on their electron-donating and withdrawing strength is also important for the reduction of ΔE_{ST} . In this way, triplet excitons can be transformed into singlet excitons easily through the up-conversion inter-system crossing method. In fact, this way the ISC from singlet to triplet states would occur which will compete with the radiative transition from S_1 , and this may overall help in generating phosphorescence quite effectively.

Interestingly, the mechanochromic luminescent (MCL) materials that exhibit varying emissive properties induced by external stimuli (such as heat, pressure, pH level of solution, electric field) find a wide range of applications in bio-imaging, stress detection and LCD screens.¹⁰⁻¹⁷ The MCL behaviour is typically observed in liquid crystals, organic and organometallic crystals as demonstrated by Ma, Kim, Matsunaga as well as Park amongst others.¹⁰⁻¹² For example, Kato reported a tricolor-based MCL luminophore by controlling self-assembly in liquid crystals.¹⁴ While Zou and Tian investigated bis(pyridylvinyl)anthracene (BP2VA) based systems for pressure-dependent mechanochromic luminescence,¹⁸ Saito and Yamaguchi exemplified the recognizable change in the luminochromic behavior of tetrathiazolylthiophene through anisotropic grinding and isotropic compression.¹⁶ Uekusa and Ito synthesized a mechanochromic luminescent system that exhibited fluorescent behavior under the crystalline phase transition.¹⁷

Amalgamating the concepts of MCL and TADF (or, RTP) could potentially aid in the discovery of new functional organic materials.¹⁹ Note that, Zhang, Zou and Ma already explored MCL phenomena in a D-A system by examining the dihedral angle twist between the functionalities, a particular structural aspect of D-A system, which is often associated with the photophysical properties. In this context, particularly relevant is a recent study by Okazaki *et al.* who reported an MCL molecular system (D-A-D triad) that shows mechanochromic luminescence based on its conformations.²⁰⁻²³ They synthesized a system, which shows four conformational varieties based on the relative arrangement among the two donor units comprising of 10-phenothiazine (PTZ) moieties and an acceptor motif dibenzo[*a, j*]phenazine (DBPHZ). Out of four conformations, two are *quasi axial-quasi axial* (AA) with *syn.* and *anti*-variants and one each, *quasi axial-quasi equatorial* (AE), and *quasi equatorial-quasi equatorial* (EE), respectively. While AA was reported to exhibit phosphorescent behavior, AE

manifested the characteristics of both phosphorescence and TADF. Finally, *EE* was predominantly TADF and reported to have the best efficiency among all conformers. Intrigued by these unique MCL features in D-A systems, here we theoretically investigate the conformation-controlled photophysical behaviour of the PTZ and DBPHZ D-A-D triad. Through long-range corrected (time-dependent) density functional theory computations, we evaluate the impact of conformational changes on the luminescence properties of the triad based on ground-state geometries, nature of the excited states and factors controlling the ISC/RISC rates in the conformers. Our findings rationalize the experimental observations and offer design strategies to boost TADF efficiency through structural modifications of the triad.

3.2 Computational details

Ground state(S_0) geometries of the three conformers were optimized using B3LYP exchange-correlation (xc) functional in conjunction with 6-31+g(d,p) basis set.²⁴⁻²⁶ Excited-state geometries were optimized using long-range-corrected hybrid CAM-B3LYP xc functional.²⁷ S_1 states of the three conformers were optimized at the TDDFT level within the Tamm-Dancoff approximation²⁸ and the corresponding T_1 states were optimized via the unrestricted SCF method. Frequency calculations of the ground state and excited states were performed to verify the absence of any unstable modes. For a superior comprehension of excited-state properties, it is essential to get the specific idea of excitation and the excitation energies, since those elements control the general ISC or rISC rates. The traditional TDDFT either overestimates or underestimates the nature of charge transfer in electronic excitations based on the Hartree-Fock percentage of the exchange-correlation functional. Subsequently, it likewise either belittles or overestimates the excitation energies. Recent investigations have shown that precise prediction of both excitation energy and the nature of excitations can be done using the concurrent utilization of gap-tuned long-range corrected functional with Tamm-Dancoff approximation.²⁹⁻³¹ Thus, LC- ω^* PBE functional was employed to calculate the excitation energies. It splits the Coulomb operator into a short-range (SR) and long-range (LR) terms as shown in equation 3.1^{32, 33}

$$\frac{1}{r_{12}} = \frac{1 - [\alpha + \beta \operatorname{erf}(\omega r_{12})]}{r_{12}} + \frac{\alpha + \beta \operatorname{erf}(\omega r_{12})}{r_{12}} \quad (3.1)$$

Thus, it imposes an asymptotic behavior to the exchange potential and maintains a

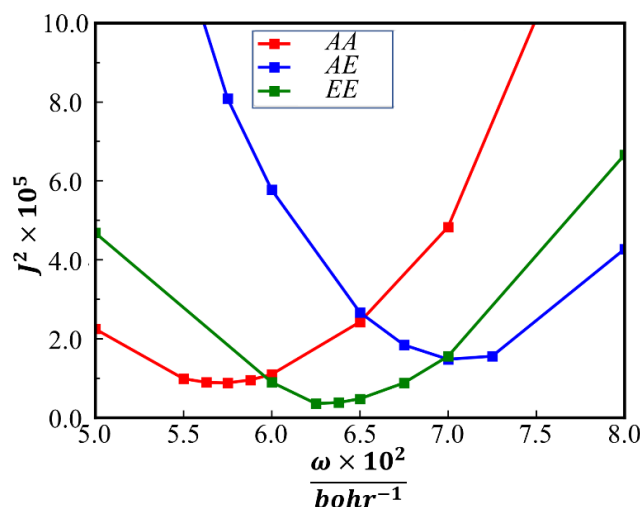


Figure 3.2: Plot of J^2 vs ω for all three conformers using LC- ω *PBE functional in conjunction with 6-31+g(d,p) basis set.

strategic exclusion from the consideration of 100% Hartree-Fock exchange. The error function erf easily interfaces the LR and SR part of the operator with the help of the empirically determinable c term. Here, r_{12} is the inter-electronic distance, α and β are constants. The optimal c values were determined by minimizing J^2 , which is defined by equation 3.2,

$$J^2 = \sum_{i=0}^{i=1} [\epsilon_H(N+i) + IP(N+i)]^2 \quad (3.2)$$

where, ϵ_H and IP are the HOMO energy and ionization potential of the $(N+i)^{th}$ electronic system, respectively. Plot of J^2 vs ω is given in Figure 3.2.

Natural transition orbital (NTO) analysis was performed to understand the nature of the excitation in the three conformers.³⁴ The rotational barrier for the transformation from *AA* to *AE* and *AE* to *EE* conformers were evaluated by scanning the C(donor) – N(donor) – C(acceptor) – C(acceptor) torsion angle between one donor and one acceptor. The rotation profiles were obtained by doing a CNCC dihedral angle constrained optimization of the geometries, which were obtained by changing the dihedral angle at every five-degree interval.³⁵ All the calculations were carried out using the polarizable continuum model (PCM) with an effective dielectric constant of the toluene ($\epsilon=2.34$).³⁶ All geometry optimization and TDDFT computations were

performed using Gaussian 16 Revision A.03 code.³⁷ A Quantitative evaluation of the amount of local excitation or charge transfer of the excited state wave functions was performed using the Multiwfn package.³⁸ The SOC matrix elements were calculated using ADF 2017 package.³⁹ ZORA Hamiltonian was used to consider the relativistic effects, which is zeroth-order regular approximation to the Dirac equation.⁴⁰ Here, the kinetic energy operator captures both the relativistic and spin-orbit coupling effects and the potential is the regular Kohn-Sham potential.

$$\widehat{T}^{ZORA} = \widehat{T}^{SR} + \widehat{T}^{SO} \quad (3.3)$$

$$\boldsymbol{\sigma} \cdot \mathbf{p} \frac{c^2}{2c^2 - V^{KS}} \boldsymbol{\sigma} \cdot \mathbf{p} = \boldsymbol{\sigma} \frac{c^2}{2c^2 - V^{KS}} \boldsymbol{\sigma} + \frac{c^2}{(2c^2 - V^{KS})^2} \boldsymbol{\sigma} \cdot (\nabla V^{KS} \times \mathbf{p}) \quad (3.4)$$

Slater type all-electron TZP basis set was used for all atoms. Also, COSMO continuum-solvation model with the dielectric constant of toluene was used to capture the effect of solvent.⁴¹

3.3 Results and Discussions

3.3.1 Ground state geometry and frontier molecular orbital analysis

We begin by examining the structural differences, relative stabilities and FMOs characteristics of the three conformers in the PTZ-DBPHZ triad. Their geometry-optimized structures are shown in Figure 3.1. Table 3.1 lists some relevant structural parameters including bond lengths ($C_{21} - N_6$ and $C_{12} - N_5$) and the dihedral angles ($C_{50} - N_6 - C_{21} - C_{22}$ and $C_{27} - N_5 - C_{12} - C_{11}$ denoted as ψ and θ , respectively) between the donor and the acceptor units along with the HOMO-LUMO gap (ΔE_{HL}) for the three conformers.

The relative stability ordering among the three conformers is $AA < AE < EE$ with EE being slightly preferred over the others. Figure 3.3 illustrates the potential energy profiles connecting the AA to AE and EE to AE as a function of ψ and θ , respectively. While the transition state for the first PTZ rotation leading to AE conformer is 12.1

kcal/mol above *AA*, the TS for the second PTZ rotation lies 18.9 kcal/mol higher than *AE*. The moderate activation barriers indicate that all the three conformers are readily convertible to one another under ambient conditions.

Table 3.1: Selected bond lengths (Å) and dihedral angles (°) at the ground state optimized geometry (S_0) of the conformers of the PTZ-DBPHZ D-A-D triad computed at the B3LYP/6-31+g(d,p) level

	<i>AA</i>	<i>AE</i>	<i>EE</i>
$C_{21} - N_6$ (Å)	1.41	1.44	1.44
$C_{12} - N_5$ (Å)	1.41	1.41	1.44
Ψ (°)	-10.77	99.37	99.37
Φ (°)	10.77	10.77	-99.37
ΔE_{HL} (eV)	3.23	2.75	2.56

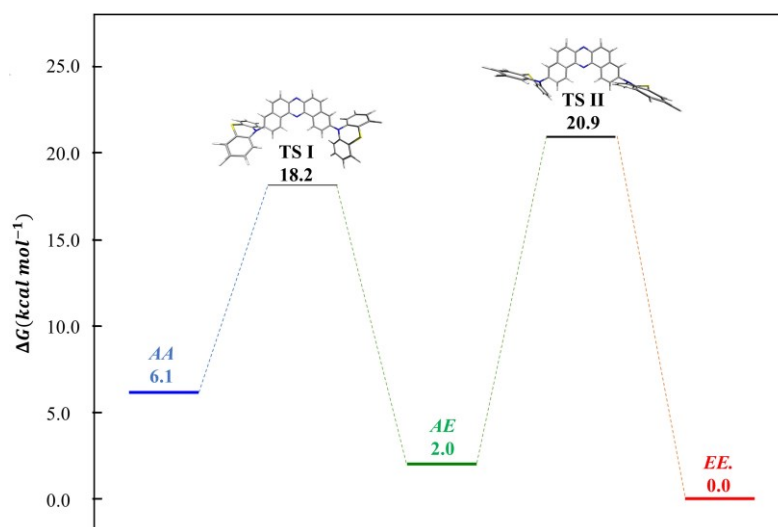


Figure 3.3: Free energy profile for the interconversion between conformers of PTZ-DBPHZ D-A-D triad. All energy values are in kcal/mol

Furthermore, the FMO analysis (Figure 3.4) reveals that the HOMO of *AA* is distributed over the entire triad while the LUMO concentrates on the DBPHZ moiety. The *ax.* to *eq.* rotation of the PTZ moiety induces a change in the FMO characteristics by spatially separating the HOMO over the donor (one PTZ for *AE* and both PTZ for

EE) units and the LUMO over the acceptor unit. These changes in FMO distribution bring a clear distinction in the excitonic character of the electronic transitions compared to *AA*. The ΔE_{HL} ordering is found to be $EE < AE < AA$. In general, the improved TADF efficiency is often associated with a twisted donor and acceptor unit

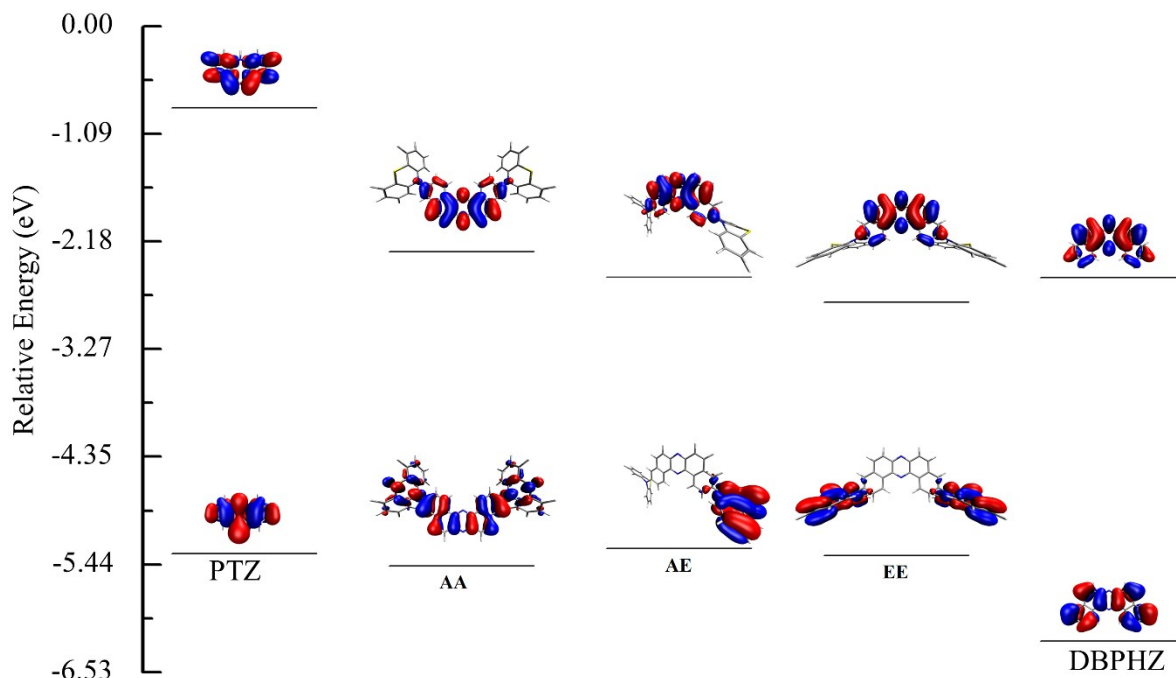


Figure 3.4: HOMO-LUMO of three conformers, PTZ, DBPHZ and their relative energy

leading to minimal overlap between HOMO and LUMO and interestingly, both *AE* and *EE* conformers pertain to this criterion.

3.3.2 Excitation energies and Natural Transition Orbitals (NTO)

Table 3.2: Vertical excitation energies and oscillator strengths (osc. str.) for the three conformers calculated at LC- ω *PBE/6-31+g(d,p) level of theory

State	<i>AA</i>			<i>AE</i>			<i>EE</i>		
	Energy (eV)		osc. Str. (f)	energy (eV)		osc. Str. (f)	energy (eV)		osc. Str. (f)
S1	2.37	524	0.591	1.93	641	0	1.62	767	0
S2	2.48	500	0.0102	2.36	524	0.3082	1.62	767	0
S3	2.87	423	0.0018	2.51	493	0.0002	2.29	542	0
S4	3	414	0.0011	2.84	435	0.0026	2.29	542	0.0002
S5	3.01	412	0.0062	2.95	420	0.0198	2.66	467	0.0022

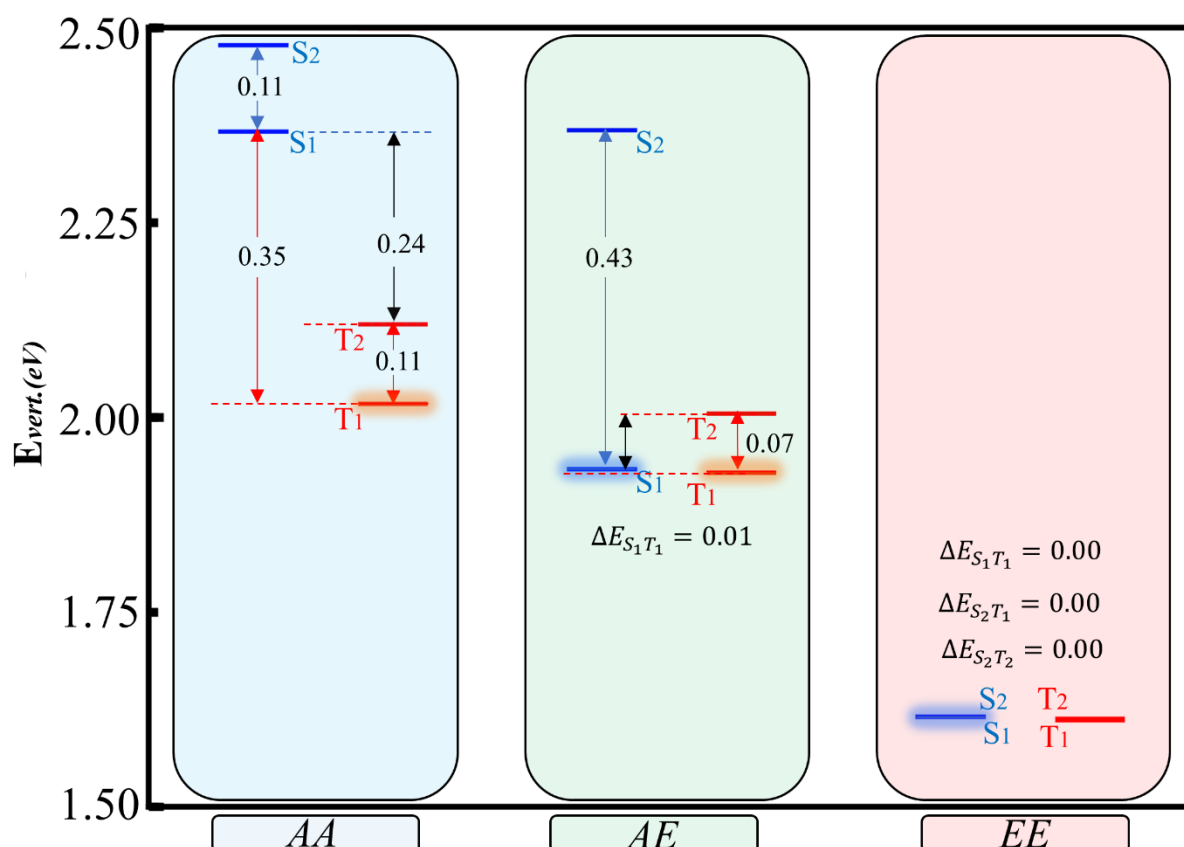


Figure 3.5: Vertical excitation energies for the three conformers calculated at LC- ω^* PBE/6-31+g(d,p) level of theory

The molecular D-A-D triad consists of 2 equivalent donor groups but their positional non-equivalence in the conformers causes an impact on the excitation energies and the nature of the excitation, which in turn is manifested in the luminescence behavior. Figure 3.5 illustrates the energies of low-lying singlet and triplet excited states of the three conformers. The experimentally observed red shift between *AE* and *EE* conformers are well reproduced in our TDDFT results (see Figure 3.5).

The computed excitation energies along with the corresponding oscillator strength values are reported in Table 3.2. We find that S_1 state of *AA* has significant oscillator strength as opposed to negligible oscillator strength in *AE* and *EE*. While *AE* exhibit high oscillator strength for S_2 , S_5 is the brightest state for *EE*.

Examining the triplet manifold, we found that in *AA*, two lowest-lying triplet states (T_1 and T_2) fall much below S_1 , leading to large ΔE_{ST} ($\Delta E_{S_1T_1} = 0.35$ eV and $\Delta E_{S_1T_2} = 0.24$ eV). Such energy orderings will presumably facilitate the ISC (from S_1 to both T_1

and T₂) and hinder rISC. The effect of a PTZ *ax.* to *eq.* rotation is clearly visible in the excited state energy ordering as $\Delta E_{S_1T_1}$ in *AE* drops down to 0.01 eV with T₂ lying 0.07 eV above S₁. Finally, in *EE*, all four energy levels, S₁, S₂, T₁ and T₂ become iso-energetic and hence ΔE_{ST} is practically zero. Based on the ΔE_{ST} values, rISC is anticipated to be relatively favored in *AE* and *EE*, compared to *AA*. We did a quantitative analysis of LE and CT characters to explain the energy order.

The nature of these excited states is further investigated by visualizing the relevant NTOs (see Figure 4) and estimating their excitonic character (local vs. CT, see Table 3.3). Both *AA* and *EE* are symmetric (point group *C_s* and *C_{2u}* respectively) in their respective ground state geometry. As a result, the distribution of NTOs is also very symmetric. Low lying excited-state transitions in *AA* show hybrid LE in nature which is evident from the higher percentage of estimated LE characters (56, 69.8, 71.6 % for S₁, T₁, T₂ respectively). This is presumably due to the delocalized π -conjugation extending over the entire length of the molecule. T₁ being LE in nature helps in phosphorescence (LE characteristics lead to high oscillator strength). In *AE*, S₁ and T₁ have significant CT (89.8 and 89.6 %) characters. As illustrated in Figure 3.6, the separated electron and hole are confined in the acceptor and the equatorial (nearly perpendicular) donor moieties, respectively. The higher CT characteristics of S₁ explains the lower oscillator strength value. T₁ being CT in nature adds up for reduced phosphorescence efficiency along with spin-forbidden restriction (since S₁ is also CT). Interestingly, extended conjugation between the acceptor and the axial (nearly planar) donor groups impart predominant LE character to T₂ (69 % LE). Note that, this can help the rISC channel through spin-vibronic coupling involving T₁ and T₂ (in a second-order perturbative way) as suggested by Gibson *et al.*⁴²

Table 3.3: CT and LE percentage for the low-lying excited states for all three conformers

	<i>AA</i>		<i>AE</i>		<i>EE</i>	
	CT	LE	CT	LE	CT	LE
S ₁	44.0	56.0	89.8	10.2	90.0	10.0
T ₁	30.2	69.8	89.6	10.4	89.9	10.1
T ₂	28.4	71.6	31	69.0	89.8	10.2
S ₂	--	--	--	--	89.9	10.1

The excitonic nature of S_1 , S_2 , T_1 and T_2 is practically the same in the EE conformer with the hole and electron occupying the donor and acceptor moiety, respectively. All excitations correspond to around 90 % CT character and thus require less energy. The involvement of four closely lying states will also help in exciton transfer through rISC along with decreased energy gap if we consider second-order perturbation. Because of such a small energy gap between the low-lying excited states, the vibronic coupling can efficiently populate the excitons in T_2 , which then transfers it to S_1 state. Clearly a low-lying S_1 (due to significant CT character) leads to a much-reduced singlet-triplet gap in AE and EE , which indicates a higher possibility of rISC.

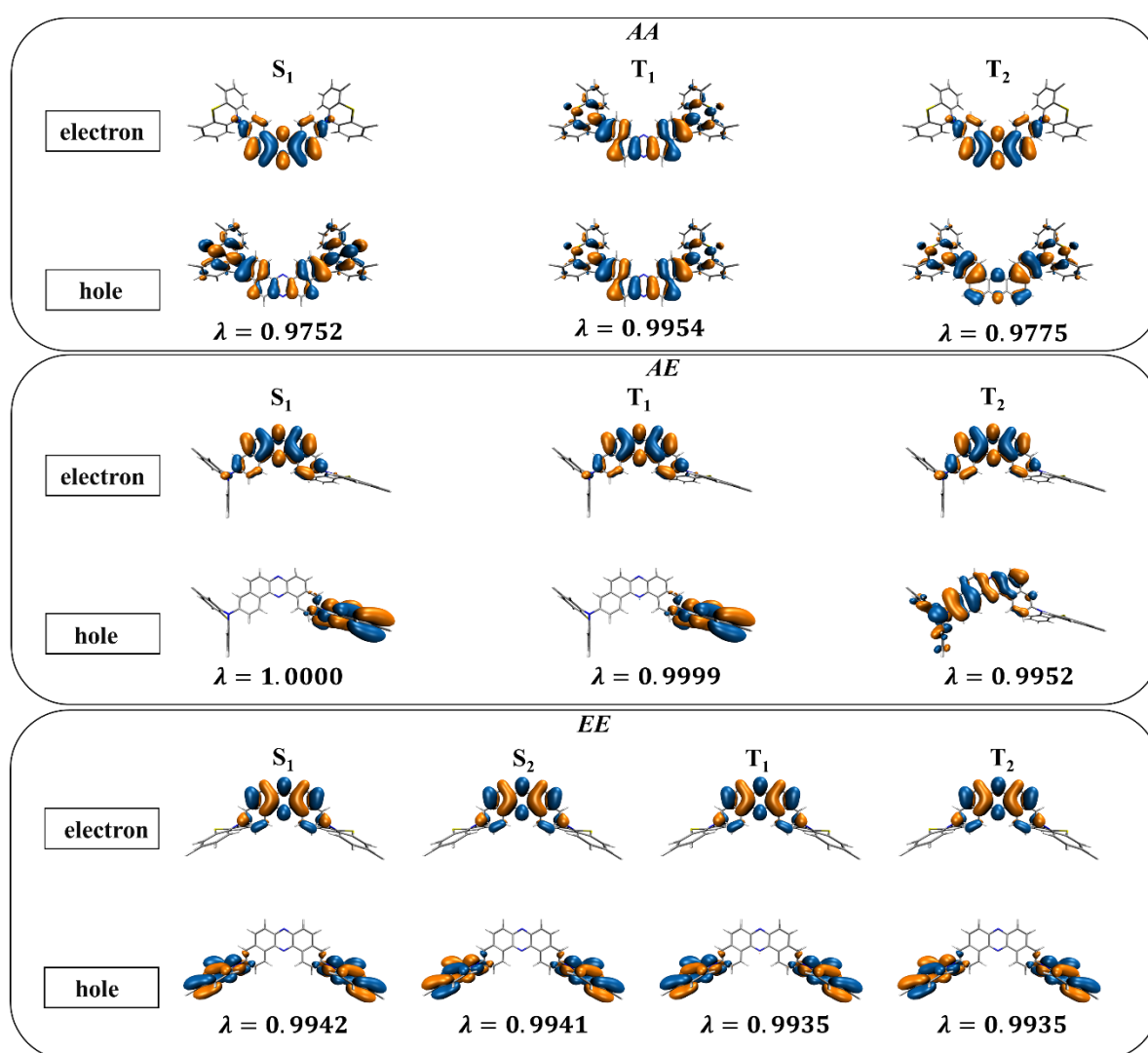


Figure 3.6: Natural Transition Orbitals of the three conformers for low lying triplet and singlet excited states, λ is the highest coefficient of SVD

3.3.3 Spin-Orbit Coupling and Reorganization energy

In Table 3.4, we have listed the calculated spin-orbit coupling elements for all the three conformers of the D-A-D triad. These values are anticipated to be small since the triad is devoid of any heavy atom. However, the presence of hetero atom induces a change in the orbital type during electronic transition. Thus, through a change in orbital type during transition, the spin-orbit coupling can be enhanced and change by the order of 1-2 in these values can significantly change the rISC. An examination of the spin-orbit coupling operator H_{SO} can qualitatively explain the obtained results.

We recall that under central-field approximation, spin-orbit operator \widehat{H}_{SO} becomes,

$$\widehat{H}_{SO} = \left\langle R(r) \left| \frac{1}{2m^2c^2} \frac{1}{r} \frac{dV(r)}{dr} \right| R(r) \right\rangle [l_{iz}s_{iz} + l_{i+}s_{i-} + l_{i-}s_{i+}] \quad 3.5$$

where $V(r)$ represents the distance-dependent function between nucleus and the electron. $l_{i+/-}$ and $s_{i+/-}$ denotes the step up or step-down operators for orbital and spin angular momentum for i -th electron, respectively. l_{is} and s_{is} represent the z component of the orbital and spin angular momentum. Thus, an increment/decrement of the spin quantum number is simultaneously coupled with a decrement/increment of the orbital angular momentum. Since the π electron conjugation in the three conformers comprises of p_{+1} , p_0 and p_{-1} orbitals, a spin-flip would result in a change in the p orbitals. SOCME will be negligible unless there is a difference in hole and electron distribution (different CT/LE characters between S_1/T_n states) during the change in spin multiplicity.

The estimated spin-orbit coupling elements values follow the same trend when computed with the optimized geometries of either the T_1 or the S_1 states and we will refer to former values during the discussion. In *AA*, all the three states, namely, S_1 , T_1 and T_2 , exhibit hybrid LE character as can be seen from Table 3.3. Thus, SOCME calculated between these states turned out to be quite small, 0.07 cm^{-1} and 0.06 cm^{-1} between states S_1 , T_1 and S_1 , T_2 , respectively. Moreover, in *AE*, SOCME between the S_1 and T_1 states is also small (0.02 cm^{-1}), due to CT character of the associated states. However, interestingly, the SOCME increases by almost ten times to 0.22 cm^{-1} for S_1 e T_2 owing to the LE character of T_2 state.

Table 3.4: Spin-Orbit Coupling Elements (cm^{-1}) $\langle S_1|H|T_n\rangle(\langle S_2|H|T_n\rangle)$ calculated using LCY- ω^* PBE functional with TZP basis set at the T_1 and S_1 optimized structure

	T_1 geom.			S_1 geom.		
	AA	AE	EE	AA	AE	EE
T_1	0.07	0.02	0.00 (0.00)	0.07	0.56	0.01 (0.00)
T_2	0.06	0.22	0.02 (0.00)	0.03	0.01	0.00 (0.00)
T_3	0.13	0.37	0.01 (0.13)	0.16	0.45	0.19 (0.50)
T_4	0.36	0.8	0.30 (0.30)	0.37	0.46	0.67 (0.00)
T_5	0.19	0.36	0.00 (0.00)	0.17	0.11	0.61 (0.00)

Thus, the rISC would mostly involve T_2 state along with S_1 and T_1 states through mainly the spin-vibronic coupling term. Note that, for the S_1 optimized geometry, this trend has been reversed. In fact, this can also explain the phosphorescence, since it opens an ISC channel from S_1 to T_1 state. In EE , the low-lying excited states, namely, S_1 , S_2 , T_1 , T_2 are all predominantly CT in nature. As a result, the estimated SOCME values involving these states turn out to be quite small. For example, SOCME between S_1 and T_2 is calculated to be 0.02 cm^{-1} . At the S_1 state optimized geometry, these values are near to zero and follows the same trend.

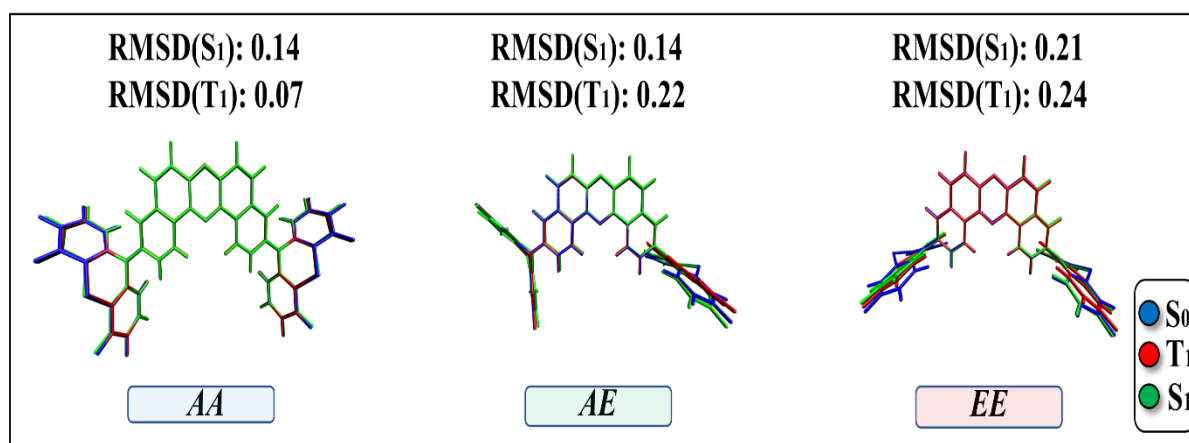


Figure 3.7: Relative RMSD of the structures with respect to their respective ground state structures

Next, we focus on the reorganization energy involved in the T_1 to S_0 transition for the three conformers since it plays a major role in determining the overall phosphorescence and TADF efficiency. Figure 3.7 illustrates the Root-Mean-Square-

Deviation (RMSD) of atomic positions of the excited-state geometries with respect to ground state geometry for each conformer, which qualitatively commensurate with the reorganization energy (λ). In general, a lower RMSD for T_1 (and lower reorganization energy) helps to diminish decay through non-radiative channels and thereby, facilitates phosphorescence efficiency. Among the three conformers, *AA* (0.07) has the lowest RMSD values at the T_1 geometry indicating the higher possibility of phosphorescence emission compared to *AE* (0.22) and *EE* (0.24). In the absence of any other channel, such high RMSD would imply non-radiative decay from T_1 for *AE* and *EE* but low ΔE_{ST} provides an alternative pathway to convert the triplet excitons into singlet ones. In any case, this explains the experimentally observed lower phosphorescence efficiency or almost no phosphorescence in *AE* and *EE* conformers, respectively.

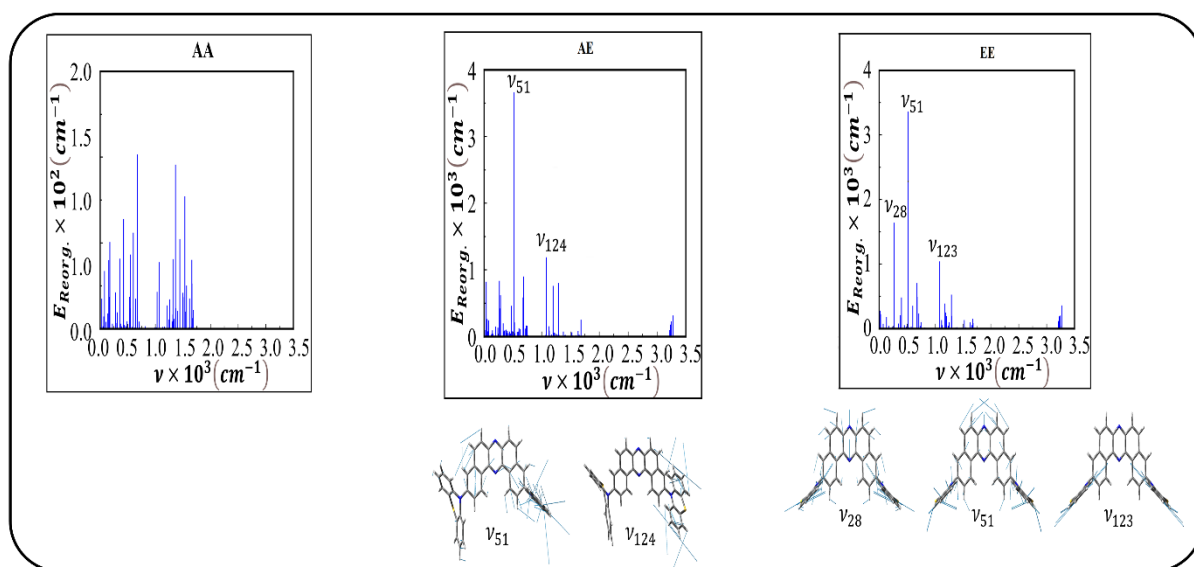


Figure 3.8: Mode-wise reorganization energy for the T_1 state for all three conformers

To better understand the role of molecular structure on reorganization energy, we computed the mode-wise reorganization energies. Reorganization energy due to intramolecular vibrations is defined as,

$$\lambda_i = \hbar \omega_i S_i \quad 3.6$$

where ω_i and S_i are the frequency and the Huang-Rhys factor, respectively, for the i th vibration.

In fact, the high reorganization energies for the *AE* and *EE* conformers are due to the vibrational modes associated with the equatorial donor groups which are planar at

their respective T_1 optimized geometry (see Figure 3.8). For the *AE* conformer, these modes, ν_{51} and ν_{124} , are involved in the breathing of thiomorpholine residue and aromatic rings, respectively. In case of *EE*, both the ν_{28} and ν_{51} modes are due to the breathing of thiomorpholine residue and ν_{123} mode arises mainly due to the breathing of aromatic rings of PTZ group.

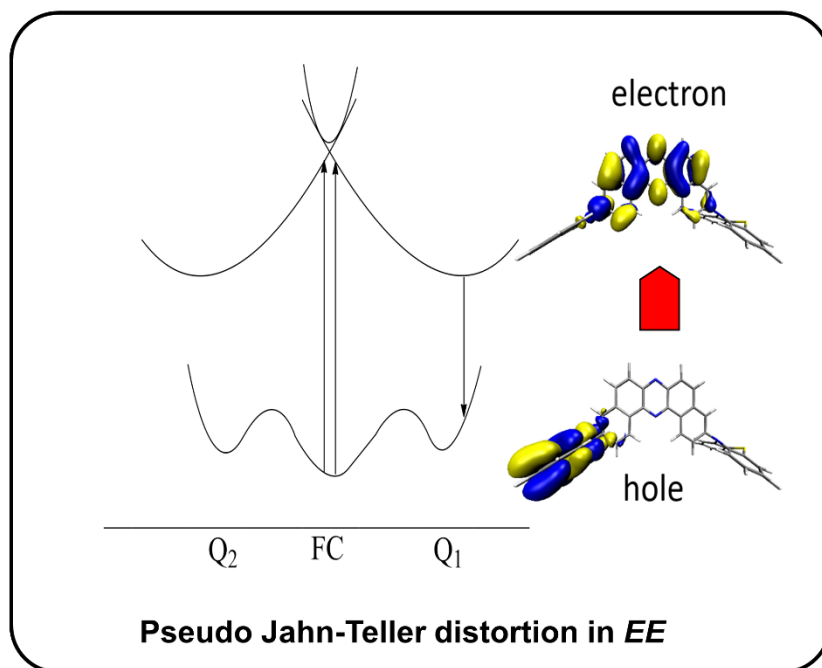


Figure 3.9: Hole and electron picture for the transition from S_1 to S_0 at S_1 optimized geometry.

S_1 optimized geometry of *AE*, which is radiative in nature and shows TADF is very similar to its ground state structure.

This structural organization helps in vertical emission by reducing the reorganization energy. Additional investigation on *EE* conformer shows that one of the PTZ groups in its S_1 optimized geometry is planar (with respect to the ground state geometry) while the other one retains its orientation similar to that in the ground-state structure. Thus, following the initial excitation, the molecular system relaxes to two identical or doubly degenerate (excited) potential energy surfaces, with one planar PTZ group and the other retaining the morphology of the ground state structure. This geometric relaxation induces a change in the orbitals involved in emission. During excitation, hole (absence of electron) is located on both the donor groups while after relaxation, the hole resides on the planar PTZ group (which is in lower energy in the PES) as shown in Figure 3.9. Such breaking of symmetry by the mixing of both ground

state and excited structure by nuclear displacement provides evidence for the pseudo-Jahn-Teller (pJT) effect.⁴³⁻⁴⁵ Because of pJT distortion, there is a conical intersection between S_1 and S_2 . So, any exciton transfer from triplet manifolds to S_2 immediately go to S_1 state and such presence of energetically nearby excited states will increase the spin-vibronic second order perturbation, which in turn boost the overall rISC efficiency.

Table 3.5: Scheme for the characterization of photophysical behavior of each conformers

Features	AA	AE	EE
HOMO-LUMO spatial separation	<i>X</i>	✓	✓
Low ΔE_{ST}	<i>X</i>	✓	✓
SOCME between S_1 and T_1	low	low	Low
Reorganization en. of T_1	low	high	High
Overall photophysical characteristics	RTP	RTP and TADF	TADF

Scheme 1 (Table 3.5) mostly summarizes our computational results. *AA* shows a significant degree of HOMO-LUMO overlap because of its almost planar structural arrangement of D-A units, while in *AE* and *EE*, these orbitals are spatially separated. As a result, the ΔE_{ST} is also small in later conformers due to dominant CT characteristics in S_1 and T_1 transitions. Such excitation nature, in turn, reduces the SOCME between S_1 and T_1 states. Apart from the electronic structure of excited states of the conformers, the role of the geometric factor has also been investigated. The reorganization energy of T_1 state, which also dictates the non-radiative decay process, turns out to be quite small for *AA* conformer, which predominantly shows phosphorescence, while higher reorganization energy for *AE* and *EE* conformers, make their T_1 state prone for non-radiative decay.

The better TADF efficiency of the *EE* conformer over the *AE* conformer can be explained by the rISC rate equation. Based on second-order perturbation theory, rISC rate equation has the following form,

$$k_{rISC} \propto \frac{2\pi}{\hbar} \left| \frac{\langle \Psi_{T_2} | H_{SOC} | \Psi_{S_1} \rangle}{\Delta E_{T_1 T_2}} \right|^2 \quad 3.7$$

If we consider a similar vibronic coupling between T_1 and T_2 for both the TADF active conformers, qualitatively *EE* shows a higher k_{rISC} rather than *AE* conformer because of lower $\Delta E_{T_1 T_2}$, although it has smaller spin-orbit coupling strength (see Table 3.6).

Table 3.6: qualitative comparison of rISC rates

Conformer	$E_{SOC}(\text{cm}^{-1})$	$E_{T_1 T_2}(\text{eV})$	$k_{rISC} \propto \left \frac{E_{SOC}}{\Delta E_{T_1 T_2}} \right ^2$
AE	0.22	0.07	9.88
EE	0.02	0.0012	277.78

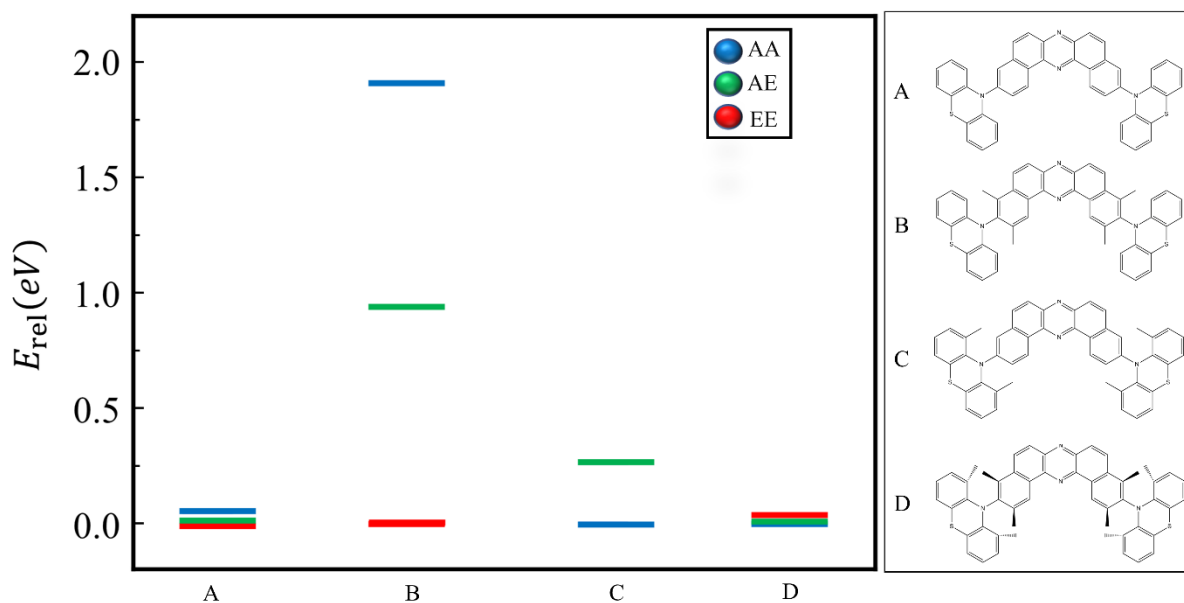


Figure 3.10: Relative energies (eV) of both substituted and unsubstituted conformers

3.3.4 Creating population difference by functionalization

Being readily interconvertible, the population of the three conformers of PTZ-DBPHZ D-A-D triad are expected to have similar proportions under ambient conditions. Due to lower or no TADF efficiency of *AE* and *AA*, respectively, the overall TADF of the triad would be much lower. One strategy to overcome this problem involves modifying the excitonic nature or reducing the ΔE_{ST} gap by inducing charge transfer characteristics in the less efficient *AA* and *AE* conformers, such that they exhibit appreciable TADF. This could be achieved with skeletal modification or appropriate functionalization on the chromophore motifs but comes with the risk of instigating radical changes in the excitonic nature or even, in excited state geometry. A more promising yet, simpler strategy to boost the overall TADF efficiency is to preferential stabilization of the *EE* conformers over the other through functionalization that does not impose major structural modifications (similar D-A dihedral angles preserves the excitonic nature). To examine this possibility, we functionalize individually and concurrently both PTZ and DBPHZ moieties with Me groups (optimized structures are shown in Figure 3.11). Figure 3.10 depicts the chemical structure of the resulting three functionalized triads along with the relative stabilities of their three conformers. Introducing Me groups simultaneously in both the D and A skeletons do not create a population difference and all three conformers have comparable stabilities. When placed on the donor moiety *EE* gets highly destabilized but substitution on acceptor moiety not only helps to retain the excitation

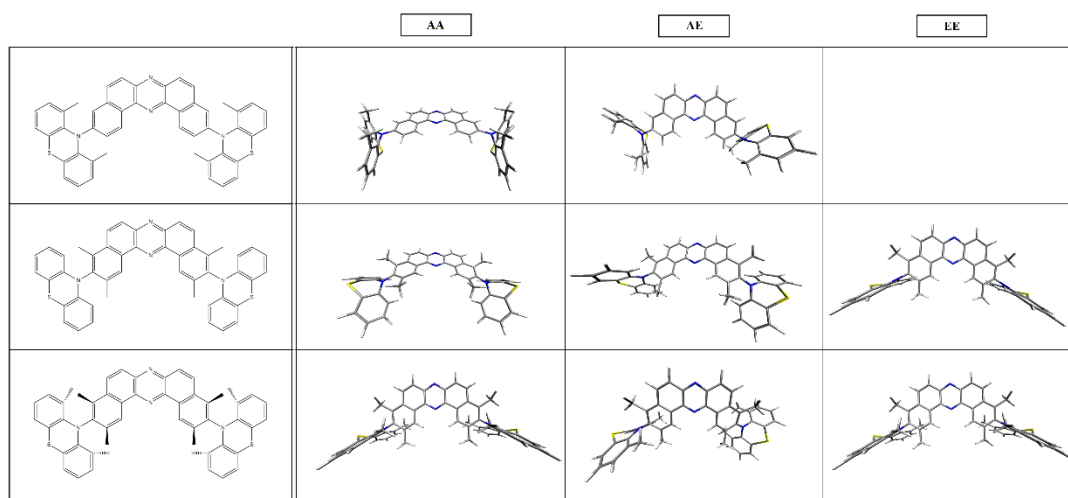


Figure 3.11: Optimized structures of the Me substituted conformers.

nature but also creates a consequential relative ground-state energy difference making the most TADF efficient *EE* conformer most stable. Thus, substitution strategy can be very successful without any major trading of excitation nature.

3.4 Conclusions

In this chapter, we have theoretically investigated the photophysical properties of a D-A-D triad consisting of PTZ as donor and DBPHZ as the acceptor unit. Among the three possible conformers, *EE* is the most stable one followed by *AE* and *AA*. The rotational barriers corresponding to their interconversion are estimated within 12-19 kcal/mol, indicating they are readily interconvertible under ambient conditions. FMO analyses reveal a substantial overlap between HOMO and LUMO for the *AA* conformer while the involvement of the *eq.* group tends to reduce this overlap resulting in a spatial separation between the frontier orbitals. This result further can be envisaged by the excitation characteristics of low-lying singlet and triplet excited states of the three conformers. In *AA*, S_1 , T_1 and T_2 are LE. In *AE*, S_1 and T_1 have predominant CT characteristics and energetically higher T_2 shows hybrid LE nature. In *EE*, T_1 , T_2 , S_1 , S_2 are predominantly CT in nature since all the transitions are spatially separated. Due to such high CT nature, excitations in *AE* and *EE* conformer require low excitation energy in comparison with corresponding states of *AA* conformer. The High singlet-triplet gap makes ISC dominant in *AA*. In *AE*, the singlet-triplet gap is quite low, which helps in RISC. Apart from the electronic factors, the role of the geometry of the relevant excited states is also examined. Lower reorganization energy for T_1 state reduces the amount of non-radiative decay from T_1 boosting the phosphorescence efficiency. In *AE* and *EE*, higher reorganization energy of T_1 state either reduces or completely suppresses the phosphorescence route. *EE* conformer, which shows TADF, features pseudo Jahn-Teller distortion by the mixing of ground state and excited state and degenerate singlet excited states. This helps to boost the overall rISC. Finally, we propose a strategy through functional modification of the triad for regulating the population difference among the conformers without any major alteration of the excitonic nature and thereby, maximizing the TADF efficiency.

Bibliography

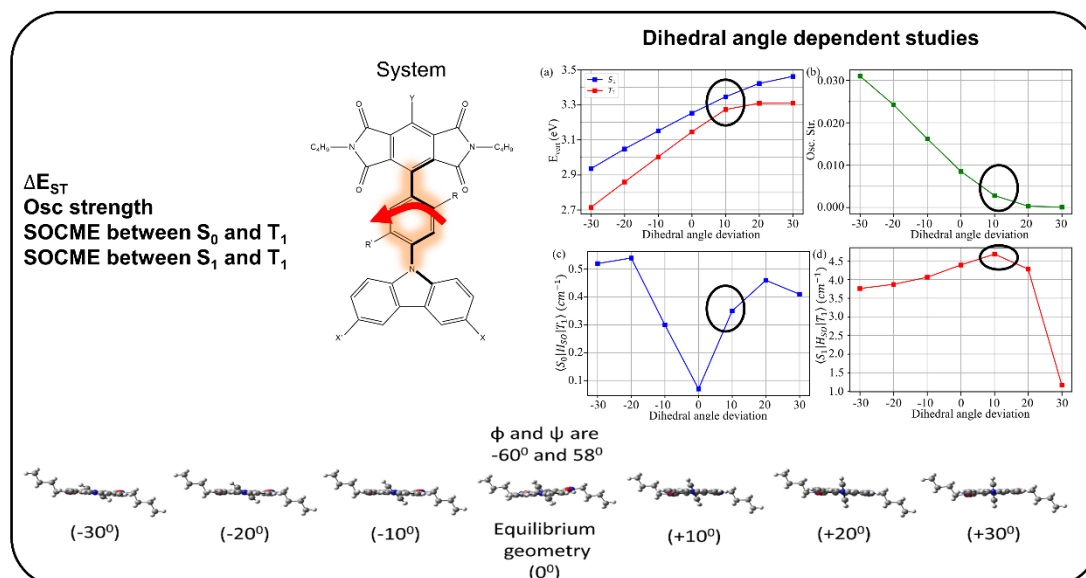
- [1] M. A. Baldo, M. E. Thompson, S. R. Forrest *Nature*. **2000**, *403*, 750-753.
- [2] K. Mullen, U. Scherf, Organic light emitting devices: synthesis, properties and applications, **2006**.
- [3] Z. Yang, Z. Mao, Z. Xie, Y. Zhang, S. Liu, J. Zhao, J. Xu, Z. Chi, M. P. Aldred *Chemical Society Reviews*. **2017**, *46*, 915-1016.
- [4] H. Uoyama, K. Goushi, K. Shizu, H. Nomura, C. Adachi *Nature*. **2012**, *492*, 234-238.
- [5] H. Kaji, H. Suzuki, T. Fukushima, K. Shizu, K. Suzuki, S. Kubo, T. Komino, H. Oiwa, F. Suzuki, A. Wakamiya, Y. Murata, C. Adachi *Nature Communications*. **2015**, *6*, 8476.
- [6] P. Rajamalli, N. Senthilkumar, P. Gandeepan, P.-Y. Huang, M.-J. Huang, C.-Z. Ren-Wu, C.-Y. Yang, M.-J. Chiu, L.-K. Chu, H.-W. Lin, C.-H. Cheng *Journal of the American Chemical Society*. **2016**, *138*, 628-634.
- [7] Z. Yin, M. Gu, H. Ma, X. Jiang, J. Zhi, Y. Wang, H. Yang, W. Zhu, Z. J. A. C. An. **2021**, *133*, 2086-2091.
- [8] T. Itoh *Chemical Reviews*. **2012**, *112*, 4541-4568.
- [9] G. Baryshnikov, B. Minaev, H. Ågren *Chemical Reviews*. **2017**, *117*, 6500-6537.
- [10] Z. Ma, M. Teng, Z. Wang, S. Yang, X. Jia *Angewandte Chemie International Edition*. **2013**, *52*, 12268-12272.
- [11] H.-J. Kim, D. R. Whang, J. Gierschner, C. H. Lee, S. Y. Park *Angewandte Chemie International Edition*. **2015**, *54*, 4330-4333.
- [12] Y. Matsunaga, J.-S. Yang *Angewandte Chemie International Edition*. **2015**, *54*, 7985-7989.
- [13] S. K. Park, I. Cho, J. Gierschner, J. H. Kim, J. H. Kim, J. E. Kwon, O. K. Kwon, D. R. Whang, J.-H. Park, B.-K. An, S. Y. Park *Angewandte Chemie International Edition*. **2016**, *55*, 203-207.
- [14] Y. Sagara, T. J. A. C. Kato. **2011**, *123*, 9294-9298.
- [15] Y. Q. Dong, J. W. Y. Lam, B. Z. Tang *The Journal of Physical Chemistry Letters*. **2015**, *6*, 3429-3436.
- [16] K. Nagura, S. Saito, H. Yusa, H. Yamawaki, H. Fujihisa, H. Sato, Y. Shimoikeda, S. Yamaguchi *Journal of the American Chemical Society*. **2013**, *135*, 10322-10325.

- [17] S. Yagai, S. Okamura, Y. Nakano, M. Yamauchi, K. Kishikawa, T. Karatsu, A. Kitamura, A. Ueno, D. Kuzuhara, H. Yamada, T. Seki, H. Ito *Nature Communications*. **2014**, *5*, 4013.
- [18] Y. Dong, B. Xu, J. Zhang, X. Tan, L. Wang, J. Chen, H. Lv, S. Wen, B. Li, L. Ye, B. Zou, W. Tian *Angewandte Chemie International Edition*. **2012**, *51*, 10782-10785.
- [19] P. Data, Y. Takeda *Chemistry – An Asian Journal*. **2019**, *14*, 1613-1636.
- [20] Y. Takeda, T. Kaihara, M. Okazaki, H. Higginbotham, P. Data, N. Tohnai, S. Minakata *Chemical Communications*. **2018**, *54*, 6847-6850.
- [21] Y. Takeda, H. Mizuno, Y. Okada, M. Okazaki, S. Minakata, T. Penfold, G. Fukuhara *ChemPhotoChem*. **2019**, *3*, 1200-1200.
- [22] P. Data, M. Okazaki, S. Minakata, Y. Takeda *Journal of Materials Chemistry C*. **2019**, *7*, 6616-6621.
- [23] M. Okazaki, Y. Takeda, P. Data, P. Pander, H. Higginbotham, A. P. Monkman, S. Minakata *Chemical Science*. **2017**, *8*, 2677-2686.
- [24] A. D. Becke *The Journal of Chemical Physics*. **1992**, *96*, 2155-2160.
- [25] C. Lee, W. Yang, R. G. Parr *Physical Review B*. **1988**, *37*, 785-789.
- [26] B. Miehlich, A. Savin, H. Stoll, H. Preuss *Chemical Physics Letters*. **1989**, *157*, 200-206.
- [27] T. Yanai, D. P. Tew, N. C. Handy *Chemical Physics Letters*. **2004**, *393*, 51-57.
- [28] S. Hirata, M. Head-Gordon *Chemical Physics Letters*. **1999**, *314*, 291-299.
- [29] H. Sun, C. Zhong, J.-L. Brédas *Journal of Chemical Theory and Computation*. **2015**, *11*, 3851-3858.
- [30] T. J. Penfold *The Journal of Physical Chemistry C*. **2015**, *119*, 13535-13544.
- [31] P. K. Samanta, D. Kim, V. Coropceanu, J.-L. Brédas *Journal of the American Chemical Society*. **2017**, *139*, 4042-4051.
- [32] L. Kronik, T. Stein, S. Refaely-Abramson, R. Baer *Journal of Chemical Theory and Computation*. **2012**, *8*, 1515-1531.
- [33] A. V. Krukau, O. A. Vydrov, A. F. Izmaylov, G. E. Scuseria *The Journal of Chemical Physics*. **2006**, *125*, 224106.
- [34] R. L. Martin *The Journal of Chemical Physics*. **2003**, *118*, 4775-4777.
- [35] J. S. Ward, R. S. Nobuyasu, M. A. Fox, A. S. Batsanov, J. Santos, F. B. Dias, M. R. Bryce *The Journal of Organic Chemistry*. **2018**, *83*, 14431-14442.
- [36] G. Scalmani, M. J. Frisch *The Journal of Chemical Physics*. **2010**, *132*, 114110.

- [37] M. J. Frisch, G. W. Trucks, H. B. Schlegel, G. E. Scuseria, M. A. Robb, J. R. Cheeseman, G. Scalmani, V. Barone, G. A. Petersson, H. Nakatsuji, X. Li, M. Caricato, A. V. Marenich, J. Bloino, B. G. Janesko, R. Gomperts, B. Mennucci, H. P. Hratchian, J. V. Ortiz, A. F. Izmaylov, J. L. Sonnenberg, Williams, F. Ding, F. Lipparini, F. Egidi, J. Goings, B. Peng, A. Petrone, T. Henderson, D. Ranasinghe, V. G. Zakrzewski, J. Gao, N. Rega, G. Zheng, W. Liang, M. Hada, M. Ehara, K. Toyota, R. Fukuda, J. Hasegawa, M. Ishida, T. Nakajima, Y. Honda, O. Kitao, H. Nakai, T. Vreven, K. Throssell, J. A. Montgomery Jr., J. E. Peralta, F. Ogliaro, M. J. Bearpark, J. J. Heyd, E. N. Brothers, K. N. Kudin, V. N. Staroverov, T. A. Keith, R. Kobayashi, J. Normand, K. Raghavachari, A. P. Rendell, J. C. Burant, S. S. Iyengar, J. Tomasi, M. Cossi, J. M. Millam, M. Klene, C. Adamo, R. Cammi, J. W. Ochterski, R. L. Martin, K. Morokuma, O. Farkas, J. B. Foresman, D. J. Fox in *Gaussian 16 Rev. C.01*, Vol. (Ed. ^Eds.: Editor), City, **2016**.
- [38] T. Lu, F. Chen *Journal of Computational Chemistry*. **2012**, *33*, 580-592.
- [39] G. te Velde, F. M. Bickelhaupt, E. J. Baerends, C. Fonseca Guerra, S. J. A. van Gisbergen, J. G. Snijders, T. Ziegler *Journal of Computational Chemistry*. **2001**, *22*, 931-967.
- [40] E. v. Lenthe, E. J. Baerends, J. G. Snijders *The Journal of Chemical Physics*. **1993**, *99*, 4597-4610.
- [41] C. C. Pye, T. J. T. C. A. Ziegler. **1999**, *101*, 396-408.
- [42] J. Gibson, A. P. Monkman, T. J. Penfold *ChemPhysChem*. **2016**, *17*, 2956.
- [43] A. R. Ilkhani, N. N. Gorinchoy, I. B. J. C. P. Bersuker. **2015**, *460*, 106-110.
- [44] I. B. J. C. R. Bersuker. **2013**, *113*, 1351-1390.
- [45] L. Blancafort, M. J. T. J. o. P. C. A. Solà. **2006**, *110*, 11219-11222.

Chapter 4

4 Tailoring Dual Emissions from Pyromellitic Diimide Derivatives through Substitution: A Theoretical Perspective*



*Work reported in this chapter is based on: Bidhan Chandra Garain, Swapan K Pati, Theo. Chem. Acc. (Revision submitted, 2023).

4.1 Introduction

Triplet exciton harvesting in purely organic chromophores via thermally activated delayed fluorescence (TADF) and ambient room temperature phosphorescence (RTP) gained huge interest for their potential application in bio-imaging, optical sensing, and organic light emitting diodes (OLEDs).¹⁻⁶ While first-generation fluorescence emitters can harvest 25% of the generated excitons, the second-generation (phosphorescent materials) can harvest the other 75% of the triplet excitons adding the total internal quantum efficiency (IQE) to 100%. Similarly, the third-generation light emitters (TADF materials) have also IQE~100. The basic design principle for TADF molecule is to make a perpendicular donor-acceptor (D-A) system to reduce the first excited singlet-triplet (ΔE_{ST}) gap.⁷⁻⁹ While the design principle for an RTP system is to increase the spin-orbit coupling between the different spin-manifolds either via the incorporation of heavy atoms or via the incorporation of lone-pair containing heteroatom to facilitate the orbital change during intersystem crossing (π - π^* to n - π^* or vice versa; El-Sayed Rule).¹⁰⁻¹⁷

Apart from the excited-state electronic structure, the excited-state geometric structure plays a big role in determining the overall efficiency. Higher molecular vibrations lead to rapid quenching of the excited state leading to a lower IQE. So, incorporating rigidity to reduce the effective molecular vibration has been added on top of the existing design principle.

Recently synthesized arylene diimides in this context are great for showing dual RTP and TADF characteristics.¹⁸⁻²⁰ The systems (both naphthalene diimide and pyromellitic diimide) are electron deficient and have efficient n-electron transporting properties. The presence of multiple carbonyl groups and heavy atom substitution helps in increasing the spin-orbit coupling strength for intersystem crossing from singlet to triplet manifold. Apart from having good intersystem crossing quantum yield, rigid π -conjugated backbone helps in reducing the non-radiative transitions leading to highly efficient RTP materials. While proper donor substitution on arylene diimide leads to charge transfer characteristics in the low-lying singlet (S_1) or triplet (T_1) excited states, which makes the systems also effective TADF materials. Thus, arylene diimides can be exploited for their dual RTP and TADF properties increasing the overall efficiency of the molecular architecture.

Recently George *et al.* have synthesized carbazole core substituted PmDI derivative (CzPhPmDI) which shows yellow emissive dual RTP and TADF under ambient conditions leading to excellent quantum efficiency of 60%.²¹ The phenyl spacer in between donor and acceptor avoids the generation of a non-emissive twisted intramolecular charge transfer state (TICT).²²

Previous theoretical calculations on this system were carried out in the crystalline environment with the help of time-dependent density functional theory (TDDFT) to delineate the TADF or RTP phenomena and possibilities of the involvement of higher excited states in the emission.²¹ Recently, Cui *et al.* have studied the CzPhPmDI system in the PMMA matrix with the help of QM/MM calculations. The treatment includes both TDDFT and wave-function-based methods (e.g., MS-CASPT2).²³ They calculated both the radiative and non-radiative transition rates for unraveling the luminescence mechanism. The current literature still lacks the dihedral angle dependence of the phenyl spacer which separates the donor and the acceptor on overall luminescence characteristics and whether certain substitutions on donor, acceptor, or on spacer yield better luminescent materials.

In this chapter, we have studied the effect of heavy atom (Br) substitution on both carbazole and PmDI derivatives on excited state properties and intersystem crossing rates (Figure 4.1). We have also substituted Me groups on spacer and locked the dihedral angle to be nearly 90° to reduce the HOMO-LUMO overlap to lower the ΔE_{ST} . We have found out that Br-substitution on carbazole unit does not increase the ISC or rISC rates in comparison to the unsubstituted CzPhPmDI system. While Br substitution on PmDI group leads to significant improvement of ISC rate, which is important for triplet harvesting process. While Me substitution leads to higher rISC rate which is important for TADF, Me substitution also leads to high structural deviation in excited state in comparison to the ground state which is indicative of generation of twisted intramolecular charge transfer (TICT) state, leading to a red-shifted bright emission due to increased coplanarity in the excited-state geometries. We hope this study will further improve the strategical substitution-based synthesis of PmDI derivatives for efficient dual RTP and TADF emitters.

4.2 Computational Methodology

Optimization of the ground state geometries for all the systems were carried out using B3LYP functional in conjunction with the 6-31+g(d) basis set for C, H, O and N. While for Br, we have used lanl2dz basis set with effective core potential. Excitation energies of CzPhPmDI were calculated using B3LYP, CAM-B3LYP, Mo6, Mo62X, and ω b97xd functional.²⁴⁻²⁹ The relevant structural parameters after optimization are reported in Table 4.1. The values obtained from Mo62X functional corroborates well with the experimental findings. So, further calculations for the excited state geometry and energy were performed using Mo62X functional.

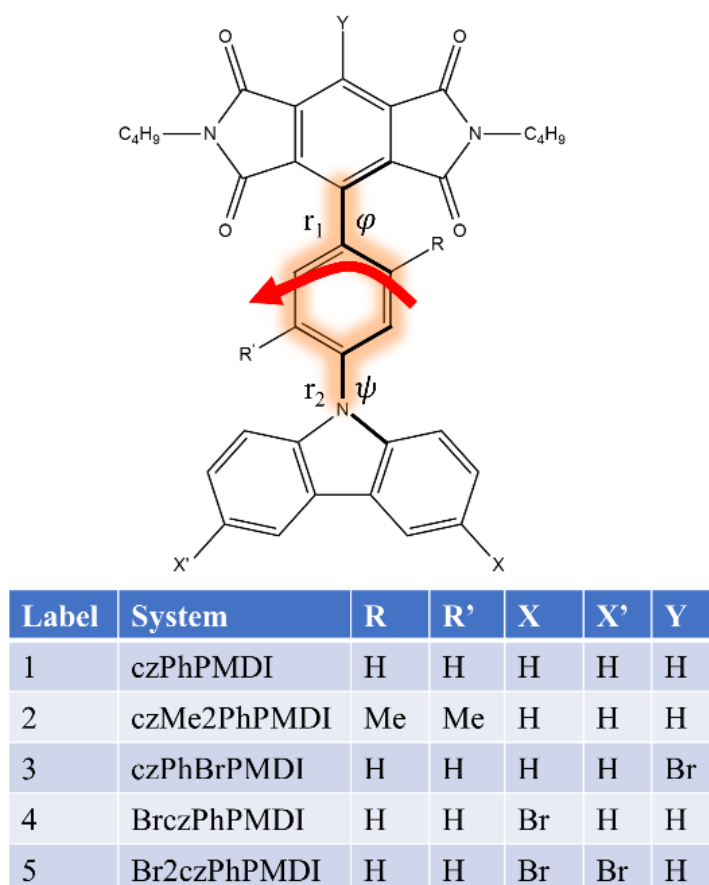


Figure 4.1: CzPhPmDI and its derivatives studied in this work

Vertical excitation energies with oscillator strength are given in the Table 4.2. All the TDDFT calculations were performed in Toluene solvent considering the Polarizable Continuum Model (PCM) to obtain the direct comparison with the experimental results (the keyword “SCRF=solvent=toluene” was used; this indicates the default

SCRF method which is the Polarizable Continuum Model (PCM) using the integral equation formalism (IEFPCM)).³⁰ Additionally, the values computed with the other solvation models have been reported in Table 4.3. For the characterization of the excitation natures, Natural Transition Orbital (NTO) analyses were carried out.³¹ All these calculations were performed using the Gaussian 16 software where the convergence criteria was kept as default.³²

4.2.1 Spin Orbit Coupling (SOC) Matrix Elements

The SOC matrix elements were estimated using the zeroth order regular approximation (ZORA) Hamiltonian.³³⁻³⁵ The SOC operator \hat{H}_{SOC} , within ZORA is defined as,

$$\hat{H}_{SOC} = \frac{c^2}{(c^2 - V_{KS})^2} \boldsymbol{\sigma} \cdot (\nabla V_{KS} \times \mathbf{p}) \quad (4.1)$$

where c , V_{KS} , $\boldsymbol{\sigma}$, \mathbf{p} correspond to the speed of light, Kohn-Sham potential, Pauli Spin matrices and momentum operator, respectively. The calculations to obtain SOC matrix elements (SOCME) were carried out using the ADF 2022 package using MO62X functional in conjunction with all-electron TZP basis set.³⁶ COSMO solvation model was used for the calculation of SOCME.

4.2.2 Intersystem Crossing (ISC) rate

ISC or reverse ISC (rISC) rate constants were obtained considering the Fermi Golden rule,^{37, 38}

$$k_{ISC} = \frac{2\pi}{\hbar} \rho_{FC} |\langle S_1 | \hat{H}_{SOC} | T_1 \rangle|^2 \quad (4.2)$$

where $\langle S_1 | \hat{H}_{SOC} | T_1 \rangle$ correspond to the SOC matrix element between singlet and triplet states. ρ_{FC} is the weighted Franck-Condon density of states (DOS). Under Marcus's semi-classical theory approximation, the DOS can be expressed as,³⁹⁻⁴¹

$$\rho_{FC} = \frac{1}{\sqrt{4\pi\lambda_M k_B T}} \exp \left[-\frac{(\Delta E_{ST} + \lambda_M)^2}{4\lambda_M k_B T} \right] \quad (4.3)$$

where, $\lambda_M, k_B, T, \Delta E_{ST}$ denote Marcus reorganization energy, Boltzmann constant, temperature, and adiabatic singlet-triplet gap, respectively. The Marcus reorganization energy corresponds to the combination of two terms: the intramolecular reorganization energy and reorganization energy due to surroundings. We have approximated the total λ_M to be both 0.2 and 0.3 eV.^{41, 42}

4.3 Results and Discussions

4.3.1 Dihedral angle dependent studies of CzPhPmDI and Geometrical aspects

Ground state geometry plays a significant role in determining the overall luminescence behaviour. The phenyl spacer in between the carbazole and PmDI in CzPhPmDI plays a big role. With proper substitution, at the spacer, its orientation with respect to both donor and acceptor can be modulated. Its orientation with respect to donor and acceptor pivots the electronic structure of low-lying excited state (S_1 or T_1).

Table 4.1: Dihedral angles between spacer and donor, acceptor (φ, ψ) and bond lengths (r_1, r_2)

System	φ	ψ	r_1 (Å)	r_2 (Å)
CzMe ₂ PhPmDI	-84	83	1.50	1.43
CzPhPmDI	-60	58	1.49	1.42
CzPhBrPmDI	-65	58	1.49	1.42
BrCzPhPmDI	-60	59	1.49	1.42
Br ₂ CzPhPmDI	-61	60	1.49	1.42

A dihedral angle of 90° disrupts the conjugation leading to HOMO-LUMO separation, which is good for TADF, but other factors do not collinear in favour of TADF.

We have studied the dihedral angle dependence of phenyl spacer of CzPhPmDI on various properties like ΔE_{ST} , spin-orbit coupling between the T_1 and $S_{1/0}$, and oscillator strength for S_0 to S_1 transition (Figure 4.2). We have performed angle dependent studies by changing the dihedral angle by $\pm 10^\circ$ (Figure 4.3) with respect to the equilibrium geometry (a total of $\pm 30^\circ$). Then, we have performed the wavefunction stability analysis on $+30^\circ$ configuration. Our calculations suggest that the system at $+30^\circ$ configurations still have closed-shell electronic configurations and there are no diradical characteristic when the geometries are out-of-equilibrium.

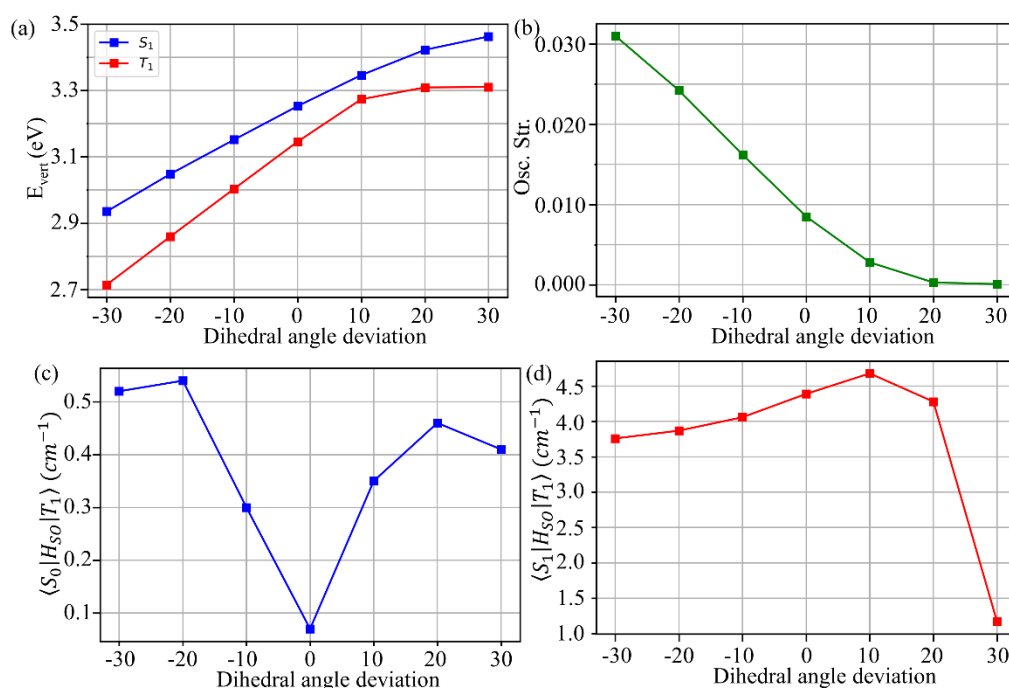


Figure 4.2: Dihedral angle dependence of ΔE_{ST} , oscillator strength for S_0 to S_1 transition and spin-orbit coupling between the T_1 and $S_{1/0}$ in CzPhPmDI

A positive increment indicates that the spacer is becoming perpendicular to both carbazole and PmDI group, while decrement indicates that the spacer is becoming coplanar with both the donor and acceptor unit. At $+30^\circ$, the spacer is almost perpendicular. With the increment, the vertical ΔE_{ST} is initially decreasing, which is expected and at $+10^\circ$ the gap is lowest at 0.07 eV, but gradual increment of the dihedral angle leads to further increase in the gap. While the decrement leads to gradual

increase in the gap possibly due to higher local excited (LE) state character of the excitation. The oscillator strength for the S_1 transition is 0.0085 indicating a hybrid LE state for S_1 at the optimized geometry, but at $+30^\circ$, the oscillator strength is 0.0001, indicating a complete charge transfer (CT) state due to its geometry. The spin-orbit coupling matrix element (SOCME) between S_1 and T_1 increases with the dihedral angle increment, but then the trend goes downward. While the SOCME between S_0 and T_1 , which dictates phosphorescence, is lowest at the optimized geometry. A slight deviation of the dihedral in either direction increases the SOCME value, indicating the change will help in RTP.

Table 4.2: Vertical excitation energies (Singlet) in eV and corresponding oscillator strength in in parenthesis

State	CzMe ₂ PhPmDI	CzPhPmDI	CzPhBrPmDI	BrCzPhPmDI	Br ₂ CzPhPmDI
S_1	3.42(0.0001)	3.25(0.0085)	3.12(0.0065)	3.35(0.0091)	3.43(0.0095)
S_2	3.63(0.0008)	3.79(0.0023)	3.59(0.0014)	3.80(0.0013)	3.83(0.0005)
S_3	3.85(0.0000)	3.92(0.0063)	3.78(0.0000)	3.95(0.0497)	3.96(0.0242)
S_4	3.99(0.0004)	3.93(0.1298)	3.89(0.0412)	4.08(0.0750)	4.09(0.0180)
S_5	4.07(0.0002)	4.03(0.1994)	3.96(0.0935)	4.09(0.0382)	4.12(0.1614)
S_6	4.11(0.0012)	--	4.02(0.2721)	4.11(0.2175)	4.20(0.2129)
S_7	4.30(0.1003)	--	--	--	--

In CzPhPmDI, the dihedral angles are -60° and 58° , indicating the spacer is not fully perpendicular to the donor and acceptor and bond lengths are 1.49 and 1.42 Å. While in CzPhBrPmDI (Br substituted in acceptor), ϕ has increased by 5° , while the bond lengths remained the same. Br substitution at donor does not change the geometrical aspects of the molecular structure. But Me substitution at the phenyl spacer leads to an increment in the dihedral angle and this geometry closely resembles the $+30^\circ$ variant of CzPhPmDI. Both the bond length has increased indicating the conjugation has been destabilized, and HOMO and LUMO are now completely separated, which is advantageous for TADF materials.

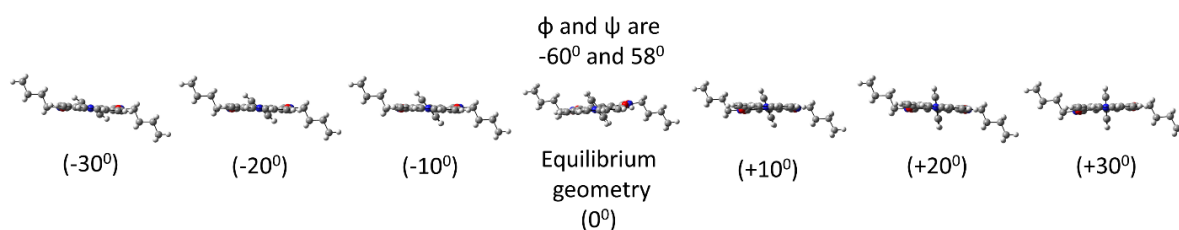


Figure 4.3: Structures for angle-dependent studies

4.3.2 Absorption energies and Jablonski diagram

We have also calculated the vertical excitation energies in B3LYP, CAM-B3LYP, Mo6, Mo62X and wb97xd functional for CzPhPmDI (Table 4.3). Excitation energies calculated using Mo62X and CAM-B3LYP functionals corroborate closely with the experimental observations.²¹ So Mo62X and CAM-B3LYP were used for further excitation energy and excited state optimization for CzPhPmDI and its derivatives. Mo62x and CAM-B3LYP reproduces the experimentally observed LE band (330-350nm) at 308 and 307 nm respectively.²¹ Similar corroboration observed for CT band (425-445 nm) at 372 nm and 381 nm with Mo62x and CAM-B3LYP respectively.²¹

Table 4.3: Excitation energies calculated using the B3LYP, CAM-B3LYP, Mo6, Mo62X, wb97xd and experimental absorption energies in toluene

Expt. (nm)	B3LYP (nm)	CAM-B3LYP (nm)	Mo6 (nm)	Mo62X (nm)	wb97xd (nm)
330-350 (LE)	421	308	387	307	290
425-445 (CT)	661	372	566	381	346

The Jablonski diagram for all the systems is shown in Figure 4.4. In CzPhPmDI, low energy transition (S_1) is hybrid LE in nature and shows absorption at 3.25 eV (381 nm). Br substitution on PmDI unit leads to lowering of energy for the hybrid LE state at 3.12 eV, while Br substitution on donor unit leads to higher energy for hybrid LE states at 3.35 eV and 3.43 eV for mono and dibromo molecules respectively, evident from figure

4.5 (NTO picture). Me substitution on phenyl spacer leads to a complete CT state for the S_1 state at higher energy than CzPhPmDI at 3.42 eV.

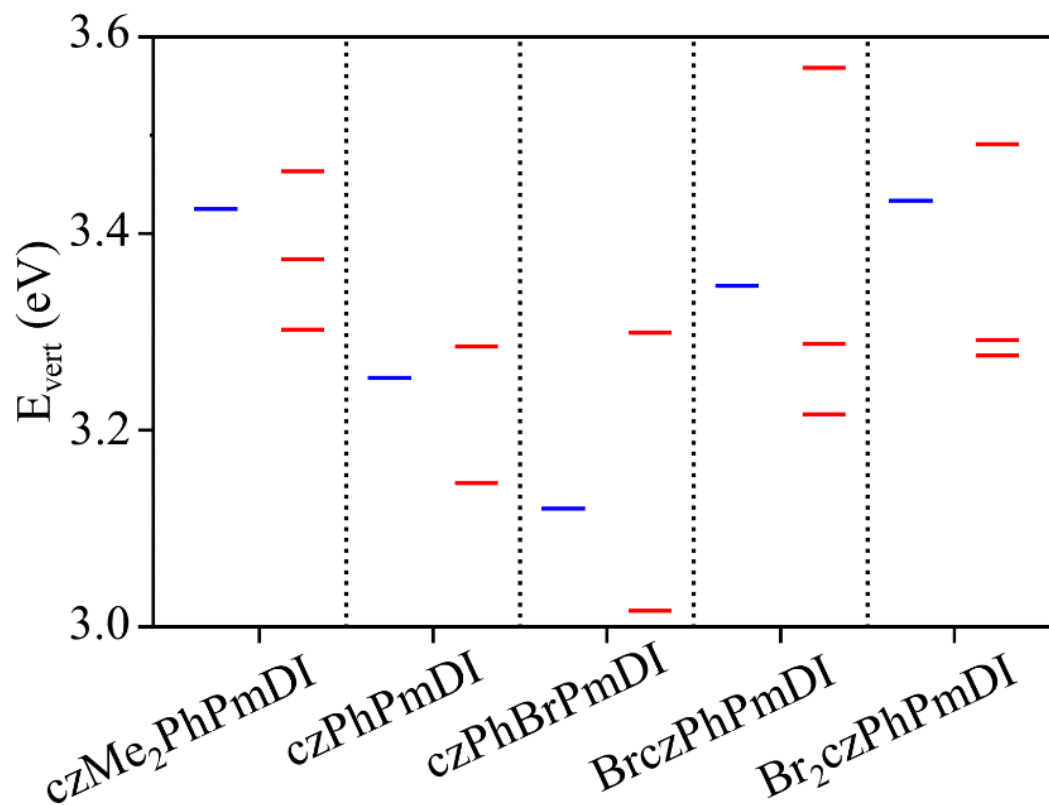


Figure 4.4: Jablonski diagram for CzPhPmDI and its derivatives. Blue lines indicate the singlet state while red lines indicate the triplet states

In CzPhPmDI and CzPhBrPmDI, the T_1 state is also a hybrid LE in nature but the extent of CT character is slightly lower than the S_1 state. The ΔE_{ST} gap in both the systems is ~ 100 meV which is beneficial for rISC. Gradual Br substitution on donor not only increases the CT state absorption energy but also the ΔE_{ST} gap has increased from 0.13 eV to 0.16 eV from BrCzPhPmDI to Br₂CzPhPmDI. In CzMe₂PhPmDI, the vertical singlet-triplet gap is 0.12 eV, which is good TADF and T_1 state is LE in nature and both hole and electron are located on acceptor unit and the transition is π - π^* nature. PmDI is a phosphorescence material, which might help the CzMe₂PhPmDI show phosphorescence.

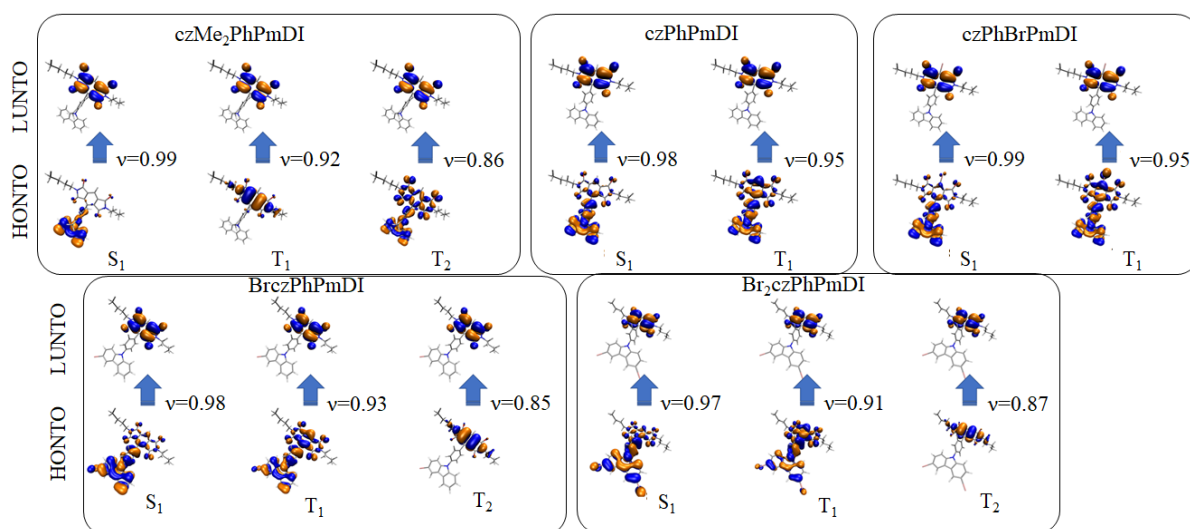


Figure 4.5: NTO diagram for low lying excited state of CzPhPmDI and its derivatives. λ denotes the highest value of singular value decomposition (SVD).

4.3.3 ISC vs rISC and comparison of excited state geometries

We have calculated the root mean square deviation (RMSD) values of the S_1 and T_1 state-optimized geometries with respect to the ground state geometries of the systems (Figure 4.6). For CzPhPmDI, the S_1 state RMSD is 0.18, which is higher than the T_1 state RMSD of 0.13. These values are quite low, indicating lower reorganization in the excited state which helps to reduce the non-radiative decay rates. Heavy atom substitution on donor does not influence the RMSD values of the excited state. These values are quite comparable to the CzPhPmDI. But, heavy atom substitution on PmDI leads to slight lowering of RMSD. While the RMSD values of the excited states for CzMe₂PhPmDI are quite higher. The phenyl spacer was nearly perpendicular at the ground state geometry, but it has rotated internally for both S_1 and T_1 state optimized geometry leading to high RMSD of 0.37 and 0.31 for S_1 and T_1 respectively. Such changes in geometries in excited state might lead to twisted intramolecular charge transfer (TICT) states. TICT can lead to either a red shift in emission or non-radiative relaxation lowering the emission efficiency. However, the phenyl spacer, in both S_1 and T_1 state become more coplanar with the donor and acceptor units, which will increase the overall conjugation. This might cause a red-shifted brighter emission.

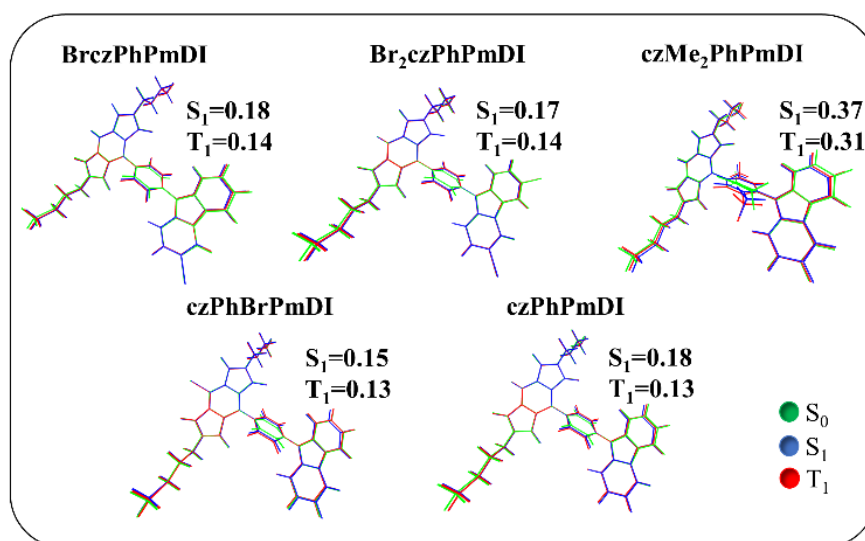


Figure 4.6: RMSD values of S₁ and T₁ states. These values are calculated with respect to S₀ geometries.

Table 4.4: intersystem and reverse intersystem crossing rates between S₁ and T₁ states, where the adiabatic energy gap calculated using M062x functional.

System	ΔE_{ST} (eV)	SOCME (cm⁻¹)	k_{ISC} ($\lambda=0.2\text{eV}$) (s⁻¹)	k_{ISC} ($\lambda=0.3\text{eV}$) (s⁻¹)	k_{rISC} ($\lambda=0.2\text{eV}$) (s⁻¹)	k_{rISC} ($\lambda=0.3\text{eV}$) (s⁻¹)
CzMe ₂ PhPmDI	0.07	4.27	4.63×10^9	1.56×10^9	3.09×10^8	1.04×10^8
CzPhBrPmDI	0.15	18.54	1.75×10^{11}	7.82×10^{10}	5.29×10^8	2.36×10^8
CzPhPmDI	0.14	4.39	9.32×10^9	3.97×10^9	4.17×10^7	1.76×10^7
BrCzPhPmDI	0.15	3.09	4.87×10^9	2.17×10^9	1.47×10^7	6.56×10^6
Br ₂ CzPhPmDI	0.17	3.68	7.46×10^9	3.69×10^9	1.09×10^7	5.14×10^6

Table 4.4 lists the ISC and rISC rates, which are based on adiabatic singlet-triplet energy gap calculated using the M62X functional (excited state geometries optimized with M062X functional), while Table 4.5 lists the same rate constants based on CAM-B3LYP functional (excited state geometries optimized with the CAM-B3LYP

functional). The adiabatic energy gap predicted with the CAM-B3LYP are higher than the Mo62X functional. As a result, the ISC rates calculated with Mo62X functional are lower than the CAM-B3LYP functional, while the rISC rates are higher than the CAM-B3LYP functional. There is substantial difference in ISC vs rISC rate constants ($5.25 \times 10^9 \text{ s}^{-1}$ vs. $7.31 \times 10^6 \text{ s}^{-1}$) calculated with adiabatic energy gap obtained with CAM-B3LYP functional. This makes the system dominant RTP. Although, experimental report says, the system manifests both RTP and TADF characteristics.

The calculated ISC and rISC rates (Table 3) for CzPhPmDI are 3.97×10^9 and $1.76 \times 10^7 \text{ s}^{-1}$ respectively, which is higher than the previous reports. Br substitution on donor has lowered both the ISC and rISC rates because of increased gap and low SOCME values. While ISC and rISC has increased by a fold in CzPhBrPmDI, which is beneficial for dual RTP and TADF. In CzMe₂PhPmDI, the ISC rate is lower than CzPhPmDI, while the rISC rate has increased because of lower singlet-triplet gap. This will be advantageous for efficient TADF characteristics.

Table 4.5: intersystem and reverse intersystem crossing rates between S₁ and T₁ states, where the adiabatic energy gap calculated using CAM-B3LYP functional.

System	ΔE_{ST} (eV)	SOCME (cm ⁻¹)	k_{ISC} ($\lambda=0.2\text{eV}$) (s ⁻¹)	k_{ISC} ($\lambda=0.3\text{eV}$) (s ⁻¹)	k_{rISC} ($\lambda=0.2\text{eV}$) (s ⁻¹)	k_{rISC} ($\lambda=0.3\text{eV}$) (s ⁻¹)
CzMe ₂ PhPmDI	0.23	4.27	1.00×10^{10}	7.31×10^9	1.37×10^6	1.00×10^6
CzPhBrPmDI	0.20	18.54	1.97×10^{11}	1.17×10^{11}	8.63×10^7	5.10×10^7
CzPhPmDI	0.17	4.39	1.06×10^{10}	5.25×10^9	1.48×10^7	7.31×10^6
BrCzPhPmDI	0.24	3.09	5.08×10^9	4.00×10^9	4.73×10^5	3.71×10^5
Br ₂ CzPhPmDI	0.31	3.68	4.34×10^9	6.34×10^9	2.68×10^4	3.93×10^4

4.4 Conclusions

In this chapter, we have studied a dual emitter (RTP and TADF) D- π -A system CzPhPmDI and heavy atom substituted and phenyl spacer modified derivatives. We have performed dihedral angle dependence of excited-state properties of phenyl

spacer of CzPhPmDI. At the optimized geometry the dihedral angles (with donor and acceptor) are nearly 60° . A dihedral angle increment initially leads to lowering of singlet-triplet gap, because of increased CT nature of S_1 and T_1 transitions. But further increment (almost perpendicular with both donor and acceptor) leads to an increase in ΔE_{ST} . With Me substitution on the spacer, we have been able to realize a system where the spacer is perpendicular to both carbazole and PmDI unit. The reason behind increasing singlet-triplet gap can be attributed to different transition natures of S_1 and T_1 . In the excited state geometry, the spacer twists and leads to a generation of TICT state. Because of increased collinearity, we expect it will show red-shifted bright emissions for TADF. The rISC rates in CzMe₂PhPmDI have increased by one-fold in comparison to CzPhPmDI due to lower adiabatic ΔE_{ST} . We have also studied the effects of heavy atom substitution on both donor and acceptor. Br substitution on PmDI lowers the CT state energy, but the SOCME between S_1 and T_1 state has increased, which helps in boosting both the ISC and rISC which is beneficial for dual RTP and TADF emissions. While Br substitution on carbazole does not influence much the triplet harvesting process.

Bibliography

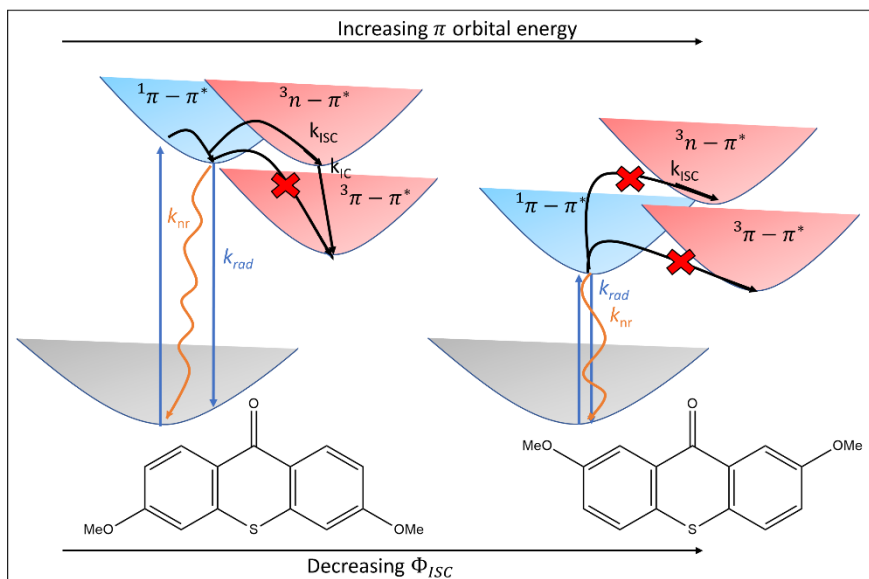
- [1] H. Nakanotani, T. Higuchi, T. Furukawa, K. Masui, K. Morimoto, M. Numata, H. Tanaka, Y. Sagara, T. Yasuda, C. Adachi *Nature Communications*. **2014**, *5*, 4016.
- [2] M. Y. Wong, E. Zysman-Colman *Advanced Materials*. **2017**, *29*, 1605444.
- [3] Y. Tao, K. Yuan, T. Chen, P. Xu, H. Li, R. Chen, C. Zheng, L. Zhang, W. Huang *Advanced Materials*. **2014**, *26*, 7931-7958.
- [4] Z. Yang, Z. Mao, Z. Xie, Y. Zhang, S. Liu, J. Zhao, J. Xu, Z. Chi, M. P. Aldred *Chemical Society Reviews*. **2017**, *46*, 915-1016.
- [5] S. Xu, R. Chen, C. Zheng, W. Huang *Advanced Materials*. **2016**, *28*, 9920-9940.
- [6] H. Chen, X. Xing, J. Miao, C. Zhao, M. Zhu, J. Bai, Y. He, H. Meng *Advanced Optical Materials*. **2020**, *8*, 1901651.
- [7] P. L. dos Santos, M. K. Etherington, A. P. Monkman *Journal of Materials Chemistry C*. **2018**, *6*, 4842-4853.
- [8] Y. Liu, C. Li, Z. Ren, S. Yan, M. R. Bryce *Nature Reviews Materials*. **2018**, *3*, 18020.
- [9] A. K. Pal, K. Bhattacharyya, A. Datta *The Journal of Physical Chemistry A*. **2020**, *124*, 11025-11037.
- [10] W. Z. Yuan, X. Y. Shen, H. Zhao, J. W. Y. Lam, L. Tang, P. Lu, C. Wang, Y. Liu, Z. Wang, Q. Zheng, J. Z. Sun, Y. Ma, B. Z. Tang *The Journal of Physical Chemistry C*. **2010**, *114*, 6090-6099.
- [11] O. Bolton, K. Lee, H.-J. Kim, K. Y. Lin, J. Kim *Nature Chemistry*. **2011**, *3*, 205-210.
- [12] H. Wu, W. Chi, Z. Chen, G. Liu, L. Gu, A. K. Bindra, G. Yang, X. Liu, Y. Zhao *Advanced Functional Materials*. **2019**, *29*, 1970063.
- [13] S. Kuila, S. J. George *Angewandte Chemie International Edition*. **2020**, *59*, 9393-9397.
- [14] J. Yang, X. Zhen, B. Wang, X. Gao, Z. Ren, J. Wang, Y. Xie, J. Li, Q. Peng, K. Pu, Z. Li *Nature Communications*. **2018**, *9*, 840.
- [15] Goudappagouda, A. Manthanath, V. C. Wakchaure, K. C. Ranjeesh, T. Das, K. Vanka, T. Nakanishi, S. S. Babu *Angewandte Chemie International Edition*. **2019**, *58*, 2284-2288.
- [16] T. Zhang, X. Ma, H. Wu, L. Zhu, Y. Zhao, H. Tian *Angewandte Chemie International Edition*. **2020**, *59*, 11206-11216.
- [17] M. A. El-Sayed *The Journal of Chemical Physics*. **1963**, *38*, 2834-2838.

- [18] B. Ventura, A. Bertocco, D. Braga, L. Catalano, S. d'Agostino, F. Grepioni, P. Taddei *The Journal of Physical Chemistry C*. **2014**, *118*, 18646-18658.
- [19] S. Garain, S. Kuila, B. C. Garain, M. Kataria, A. Borah, S. K. Pati, S. J. J. A. C. I. E. George. **2021**, *60*, 12323-12327.
- [20] S. Kuila, K. V. Rao, S. Garain, P. K. Samanta, S. Das, S. K. Pati, M. Eswaramoorthy, S. J. George *Angewandte Chemie International Edition*. **2018**, *57*, 17115-17119.
- [21] S. Kuila, S. Garain, G. Banappanavar, B. C. Garain, D. Kabra, S. K. Pati, S. J. J. T. J. o. P. C. B. George. **2021**, *125*, 4520-4526.
- [22] S. Sasaki, G. P. C. Drummen, G.-i. Konishi *Journal of Materials Chemistry C*. **2016**, *4*, 2731-2743.
- [23] X.-W. Sun, L.-Y. Peng, Y.-J. Gao, Q. Fang, G. Cui *The Journal of Physical Chemistry A*. **2022**, *126*, 4176-4184.
- [24] A. D. Becke *The Journal of Chemical Physics*. **1993**, *98*, 5648-5652.
- [25] C. Lee, W. Yang, R. G. Parr *Physical Review B*. **1988**, *37*, 785-789.
- [26] T. Yanai, D. P. Tew, N. C. Handy *Chemical Physics Letters*. **2004**, *393*, 51-57.
- [27] Y. Zhao, D. G. Truhlar *Theoretical Chemistry Accounts*. **2008**, *120*, 215-241.
- [28] J.-D. Chai, M. Head-Gordon *The Journal of Chemical Physics*. **2008**, *128*, 084106.
- [29] M. Alipour, P. Fallahzadeh *Physical Chemistry Chemical Physics*. **2016**, *18*, 18431-18440.
- [30] G. Scalmani, M. J. Frisch *The Journal of Chemical Physics*. **2010**, *132*, 114110.
- [31] R. L. Martin *The Journal of Chemical Physics*. **2003**, *118*, 4775-4777.
- [32] M. J. Frisch, G. W. Trucks, H. B. Schlegel, G. E. Scuseria, M. A. Robb, J. R. Cheeseman, G. Scalmani, V. Barone, G. A. Petersson, H. Nakatsuji, X. Li, M. Caricato, A. V. Marenich, J. Bloino, B. G. Janesko, R. Gomperts, B. Mennucci, H. P. Hratchian, J. V. Ortiz, A. F. Izmaylov, J. L. Sonnenberg, Williams, F. Ding, F. Lipparini, F. Egidi, J. Goings, B. Peng, A. Petrone, T. Henderson, D. Ranasinghe, V. G. Zakrzewski, J. Gao, N. Rega, G. Zheng, W. Liang, M. Hada, M. Ehara, K. Toyota, R. Fukuda, J. Hasegawa, M. Ishida, T. Nakajima, Y. Honda, O. Kitao, H. Nakai, T. Vreven, K. Throssell, J. A. Montgomery Jr., J. E. Peralta, F. Ogliaro, M. J. Bearpark, J. J. Heyd, E. N. Brothers, K. N. Kudin, V. N. Staroverov, T. A. Keith, R. Kobayashi, J. Normand, K. Raghavachari, A. P. Rendell, J. C. Burant, S. S. Iyengar, J. Tomasi, M. Cossi, J. M. Millam, M. Klene, C. Adamo, R. Cammi, J. W. Ochterski, R. L. Martin, K. Morokuma, O. Farkas, J. B. Foresman, D. J. Fox in *Gaussian 16 Rev. C.01*, Vol. (Ed. ^Eds.: Editor), City, **2016**.

- [33] E. van Lenthe, J. G. Snijders, E. J. Baerends *The Journal of Chemical Physics*. **1996**, *105*, 6505-6516.
- [34] E. van Lenthe, R. van Leeuwen, E. J. Baerends, J. G. Snijders *International Journal of Quantum Chemistry*. **1996**, *57*, 281-293.
- [35] F. Wang, T. Ziegler *The Journal of Chemical Physics*. **2005**, *123*, 154102.
- [36] G. te Velde, F. M. Bickelhaupt, E. J. Baerends, C. Fonseca Guerra, S. J. A. van Gisbergen, J. G. Snijders, T. Ziegler *Journal of Computational Chemistry*. **2001**, *22*, 931-967.
- [37] V. Lawetz, G. Orlandi, W. Siebrand *The Journal of Chemical Physics*. **1972**, *56*, 4058-4072.
- [38] G. W. Robinson, R. P. Frosch *The Journal of Chemical Physics*. **1963**, *38*, 1187-1203.
- [39] D. Beljonne, Z. Shuai, G. Pourtois, J. L. Bredas *The Journal of Physical Chemistry A*. **2001**, *105*, 3899-3907.
- [40] Q. Ou, J. E. Subotnik *The Journal of Physical Chemistry C*. **2013**, *117*, 19839-19849.
- [41] P. K. Samanta, N. J. English *The Journal of Physical Chemistry C*. **2020**, *124*, 8178-8185.
- [42] B. C. Garain, P. K. Samanta, S. K. Pati *The Journal of Physical Chemistry A*. **2021**, *125*, 6674-6680.

Chapter 5

5 Unraveling the Efficiency of Thioxanthone Based Triplet Sensitizers: A Detailed Theoretical Study*



* Work reported in this chapter is published in: Bidhan Chandra Garain, S. K Pati, *ChemPhysChem*, e202100753, 2022

5.1 Introduction

Photochemical activation by irradiation with UV/vis light without catalysts or reagents is highly desirable and economically viable for a green focus society. These reactions generally occur at the lowest triplet or singlet excited states. In fact, one of the greener applications of the triplet state is its sensitization so that it becomes indispensable for photo-redox catalysis apart from other photochemical and photonic applications.¹⁻⁸ Triplet photosensitizers (PSs) transfer exciton to the triplet excited state of a substrate when direct excitation is ineffective. Apart from acting as photocatalysts, triplet PSs could be used for photodynamic therapy, photoinduced hydrogen production from water and triplet-triplet annihilation.⁹⁻¹⁶ After initial excitation, a higher singlet state (S_n ; $n \geq 1$) gets populated and comes down to the lowest excited singlet state S_1 (Kasha's rule). Now the fate of the higher energy singlet state (S_1) is two-fold: either a straightforward radiative transition from S_1 to S_0 (Fluorescence), or it can transfer the excitons to the triplet state using non-radiative intersystem crossing (ISC) mechanism. An ideal photosensitizer should have a high absorption coefficient for efficient exciton population generation at low concentration, high intersystem crossing quantum yield (Φ_{ISC}) for productive T_1 state population and long-lived T_1 state for effective population transfer to the substrate.¹⁷⁻¹⁹ However, in simple terms, synthesizing a triplet PS is still quite difficult, especially without heavy atoms. The unclear relationship between molecular architecture and the rate constants of intersystem crossing (ISC) is responsible for this phenomenon. Often researchers find chemical substitution is the most viable option to enhance certain molecular properties,^{20, 21} however, there are cases where substitution may lead to evanescence of Φ_{ISC} .

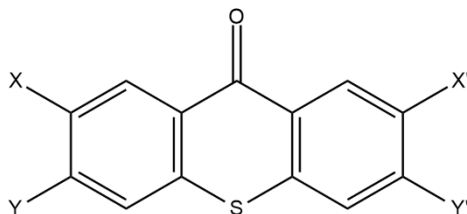
ISC involves a transition between 2 electronic states of different spin manifolds. The two parameters which influence the ISC are (1) high spin-orbit coupling matrix elements (SOCMEs) and (2) adiabatic energy gap between the states.²²⁻²⁴ The 1st condition can be achieved via the substitution of heavy atom. In the absence of heavy atom effect, the only way to harness the reasonable spin-orbit coupling is via a change in orbital type during transition (e.g., $n-\pi^*$ to $\pi-\pi^*$, El-Sayed's rule). The 2nd condition is the extent of adiabatic energy gap between two states, which can be controlled chemically, by substitution of various groups or atoms, which causes the shift in energy levels (n , π , π^*) that are involved in the transition (e.g., $n-\pi^*$ to $\pi-\pi^*$).

Thioxanthone and its derivatives are known to be an excellent class of heavy-atom free triplet photosensitizers.^[25-27] Recently, Elliot *et al.* have proposed a rational design for the synthesis of a new set of thioxanthone derivatives as triplet sensitizers.^[28] They have investigated the possibility of forming triplet PSs in these derivatives, which show photo-absorption in a wide wavelength region, from UV to visible, ranging from 350-450 nm with high extinction coefficient. In fact, the experimental group have corroborated their experimental findings with the computational (TDDFT) results.

Interestingly, the substitution at different positions on thioxanthone leads to different λ_{\max} and depending on the substitutions, the ISC rate also varies. In fact, the magnitude of Φ_{ISC} depends crucially on these two factors. In their study, 3 or 3' substitution of -OMe or -F on thioxanthone led to an increment of absorption energy (shorter λ_{\max} ; $E(\text{eV}) \sim 1240/\lambda(\text{nm})$) than the unsubstituted thioxanthone, while similar group substitution at 2 or 2' position led to lowering of absorption energy (longer λ_{\max}). The triplet PSs with high absorption energies have high Φ_{ISC} . In fact, in terms of absorption energy, the thioxanthone derivatives with low absorption energies have not been able to harvest triplet excitons and performed poorly as a photocatalyst. A good photocatalyst should have high triplet harvesting ability (high Φ_{ISC}). Interestingly, the interplay among nature of substitutions and triplet harvesting ability has not been explored in detail in any system in the current literature.

In this chapter, we have carried out detail DFT and TDDFT-based calculations on these 8 systems to delineate the effect of substitution (Figure 5.1) on both the absorption profile and the Φ_{ISC} . We have found that the major ISC channel is S_1 to $^3n-\pi^*$. There is also a radiative transition from S_1 to S_0 (k_{rad}) which is $\pi-\pi^*$ in nature that competes with ISC. In thioxanthone without any substitution, the $\Delta E_{S_1-n\pi^*}$ is slightly positive. As a result, the rate of ISC (k_{ISC}) from S_1 to the triplet manifold (mainly T_4) is higher than the radiative decay rate (k_{rad}) and non-radiative decay rate (k_{nr}) from S_1 to S_0 . However, the ISC channel becomes remote for thioxanthone system with -OMe or F substitution at 2 or 2' positions. It is because of lowering of S_1 state energy although $^3n-\pi^*$ state energy remains almost the same. As a result, the $\Delta E_{S_1-n\pi^*}$ becomes highly positive leading to disruption of ISC channel. So, these systems are not being able to harvest triplet excitons which is necessary for photosensitization. While similar substitutions at 3 or 3' positions alleviate the S_1 state energy rendering suitable singlet-triplet gap, leading to a higher ISC quantum yield suitable for triplet

photosensitization. We hope the results of this chapter will further strengthen the understanding of TX-based triplet sensitizers which we believe can perform as good photocatalyst and in turn help in designing more efficient systems.



No.	Name	X	X'	Y	Y'	Φ_{ISC}
1	3, 3'-MeOTX	H	H	OMe	OMe	0.93
2	3, 3'-FTX	H	H	F	F	0.92
3	3-MeOTX	H	H	H	OMe	>0.90
4	3-FTX	H	H	H	F	0.83
5	TX	H	H	H	H	0.76
6	ITX	H	C(CH ₃) ₂	H	H	0.86
7	2-F, 2'-MeOTX	OMe	F	H	H	0.62
8	2, 2'-MeOTX	OMe	OMe	H	H	0.66

Figure 5.1: Systems studied in this work along with their ISC quantum yields (Φ_{ISC}). Φ_{ISC} were experimentally calculated from bleach recovery studies

5.2 Computational Methodology

5.2.1 Geometry Optimization and Optical Absorption

Ground state geometries were optimized using MO6 functional in conjunction with the 6-31+g(d) basis set. Optical excitations were calculated using B3LYP (HF% ~ 22) and MO6 (HF% = 27).²⁹⁻³² Although absorption energies performed using B3LYP are better, adiabatic triplet energies deviate more from the experimental value than MO6. Since the intersystem crossing rate constant calculation involves adiabatic triplet state energies and adiabatic T₁ state energy closely corroborate with experimentally observed triplet energies of the studied systems. So, we chose MO6 for further optimization of the higher energy singlet and triplet states. We have optimized the first singlet and triplet excited state (S₁) and ³n-π* state whenever that is found below the S₁ state. We have not optimized the in-between ³π-π* states, as the spin-orbit coupling between S₁ and those states is very small and as a result, they impart less significance the ISC rate. All the DFT and TDDFT calculation were performed in acetonitrile considering Polarizable Continuum Model (PCM) to compare our results with the experimental results.³³ Natural Transition Orbital (NTO) analyses were done to

characterize the excited state characteristics.³⁴ We have carried out all the above calculations using the Gaussian 16 software package with default convergence criteria.³⁵

5.2.2 Spin-Orbit Coupling

The SOC matrix elements were calculated using the zeroth order regular approximation (ZORA) Hamiltonian.³⁶⁻³⁸ The SOC operator \hat{H}_{SOC} , within ZORA is defined as,

$$\hat{H}_{SOC} = \frac{c^2}{(c^2 - V_{KS})^2} \boldsymbol{\sigma} \cdot (\nabla V_{KS} \times \mathbf{p}) \quad (5.1)$$

where c , V_{KS} , $\boldsymbol{\sigma}$, \mathbf{p} is the speed of light, Kohn-Sham potential, Pauli Spin matrices, momentum operator respectively. The SOC effects were considered as a perturbation on the scalar relativistic (SR) orbitals after the SCF and TD-DFT calculations (pSOC-TDDFT). Spin-Orbit coupling matrix elements were calculated using the ADF 2017 package using the MO6 functional in conjunction with all-electron TZP basis set.³⁹ In most of the chapters and in fact here also, we have used COSMO solvation model as implemented in the package.⁴⁰

5.2.3 Intersystem Crossing rate

Non-radiative decay from the S_1 state to the ${}^3n-\pi^*$ state due to ISC can be calculated using the Fermi Golden rule,^{41, 42}

$$k_{ISC} = \frac{2\pi}{\hbar} \rho_{FC} |\langle S_1 | \hat{H}_{SOC} | T \rangle|^2 \quad (5.2)$$

$\langle S_1 | \hat{H}_{SOC} | T \rangle$ is the SOC matrix element between two states. ρ_{FC} is the weighted density of states, which under Marcus's semi-classical theory approximation can be expressed as,⁴³⁻⁴⁵

$$\rho_{FC} = \frac{1}{\sqrt{4\pi\lambda k_B T}} \exp \left[-\frac{(\Delta E_{ST} + \lambda)^2}{4\lambda k_B T} \right] \quad (5.3)$$

where, $\lambda, k_B, T, \Delta E_{ST}$ is the Marcus reorganization energy, Boltzmann constant, temperature, and adiabatic singlet-triplet gap respectively. The Marcus reorganization

energy consists of two parts, one is intramolecular reorganization energy and reorganization energy due to surroundings. We have approximated the total λ to be both 0.2 and 0.3 eV.⁴⁵

5.2.4 Fluorescence decay rate

The fluorescence decay rate is calculated using Einstein's A coefficient,⁴⁶⁻⁴⁸

$$A_{fi} = \frac{(E_f - E_i)^3}{3\varepsilon_0\pi\hbar^4c^3} |\langle f|\hat{\mu}|i\rangle|^2 \quad (5.4)$$

E_f, E_i are the initial and final state energies and $\langle f|\hat{\mu}|i\rangle$ is the corresponding transition dipole moment. In case of prompt fluorescence $k_F = A_{fi}$.

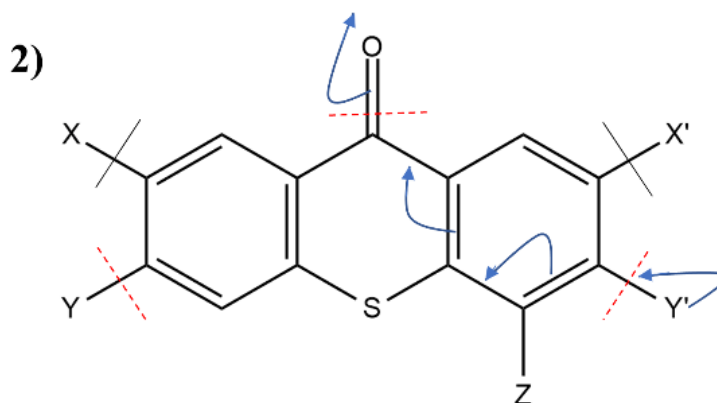
5.3 Results and Discussions

5.3.1 Ground state and Frontier Molecular Orbitals

We start with the ground state structural aspects and the FMO characteristics of the thioxanthone derivatives (1 – 8). Table 5.1 lists some of the relevant structural aspects, like C=O, C-OMe and C-F bond lengths in the ground state. Molecules containing OMe group at the 3 or 3' positions have higher C=O and lower C-OMe bond length values compared to the systems with OMe group at the 2 or 2' positions or systems with F at 3 (3') or 2 (2') positions. This can be explained by the mesomeric (+M) effect shown by the OR (R=Me) groups (Figure 5.2). C-F bond length in 8 (where F is at 2' position) is higher than the systems where F is at 3 or 3' positions. Interestingly, since F has a lower +M effect than OMe, the change in C=O bond length is not prominent in the case of molecule 8.

Table 5.1: C=O, C-OMe and C-F bond length at the S_0 state

System	C=O	C-F	C-OMe
1	1.237	--	1.347
2	1.233	1.342	--
3	1.235	--	1.346
4	1.233	1.342	--
5	1.234	--	--
6	1.234	--	--
7	1.232	1.348	1.354
8	1.233	--	1.355

Figure 5.2: +M effect of the Y or Y' substitution. Black and red lines indicate the presence of a node at π , π^* level respectively

The effect of substitution on relevant FMOs (n , π , π^* orbitals) (Figure 5.3) is quite substantial and significant, which need to be discussed in detail. The n orbital is primarily dominated by the C=O bonding and molecules (1 and 3) with higher C=O bond length contribute to high n orbital energy than the other substitutions or unsubstituted system(s). While in the case of π orbital, there is a node passing between the C-X (X = -OMe at 2 or 2') bond, such a node is slightly shifted towards Y group

when Y = -OMe and it is at 3 or 3' positions. In fact, the shift leads to the higher energy of the π molecular orbital of 7 and 8, in comparison to the rest of the molecules. In the case of π^* orbital, molecules with -OMe or F at 2 or 2' positions get stabilized than the rest of the systems. There is a node passing through the C-Y bond, while such a node is missing between the C-X bond, which in turn leads to the stabilization of π^* .

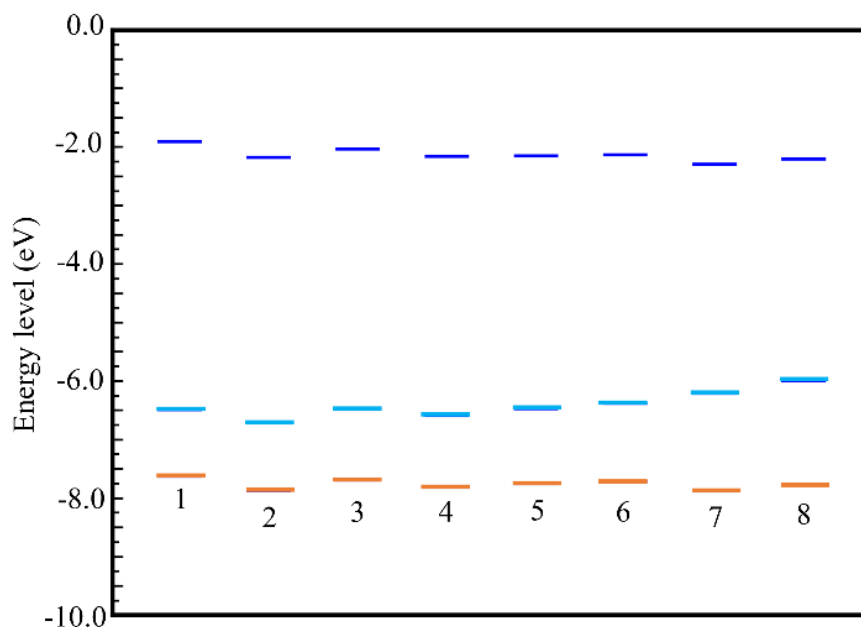


Figure 5.3: FMO energies of the thioxanthone and its derivatives. Orange lines denote the n orbital energies, sky-blue lines denote the π energies and blue lines denote the π^* energies.

5.3.2 Absorption Energy and Jablonski Profile

We have carried out computations of the ground state and the excitation energies, which contains the singlet excited and low energy triplet states. These energies are listed in Table 5.2, while energies calculated with B3LYP functional are listed in Table 5.3. Thioxanthone and its derivatives showed optical absorption due to S_0 to S_1 transition evident from our TDDFT calculations. These absorption energies range from 338 nm (in UV region) for 1, where -OMe is substituted at 3 and 3' positions to 412 nm (in the visible light region) for 8, where -OMe substitution at the 2 and 2' positions.

Table 5.2: theoretical and experimental absorption (in acetonitrile) and triplet energies calculated using MO6 functional in conjunction with 6-31+g(d) basis set calculated in acetonitrile.

System	E_{abs}(expt.) nm.	E_{abs} (MeCN) nm. (f)	E_T (expt.) nm.	E_T (calc.) nm.
1	354	338(0.063)	401	427
2	362	338(0.091)	413	440
3	367	348(0.080)	422	454
4	370	347(0.097)	424	458
5	380	356(0.102)	436	474
6	385	362(0.098)	449	487
7	408	396(0.100)	509	567
8	415	412(0.098)	517	590

These transitions are HOMO-LUMO based and π - π^* in nature which accounts for the high oscillator strength for almost all the transitions. Calculated triplet energies (T_1 to S_0) range from 427 nm for 1 to 590 nm for 8. Similarly, these transitions also arise from π - π^* based transitions (Figure 5.4). Our calculated TDDFT absorption (vertical) and triplet energies (adiabatic) corroborate well with the experimentally reported energy values. Even our calculated fluorescence energy for thioxanthone at 392 nm in acetonitrile corroborates well with earlier experimental report at 409 nm.⁴⁹

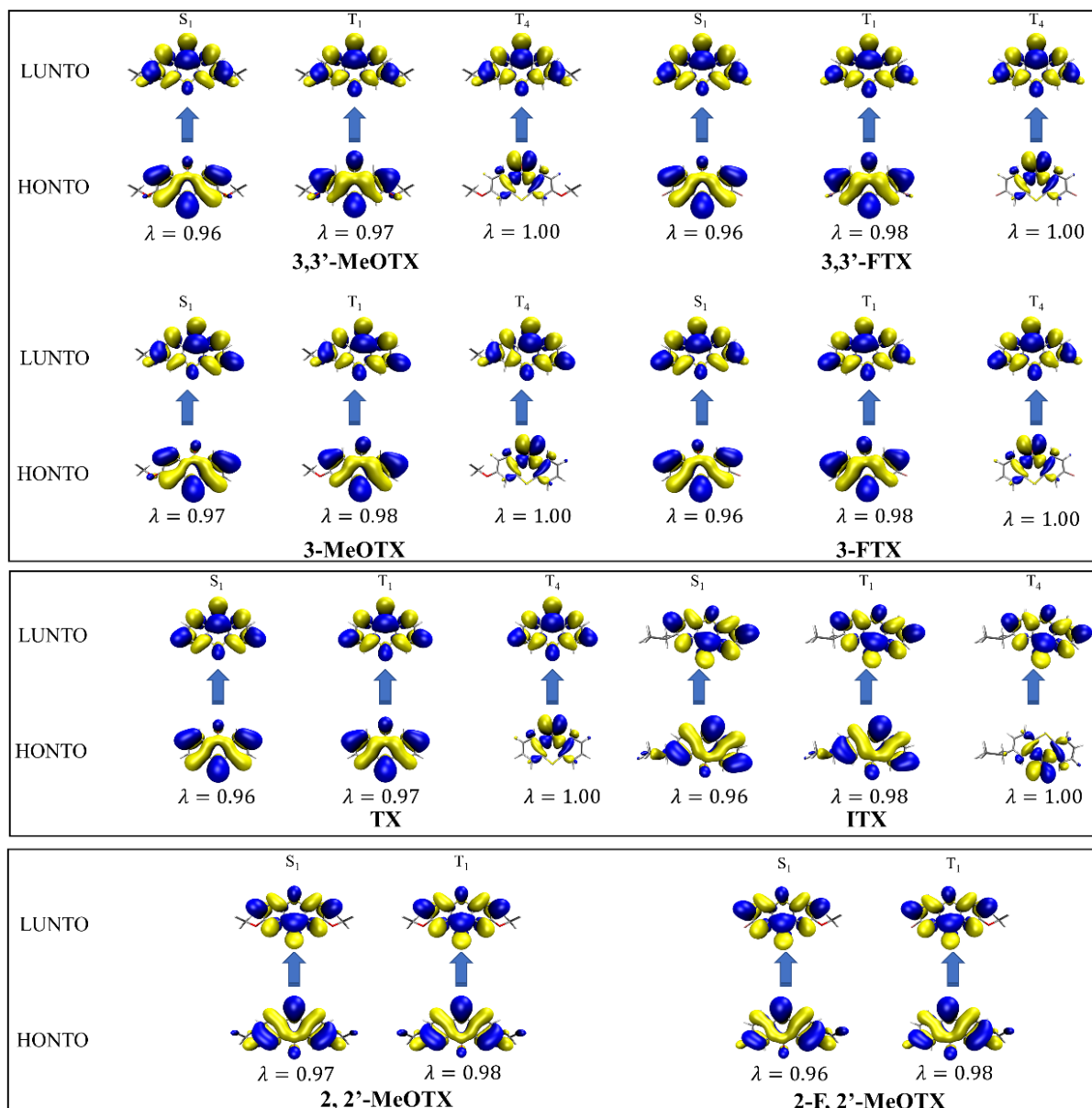


Figure 5.4: Relevant NTOs of the thioxanthone derivatives. λ denotes the coefficient for the transition from HONTO to LUNTO after singular value decomposition (SVD)

Table 5.3: Theoretical absorption and triplet energies calculated using B3LYP functional in conjunction with 6-31+g(d) basis set.

No.	E _{abs} (expt.) nm.	E _{abs} (calc.) (<i>f</i>) MeCN nm.	E _T (expt.) nm.	E _T (calc.) nm.
1	354	350 (0.0588)	401	455
2	362	349 (0.0861)	413	470
3	367	359 (0.0749)	422	481
4	370	358 (0.0905)	424	486
5	380	367 (0.0950)	436	502
6	385	372 (0.0911)	449	514
7	408	400 (0.0936)	509	599
8	415	426 (0.0869)	517	623

The downward trend in the absorption energies from 1 to 8 can be explained by the stabilization of π^* orbitals and the destabilization of π orbitals while moving from 1 to 8, as explained earlier. While we have seen a downward trend for S_1 and T_1 transitions due to their π - π^* nature, the vertical energy difference between S_0 and T_4 states showed a little descending trend due to its n - π^* transition characteristics. These comparative energies are pictorially shown in the Jablonski diagram (Figure 5.5). Interestingly, as a result of this, the $\Delta E_{S_1-n\pi^*}$ gap increases while going from 1 to 8. For compounds, 1-4, the energy gap is positive, which suggests that the lowest excited singlet state (S_1) is higher in energy than the $3n$ - π^* , while for compounds, 5 and 6, the gap is little negative. For the compounds, 7 and 8, however, the gap is highly negative, indicating any transitions from S_1 to $3n$ - π^* is energetically impossible, which is deleterious for high Φ_{ISC} and this is the reason that the triplet PSs are inadequate for photosensitized reactions.

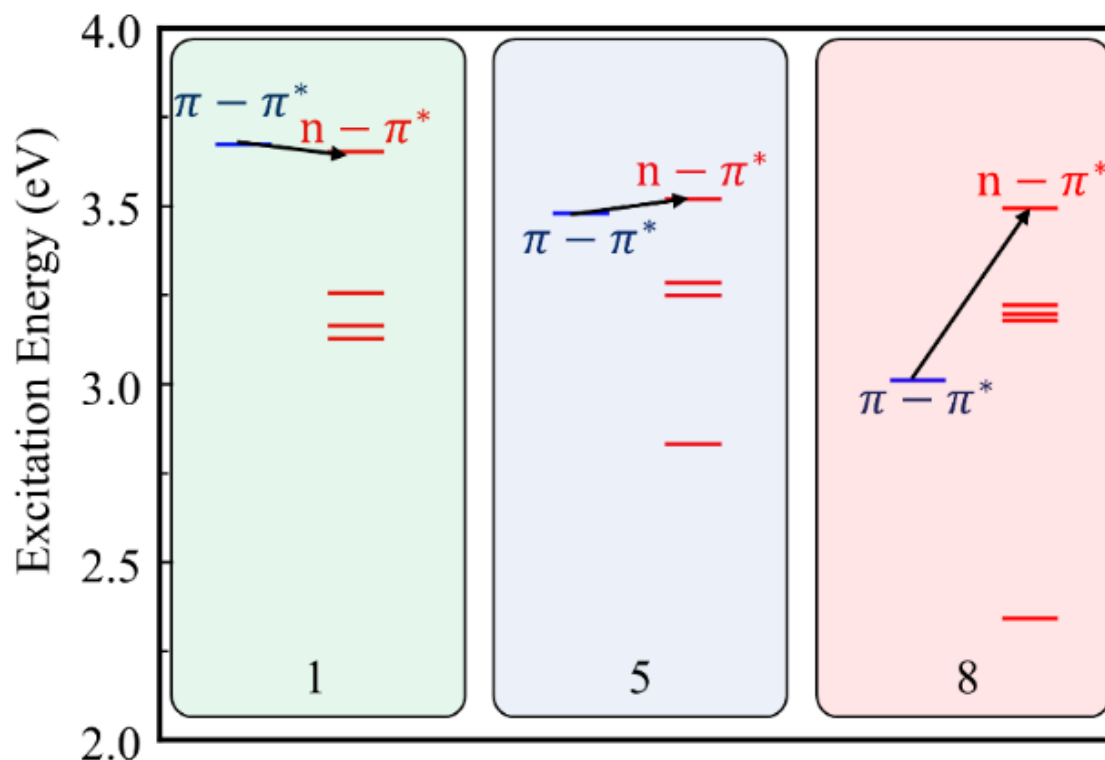


Figure 5.5: Jablonski diagram of 1, 5 and 8.

5.3.3 Excited state geometry comparison

We have looked at in details and compared the geometries of the S_1 and T_1 excited states with the geometry of the ground state (S_0). Some important bond lengths are listed in Table 5.4. C=O bond length has increased in both S_1 and T_1 states compared to the S_0 state, while the extent of increment is higher for T_1 state. The C-F bond length on the other hand has not increased to that extent and both the bond lengths are similar in both S_1 and T_1 geometries. Interestingly, for the C-OMe bond length, it has increased for the compound, 1 and 2, while for the compound, 7 and 8, it has decreased from S_0 geometry, and the extent of decrement is higher in T_1 than the S_1 state. In figure 5.6, we have shown the Root Mean Square Deviation (RMSD) of excited state (S_1 and T_1 state) geometries with respect to its ground state (S_0) geometries. For TX derivatives with -OMe substitution, S_1 state RMSD is higher than the T_1 state geometries. On the other hand, for unsubstituted TX or other TX derivatives, the trend has been reversed. Any non-radiative decay happens through structural changes, caused by the vibronic couplings. Since RMSD qualitatively represent the structural changes between the two states, RMSD is also a parameter, which can qualitatively predict the non-radiative

decay from excited state to ground state. We believe that although RMSD values of the substituted TXs are higher than the unsubstituted TX, small increment in the RMSD values would not change the non-radiative decay rates drastically.

Table 5.4: C=O, C-OMe and C-F bond length at the S_1 and T_1 state

System	S_1			T_1		
	C=O	C-F	C-OMe	C=O	C-F	C-OMe
1	1.27	--	1.35	1.28	--	1.36
2	1.26	1.35	--	1.28	1.35	--
3	1.26	--	1.35	1.27	--	1.35
4	1.26	1.35	--	1.27	1.35	--
5	1.26	--	--	1.26	--	--
6	1.26	--	--	1.27	--	--
7	1.26	1.35	1.34	1.27	1.35	1.34
8	1.26	--	1.34	1.27	--	1.33

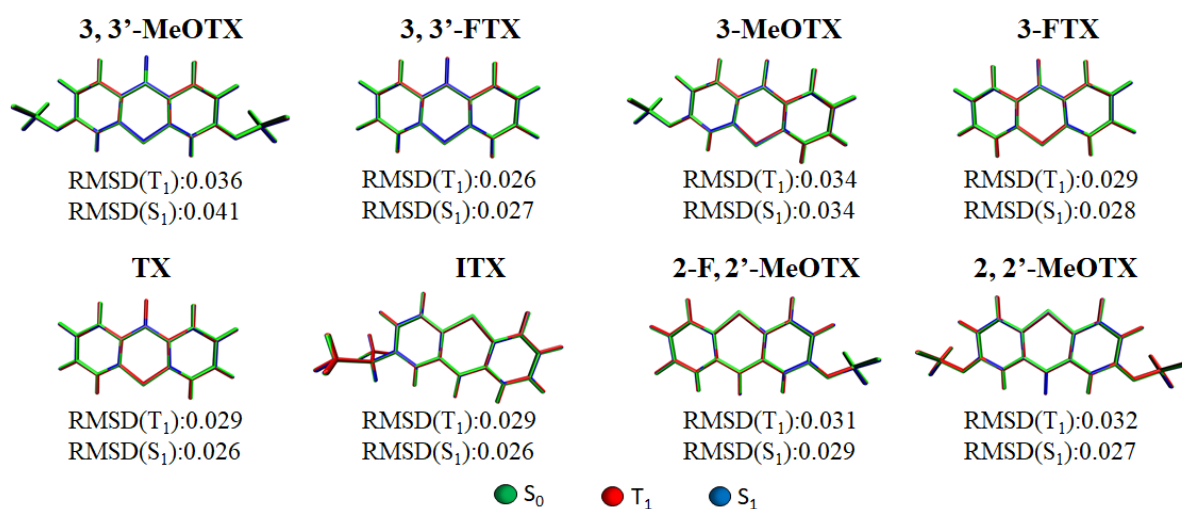


Figure 5.6: S_0 , T_1 , S_1 state geometry and Root Mean Square Deviation (RMSD) values of T_1 and S_1 geometries with respect to its ground state S_0 geometry

5.3.4 Intersystem crossing rate constants and its comparison with fluorescence rates

High Φ_{ISC} requirement is proportionate to high k_{ISC} value, which in turn depends on the two most important parameters: (1) adiabatic singlet-triplet energy gap and the (2) spin-orbit coupling matrix elements (SOCME) between the singlet-triplet state. The SOCME values are significantly higher for the S_1 and ${}^3n-\pi^*$ states, compared to ${}^3\pi-\pi^*$ states, evident from Table 5.5. Such change in the SOC matrix element values can be explained with the help of the \hat{H}_{SO} operator. Under central field approximation, the SOC operator reads as,⁵⁰

$$\hat{H}_{SO} = \sum_{\mu} \sum_i \frac{2c^2}{(2c^2 - V_{\mu i})^2} \frac{1}{r_{\mu i}} \frac{\partial V_{\mu i}}{\partial r_{\mu i}} \left[\frac{1}{2} (\hat{l}_{\mu i+} \hat{s}_{\mu i-} + \hat{l}_{\mu i-} \hat{s}_{\mu i+}) + \hat{l}_{\mu iz} \hat{s}_{\mu iz} \right] \quad (5.5)$$

where, $V_{\mu i}$ is the r -dependent potential energy function between electron i and nucleus μ . $\hat{l}_{\pm}[\hat{s}_{\pm}]$ is creation and annihilation operator for the orbital [spin] angular momentum. $\hat{l}_z[\hat{s}_z]$ is the z component of the orbital [spin] angular momentum operator. The operator form in the above equation implies that the spin-flipping (either up to down or vice versa) should be accompanied by orbital flipping (down to up or vice versa) to conserve the total orbital angular momentum. The system under investigation uses just the p -orbitals for the creation of frontiers molecular orbitals. So, accordingly, only the p -orbitals will be affected by the \hat{l}_{\pm} operator. Therefore, upon spin flipping, the orbital arrangement should change to maintain total angular momentum. Since the molecules studied here do not contain heavy atoms with d -orbitals, only the orbital angular momentum of p -orbitals are influenced by spin-orbit coupling operator. π orbitals are made up of p_z (p_o), upon spin flip, they get converted into $p_{1/-1}$ orbitals which are linear combination of $p_{x/y}$. Generally, n orbitals are made up of $p_{1/-1}$. But for the S_1 to ${}^3\pi-\pi^*$ transition, the p_z orbitals do not change, and they remain in the z plane, while for the S_1 to ${}^3n-\pi^*$ transition, the p_z orbitals get converted into $p_{x,y}$ orbitals upon spin flipping. This explains a high value of SOCME between these two states, while in case of other states, the SOCME is lower than in orders of 3-4. In fact, since k_{ISC} depends on the square of the SOCME, contribution to the k_{ISC} by those states are smaller by 6-8 times in comparison to the transition from S_1 to ${}^3n-\pi^*$.

Table 5.5: Dominating intersystem crossing rate constants and radiative decay rate constants

System	State	Transition type	ΔE_{ST} (eV)	SOCME (cm ⁻¹)	k_{ISC} (s ⁻¹) from S ₁	k_{ISC} (s ⁻¹) from S ₁	k_{rad} (s ⁻¹) from S ₁
					$\lambda=0.2$	$\lambda=0.3$	
1	T ₁	$\pi - \pi^*$	-0.46	0.002	8.76×10^1	8.23×10^2	
	T ₄	$n - \pi^*$	-0.11	19.762	1.52×10^{11}	5.73×10^{10}	6.38×10^7
2	T ₁	$\pi - \pi^*$	-0.52	0.001	4.07×10^0	9.88×10^1	
	T ₄	$n - \pi^*$	-0.12	22.527	2.14×10^{11}	8.39×10^{10}	8.30×10^7
3	T ₁	$\pi - \pi^*$	-0.50	0.004	1.18×10^2	2.07×10^3	
	T ₄	$n - \pi^*$	-0.03	20.196	5.80×10^{10}	1.82×10^{10}	7.04×10^7
4	T ₁	$\pi - \pi^*$	-0.53	0.001	2.97×10^0	8.53×10^1	
	T ₄	$n - \pi^*$	-0.05	21.869	9.27×10^{10}	3.00×10^{10}	7.97×10^7
5	T ₁	$\pi - \pi^*$	-0.54	0	0	0	
	T ₄	$n - \pi^*$	0.12	21.472	1.88×10^9	7.35×10^8	7.90×10^7
6	T ₁	$\pi - \pi^*$	-0.53	0.007	1.45×10^2	4.18×10^3	
	T ₄	$n - \pi^*$	0.09	21.350	4.50×10^9	1.59×10^9	7.54×10^7
7	T ₁	$\pi - \pi^*$	-0.56	0.007	5.35×10^1	2.60×10^3	5.28×10^7
8	T ₁	$\pi - \pi^*$	-0.56	0.005	2.73×10^1	1.33×10^3	5.65×10^7

As a result, we have excluded the intermediate states between S₁ and 3n- π^* from the calculations of k_{ISC} rates, as their contribution to the Φ_{ISC} is relatively low. Even a lower ΔE_{ST} gap would not be able to manifest higher k_{ISC} than a state with high ΔE_{ST} but with high SOCME values (El-Sayed's rule). The calculated k_{ISC} (high contribution to Φ_{ISC}) are listed in Table 5.5. The k_{ISC} due to such transitions for 1-4 are 1.52×10^{11} , 2.14×10^{11} , 5.80×10^{10} , 9.27×10^{10} s⁻¹ respectively, significantly much higher than its S₁ to T₁ transition rates 8.76×10^1 , 4.07×10^0 , 1.18×10^2 , 2.97×10^0 s⁻¹. The lower rate constants can be attributed to the low values of spin-orbit coupling matrix elements (SOCME). While for 5 and 6, the k_{ISC} is little lower than the previous systems, 1.88×10^9 and 4.50×10^9 s⁻¹ respectively, due to high ΔE_{ST} gap values. But in cases of compound, 7 and 8, this channel cannot be observed due to very high ΔE_{ST} gap.

Another, competitive channels are the radiative and non-radiative decay from the S_1 to S_0 state. The radiative transitions are $\pi-\pi^*$ based. So, oscillator strength is quite substantial, and the rate constants are almost similar $O(10^7 s^{-1})$. This value is much closer to the experimentally calculated k_{rad} value of $4.4 \times 10^7 s^{-1}$ for thioxanthone in cyclohexane, where fluorescence quantum yield is 0.95.⁵¹

But lifetimes ($10^{-7} s$) calculated from these radiative rate constants are much smaller than the S_1 state lifetime reported experimentally ($\sim 10 \times 10^{-9} s$ or even lower). Thus, it is evident that the non-radiative decay rates are nearly 2 to 10 times higher than the radiative decay rates. ($\tau_s = 1/(k_{rad} + k_{nr} + k_{ISC})$; where $k_{nr} \gg k_{ISC} + k_{rad}$), which is also supported by the fact that thioxanthone does not have good fluorescence quantum yield in acetonitrile.⁴⁹ Vibronic coupling plays a significant role in non-radiative decays from S_1 to S_0 . Marian *et al.* have clearly shown vibronic coupling strength changes for S_1 to S_0 non-radiative decay in different solvents.⁵² In non-polar solvents, due to lower stabilization of n-orbitals, the energy levels of ${}^1\pi-\pi^*$ and ${}^1n-\pi^*$ become similar. In fact, in such cases, the vibronically active out-of-plane modes make S_1 to S_0 non-radiative transition faster. While in polar solvents, the vibronic coupling is weakened leading to lower non-radiative transition and higher fluorescence quantum yield.

However, in this work, we have carried out all the calculations in acetonitrile solvent for all the systems and their RMSD values (which is a qualitative indicator of non-radiative decay) for S_1 state in comparison to S_0 state is similar for all the systems we have studied in this chapter. We have calculated the singlet state lifetime with the intersystem crossing rate obtained with $\lambda=0.2$ eV (Since $k_{ISC} \gg k_{rad} + k_{nr}$). These lifetime values (Table 5.6) are almost in close agreement with the experimentally obtained lifetime data except for thioxanthone. The agreement is quite good for system 1-4 evident from Table 5.6, while there is slight deviation in the theoretical corroboration for 5 and 6. Generally, internal conversion (IC) rate constants are even higher (Kasha's rule) than these intersystem crossing rate constants, indicating singlet excitons will get converted into triplet excitons through high ISC compared to k_{rad} . This explains the ordering of Φ_{ISC} with substitution.

Table 5.6: Calculated singlet state lifetime for systems 1-5 where ISC rate is much higher than radiative and non-radiative decay rate ($k_{ISC} \gg k_{rad} + k_{nr}$)

System	k_{ISC} (s^{-1}) from S_1 $\lambda=0.2$	$\tau_s \sim 1/k_{ISC}$ (ps)	Expt. Observation (ps)
1	1.52×10^{11}	6.58	10
2	2.14×10^{11}	4.67	10.5
3	5.80×10^{10}	17.24	31
4	9.27×10^{10}	10.78	21
5	1.88×10^9	531.91	70 ⁵³
6	4.50×10^9	222.22	270

5.4 Conclusions

We have examined the absorption and triplet energies of both unsubstituted and a series of substituted thioxanthenes and delineated the effect of substitution on excited state energy levels, which renders the difference in the efficiency of triplet harvesting. Substitution of -OMe at 3 or 3' positions lead to an increment in the C=O bond length owing to the mesomeric effect of the -OMe group, which also leads to lower C-OMe bond length in 3 or 3' position compared to similar group substitution at 2 or 2' position. The major ISC channel in thioxanthone or its derivatives are S_1 to $^3n-\pi^*$. -OMe or F substitution at 2 or 2' positions lead to the rise of π energy state and lowering of the π^* state. As a result of this, the S_1 state energy of such derivatives get lowered and the $^3n-\pi^*$ state energy remains the same, which makes the ISC channel inaccessible due to positive singlet-triplet energy gap. The other competitive processes to this ISC, are the radiative decay from S_1 to S_0 , which is $\pi-\pi^*$ in nature. So, the oscillator strength is quite high for this transition. The k_{rad} for the systems are $\sim 10^7$ s^{-1} . There is also a non-radiative decay process from S_1 to S_0 , which is 2 to 10 times higher than the radiative decay channel. Systems 1-4 (substitution at 3 or 3' position with a group having mesomeric effect) show a $k_{ISC} \sim 10^{11} > 10^7$ s^{-1} . This explains a high intersystem quantum yield ($\Phi_{ISC} \geq 0.9$) which is a must have requirement to be an efficient photocatalyst. Overall, our results indicate that judicious substitution at 3 or 3' position of thioxanthone with proper +M effect might lead a good triplet

photosensitizer in the UV region. In fact, we conjecture that our results will open new synthetic strategies mainly chromophore modification in the field of organic triplet photosensitization and photocatalysis.

Bibliography

- [1] Q. Zhao, F. Li, C. Huang *Chemical Society Reviews*. **2010**, *39*, 3007-3030.
- [2] J. Zhao, W. Wu, J. Sun, S. Guo *Chemical Society Reviews*. **2013**, *42*, 5323-5351.
- [3] J. Xuan, W.-J. Xiao *Angewandte Chemie International Edition*. **2012**, *51*, 6828-6838.
- [4] L. Shi, W. Xia *Chemical Society Reviews*. **2012**, *41*, 7687-7697.

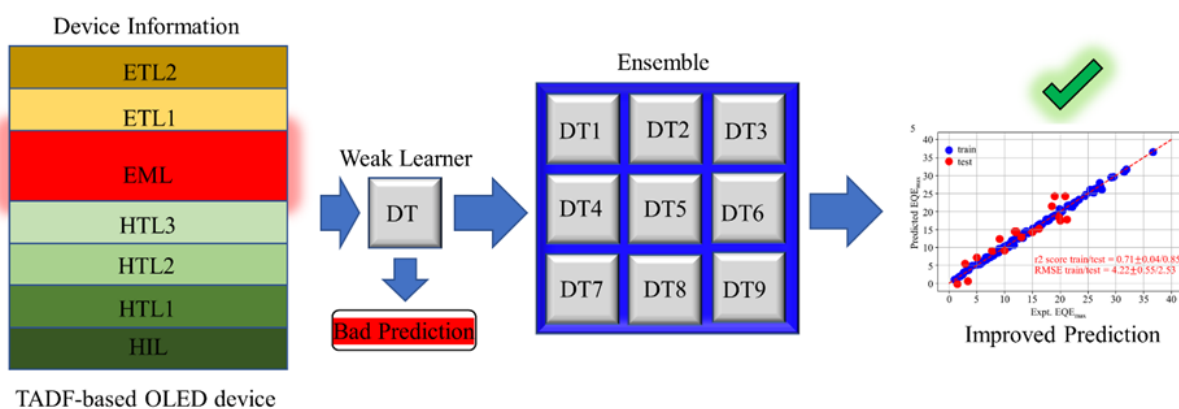
- [5] D. Ravelli, M. Fagnoni, A. Albini *Chemical Society Reviews*. **2013**, *42*, 97-113.
- [6] S. Maity, M. Zhu, R. S. Shinabery, N. Zheng *Angewandte Chemie International Edition*. **2012**, *51*, 222-226.
- [7] M. Neumann, S. Földner, B. König, K. Zeitler *Angewandte Chemie International Edition*. **2011**, *50*, 951-954.
- [8] Y.-Q. Zou, L.-Q. Lu, L. Fu, N.-J. Chang, J. Rong, J.-R. Chen, W.-J. Xiao *Angewandte Chemie International Edition*. **2011**, *50*, 7171-7175.
- [9] A. Gorman, J. Killoran, C. O'Shea, T. Kenna, W. M. Gallagher, D. F. O'Shea *Journal of the American Chemical Society*. **2004**, *126*, 10619-10631.
- [10] S. O. McDonnell, M. J. Hall, L. T. Allen, A. Byrne, W. M. Gallagher, D. F. O'Shea *Journal of the American Chemical Society*. **2005**, *127*, 16360-16361.
- [11] A. Kamkaew, S. H. Lim, H. B. Lee, L. V. Kiew, L. Y. Chung, K. Burgess *Chemical Society Reviews*. **2013**, *42*, 77-88.
- [12] A. E. O'Connor, W. M. Gallagher, A. T. Byrne *Photochemistry and Photobiology*. **2009**, *85*, 1053-1074.
- [13] T. N. Singh-Rachford, F. N. Castellano *Coordination Chemistry Reviews*. **2010**, *254*, 2560-2573.
- [14] P. Ceroni *Chemistry – A European Journal*. **2011**, *17*, 9560-9564.
- [15] A. Monguzzi, R. Tubino, S. Hoseinkhani, M. Campione, F. Meinardi *Physical Chemistry Chemical Physics*. **2012**, *14*, 4322-4332.
- [16] Y. C. Simon, C. Weder *Journal of Materials Chemistry*. **2012**, *22*, 20817-20830.
- [17] J. Zhao, S. Ji, W. Wu, W. Wu, H. Guo, J. Sun, H. Sun, Y. Liu, Q. Li, L. Huang *RSC Advances*. **2012**, *2*, 1712-1728.
- [18] Y. You, W. Nam *Chemical Society Reviews*. **2012**, *41*, 7061-7084.
- [19] J. I. Goldsmith, W. R. Hudson, M. S. Lowry, T. H. Anderson, S. Bernhard *Journal of the American Chemical Society*. **2005**, *127*, 7502-7510.
- [20] A. Loudet, K. Burgess *Chemical Reviews*. **2007**, *107*, 4891-4932.
- [21] Y. Zhou, J. Yoon *Chemical Society Reviews*. **2012**, *41*, 52-67.
- [22] C. M. Marian *WIREs Computational Molecular Science*. **2012**, *2*, 187-203.
- [23] X. Gao, S. Bai, D. Fazzi, T. Niehaus, M. Barbatti, W. Thiel *Journal of Chemical Theory and Computation*. **2017**, *13*, 515-524.
- [24] S. Bissesar, D. M. E. van Raamsdonk, D. J. Gibbons, R. M. Williams in Spin Orbit Coupling in Orthogonal Charge Transfer States: (TD-)DFT of Pyrene—Dimethylaniline, Vol. 27 (Ed. ^Eds.: Editor), City, **2022**.

- [25] R. M. Williams, I. V. Khudyakov, M. B. Purvis, B. J. Overton, N. J. Turro *The Journal of Physical Chemistry B*. **2000**, *104*, 10437-10443.
- [26] K. Dietliker, S. Broillet, B. Hellrung, P. Rzadek, G. Rist, J. Wirz, D. Neshchadin, G. Gescheidt *Helvetica Chimica Acta*. **2006**, *89*, 2211-2225.
- [27] N. F. Nikitas, P. L. Gkizis, C. G. Kokotos *Organic & Biomolecular Chemistry*. **2021**, *19*, 5237-5253.
- [28] L. D. Elliott, S. Kayal, M. W. George, K. Booker-Milburn *Journal of the American Chemical Society*. **2020**, *142*, 14947-14956.
- [29] A. D. Becke *The Journal of Chemical Physics*. **1993**, *98*, 5648-5652.
- [30] B. Miehlich, A. Savin, H. Stoll, H. Preuss *Chemical Physics Letters*. **1989**, *157*, 200-206.
- [31] C. Lee, W. Yang, R. G. Parr *Physical Review B*. **1988**, *37*, 785-789.
- [32] Y. Zhao, D. G. Truhlar *Theoretical Chemistry Accounts*. **2008**, *120*, 215-241.
- [33] G. Scalmani, M. J. Frisch *The Journal of Chemical Physics*. **2010**, *132*, 114110.
- [34] R. L. Martin *The Journal of Chemical Physics*. **2003**, *118*, 4775-4777.
- [35] M. J. Frisch, G. W. Trucks, H. B. Schlegel, G. E. Scuseria, M. A. Robb, J. R. Cheeseman, G. Scalmani, V. Barone, G. A. Petersson, H. Nakatsuji, X. Li, M. Caricato, A. V. Marenich, J. Bloino, B. G. Janesko, R. Gomperts, B. Mennucci, H. P. Hratchian, J. V. Ortiz, A. F. Izmaylov, J. L. Sonnenberg, Williams, F. Ding, F. Lipparini, F. Egidi, J. Goings, B. Peng, A. Petrone, T. Henderson, D. Ranasinghe, V. G. Zakrzewski, J. Gao, N. Rega, G. Zheng, W. Liang, M. Hada, M. Ehara, K. Toyota, R. Fukuda, J. Hasegawa, M. Ishida, T. Nakajima, Y. Honda, O. Kitao, H. Nakai, T. Vreven, K. Throssell, J. A. Montgomery Jr., J. E. Peralta, F. Ogliaro, M. J. Bearpark, J. J. Heyd, E. N. Brothers, K. N. Kudin, V. N. Staroverov, T. A. Keith, R. Kobayashi, J. Normand, K. Raghavachari, A. P. Rendell, J. C. Burant, S. S. Iyengar, J. Tomasi, M. Cossi, J. M. Millam, M. Klene, C. Adamo, R. Cammi, J. W. Ochterski, R. L. Martin, K. Morokuma, O. Farkas, J. B. Foresman, D. J. Fox in *Gaussian 16 Rev. C.01*, Vol. (Ed. ^Eds.: Editor), City, **2016**.
- [36] E. van Lenthe, J. G. Snijders, E. J. Baerends *The Journal of Chemical Physics*. **1996**, *105*, 6505-6516.
- [37] E. van Lenthe, R. van Leeuwen, E. J. Baerends, J. G. Snijders *International Journal of Quantum Chemistry*. **1996**, *57*, 281-293.
- [38] F. Wang, T. Ziegler *The Journal of Chemical Physics*. **2005**, *123*, 154102.

- [39] G. te Velde, F. M. Bickelhaupt, E. J. Baerends, C. Fonseca Guerra, S. J. A. van Gisbergen, J. G. Snijders, T. Ziegler *Journal of Computational Chemistry*. **2001**, *22*, 931-967.
- [40] A. Klamt *WIREs Computational Molecular Science*. **2011**, *1*, 699-709.
- [41] V. Lawetz, G. Orlandi, W. Siebrand *The Journal of Chemical Physics*. **1972**, *56*, 4058-4072.
- [42] G. W. Robinson, R. P. Frosch *The Journal of Chemical Physics*. **1963**, *38*, 1187-1203.
- [43] D. Beljonne, Z. Shuai, G. Pourtois, J. L. Bredas *The Journal of Physical Chemistry A*. **2001**, *105*, 3899-3907.
- [44] Q. Ou, J. E. Subotnik *The Journal of Physical Chemistry C*. **2013**, *117*, 19839-19849.
- [45] P. K. Samanta, N. J. English *The Journal of Physical Chemistry C*. **2020**, *124*, 8178-8185.
- [46] K. Schmidt, S. Brovelli, V. Coropceanu, D. Beljonne, J. Cornil, C. Bazzini, T. Caronna, R. Tubino, F. Meinardi, Z. Shuai, J.-L. Brédas *The Journal of Physical Chemistry A*. **2007**, *111*, 10490-10499.
- [47] R. C. Hilborn *American Journal of Physics*. **1982**, *50*, 982-986.
- [48] P. K. Samanta, S. K. Pati *Physical Chemistry Chemical Physics*. **2015**, *17*, 10053-10058.
- [49] J. C. Dalton, F. C. J. J. o. t. A. C. S. Montgomery. **1974**, *96*, 6230-6232.
- [50] P. K. Samanta, D. Kim, V. Coropceanu, J.-L. Brédas *Journal of the American Chemical Society*. **2017**, *139*, 4042-4051.
- [51] R. Mundt, T. Villnow, C. T. Ziegenbein, P. Gilch, C. Marian, V. Rai-Constapel *Physical Chemistry Chemical Physics*. **2016**, *18*, 6637-6647.
- [52] V. Rai-Constapel, S. Salzmann, C. M. Marian *The Journal of Physical Chemistry A*. **2011**, *115*, 8589-8596.
- [53] C. Ley, F. Morlet-Savary, P. Jacques, J. P. Fouassier *Chemical Physics*. **2000**, *255*, 335-346.

Chapter 6

6 Improved Prediction of Maximum EQE in TADF-based OLEDs Through Ensemble Learning*



* Work reported in this chapter is based on: Bidhan Chandra Garain, Swapan K Pati, DOI: [10.26434/chemrxiv-2022-636c2](https://doi.org/10.26434/chemrxiv-2022-636c2), 2023 and codes deposited in GitHub (https://github.com/BidhanChandra/ML_EQE_max_Prediction).

6.1 Introduction

The advancement in the research on thermally activated delayed fluorescence (TADF)-based materials has added a whole new dimension to the field of OLEDs with prodigious applications ranging from wall lighting, imaging to sensing.¹⁻³ From conventional fluorescence emitters, since the ground state is in singlet state, we could only harvest one-quarter (singlet state: triplet states is 1:3) of the generated singlet excitons for emission. Whereas in TADF emitters, the other three-quarter of the total generated excitons get converted into triplet excitons, which can again be harvested into singlet excitons through reverse-intersystem crossing (rISC) mechanism. So, theoretically, we can achieve 100% internal quantum efficiency (IQE). Efficient rISC requires the proper balance of two contrasting parameters, low singlet-triplet gap between first excited singlet state (S_1) and lowest triplet state (T_1) and moderate spin-orbit coupling (SOC) between these two states. The traditional way to synthesize a TADF emitter is to make a perpendicular donor-acceptor (D-A) system either through a bond between donor (D) and acceptor (A) or through a spiro-conjunction between D and A. This architecture reduces the overlap between HOMO and LUMO inducing charge-transfer (CT) characteristics in the low-lying excited states (S_1 and T_1) and effectively reduces the energy gap. While this phenomenon lowers the coupling strength between these two states owing to the same symmetry of excitation and reduces the oscillator strength for the transition from S_1 to the ground state (S_0). In the last couple of decades, a large number of developments happened in the field of efficient organic TADF-based chromophores and their synthesis. With such burgeoning, alternative approaches to D-A systems have been scanned. Hatakeyama *et al.* have shown that the nitrogen manifests a opposite resonance effect than boron and relative para-substitution of boron and nitrogen can enhance such opposite resonance effect, which can significantly separate the HOMO-LUMO.⁴ Devising coplanar system with high oscillator strength and low ΔE_{ST} have been shown by Chen *et al.*⁵ Even the theoretical studies involving spin-vibronic coupling or hyperfine coupling has made a significant impact explaining rISC pathways in TADF systems.⁶⁻⁸ Samanta *et al.* have shown the effect of LE characteristics in triplet manifolds for a better rISC rate.⁹

With the evolution of data-driven analysis, researchers have started using ML-based models. Aspuru-Guzik *et al.* have used neural nets and subsequent quantum-

chemistry calculations for accurate prediction of rISC rate (k_{rISC}) and from high throughput virtual screening they have been able to screen TADF emitter with $EQE_{max} \sim 22\%$.¹⁰ Meftahi *et al.* have predicted the power conversion efficiency (PCE) using BRANNLP method with an r^2 score of 0.72.¹¹ Chan *et al.* have predicted the current efficiency (CE) for blue phosphorescent materials from various device descriptors like layer thickness and triplet energy of electron transport layer through various machine learning algorithms, like XGBoost (Extreme gradient boosting), Random Forest (RF) and k-Nearest Neighbor (kNN).¹² RF has shown the highest efficiency with r^2 score of 0.67/0.73 for train/test datasets. Troisi *et al.* have also done a virtual screening of 700 TADF emitters out of 40000 systems for quantum chemistry calculations and predicted 125 highly efficient emitters among them, whose structures significantly deviate from the D-A architecture.¹³ Shu *et al.* also have used the high throughput virtual screening (HTVS) method for scanning better TADF emitters.¹⁴ However, to the best of our knowledge, none of these models emphasize the relationship between EQE_{max} and device architecture. Recently, Lee has proposed an RF-based ML approach to predict EQE_{max} only for green TADF emitters with r^2 score of 0.85/0.74 for train/ test dataset with RMSE of 4.16/4.72 respectively using just host and guest parameters.¹⁵ Importance of the similarity matrix between host and guest has been emphasized in this work.

Generally, in the OLED field particularly in TADF-based OLEDs, there are two steps. The first one is to synthesize a chemical system (GUEST) that will have a low ΔE_{ST} and thus it can manifest a high PLQY or internal quantum efficiency. Most of the previously mentioned works try to fill that void.

Another part comes next, which is to engineer a device out of the synthesized material, which is very important for OLED application.

This chapter does not survey the molecular structure part. That is beyond the scope of this work chapter. Instead, this chapter is rather centred around the device architecture part. From the literature, it is evident that a molecule with small ΔE_{ST} or high PLQY does not exhibit a high external quantum efficiency (EQE). The output parameter not only depends on the previous two parameters but rather on the overall device architecture. Finding the optimum device architecture has been a trial and error-based method, which is extremely expensive because of both the instrumental requirements (like spin coating or chemical vapour deposition) and the cost of the

materials of HTL and ETL. Although, interestingly over the years many devices have been developed. So, with data availability and massive growth of machine learning (ML) in recent years, ML-based predictions for EQE_{\max} for any TADF emitters irrespective of their emissive range (or CIE value) is still lacking.

This work chapter probes on the engineering aspect of the TADF-based OLEDs field rather than the chemical aspect of molecular structure of GUEST through ML-based approach. This work tries to understand what the optimum requirements of the device could be. Device structure beyond host and guest makes a significant impact on EQE_{\max} like various energy levels of the hole and electron transport layers and each of their thickness. Certainly, a change in device fabrication may lead to a certain change in EQE_{\max} .

In this chapter, we have compiled our own database from the existing device information for TADF-based OLEDs available in the literature and have employed ensemble learning (Bagging and Boosting) based models for improved predictions of EQE_{\max} . Among the models, Gradient Boosting (GB) has shown the best performance with an r^2 score of 0.71/0.84 for train/test set and RMSE of 4.22/2.53 respectively, which is good considering the applicability of the model to all TADF emitters along with device selectivity with close range metrics compared to the models with high selectivity to chromophores with specific emissive range. After the model implementations, we have checked the feature importance score to analyse the effects of the input features to give insights.

We do hope that this work chapter would make a noteworthy impact on further research on TADF-based OLEDs. All the descriptors can be obtained experimentally and learning curve is still rising to indicate this model will perform even better with addition of more data points. The computation is easily accessible to experimentalists since all the computations can be done using free cloud computation (Google Colab).

6.2 Computational Methodology

In this work, we have collected 123 device information of 123 different chromophores and from there 30 features have been selected.^{4, 5, 12, 16-72} They are **(1)** - HOMO energy of GUEST **(2)** -LUMO energy of GUEST **(3)** -HOMO energy of HOST

(4) -LUMO energy of HOST **(5)** ΔE_{ST} of GUEST **(6)** -HOMO energy of hole injection layer (HIL) **(7)** HIL thickness **(8)** -HOMO energy of 1st hole transport layer (HTL1) **(9)** -LUMO energy of 1st hole transport layer (HTL1) **(10)** HTL1 thickness **(11)** -HOMO energy of 2nd hole transport layer (HTL2) **(12)** -LUMO energy of 2nd hole transport layer (HTL2) **(13)** HTL2 thickness **(14)** -HOMO energy of 3rd hole transport layer (HTL3) **(15)** -LUMO energy of 3rd hole transport layer (HTL3) **(16)** HTL3 thickness **(17)** total HTL thickness (HTL1 + HTL2 + HTL3) **(18)** emissive layer (EML) thickness **(19)** T_1 energy of 1st electron transport layer (ETL1) **(20)** -HOMO of ETL1 **(21)** -LUMO of ETL1 **(22)** ETL1 thickness **(23)** -HOMO energy of ETL2 **(24)** -LUMO energy of ETL2 **(25)** ETL2 thickness **(26)** total ETL thickness (ETL1 + ETL2) **(27)** Work function of the cathode **(28)** Cathode thickness **(29)** doping concentration **(30)** PLQY in HOST matrix. In the case of the absence of HTL3 material, the thickness is 0 and HOMO-LUMO energy is taken to be of HLT2 material. The same approach is also taken when ETL1 material is absent.

Since the total number of device data points is only 123, we have to divide this for training and for the test datasets as well as have to cross validate the part of training datasets to avoid overfitting. In fact, we have considered 85% of the total data, 104 as a training dataset and 15% as a test dataset (19). Further, we did 4-fold cross-validation on train dataset ($4 * 26 + 19 = 104 + 19 = 123$) while evaluating any ML model. We have performed all the calculations using Google colab.

6.2.1 Cross Validation

Cross validation is generally done to prevent overfitting. However, it is not done on overall dataset. Test set is always kept hidden from the model, otherwise results will be biased. In general, the dataset is divided in 3 sets: (1) train set, (2) validation set (3) test set.

Models are generally employed on the train set, then initially it is checked on validation set for the performance checking. Once that is good, finally the model is tested on test dataset. Cross-validation generally does that only with the requirement of the validation dataset.

Scikit-Learn which has implemented the cross-validation method, has said the following in their official documentation,

https://scikit-learn.org/stable/modules/cross_validation.html

6.2.2 Metrics

Pearson correlation: Correlation coefficients measure the nature and strength of the relationships between two variables. One such important correlation coefficient is the Pearson correlation, r which is defined as,

$$r = \frac{\sum(x_i - \bar{x})(y_i - \bar{y})}{\sqrt{\sum(x_i - \bar{x})^2 \sum(y_i - \bar{y})^2}} \quad (6.1)$$

where x_i is the input variables, \bar{x} is the mean value of input variables, y_i is the output variables and \bar{y} is the mean value of the output variables.

r^2 score: it is the regression score function, which determines how good a given fit is; it is defined as,

$$r^2(y, \hat{y}) = 1 - \frac{\sum_{i=1}^n (y_i - \hat{y}_i)^2}{\sum_{i=1}^n (y_i - \bar{y})^2} \quad (6.2)$$

where \hat{y}_i is the predicted value for the i th sample, y_i is the true value and \bar{y} is again the mean value of the output variables.

RMSE value: RMSE is the standard deviation of the residuals. This is a more quantitative metric compared to r^2 score. This is defined as,

$$RMSE(y, \hat{y}) = \sqrt{\frac{1}{n} \sum_{i=0}^{n-1} (y_i - \hat{y}_i)^2} \quad (6.3)$$

6.2.3 Hyperparameter Tuning

We have carried out hyperparameter tuning using GridSearchCV algorithm for the models except for RF. For RF, we have used RandomSearchCV algorithm. All the hyperparameters are listed in Table 6.2.

All the implemented codes, raw dataset and preprocessed dataset can be found at [https://github.com/BidhanChandra/ML EQE max Prediction](https://github.com/BidhanChandra/ML_EQE_max_Prediction)

6.3 Results and Discussions

6.3.1 Exploratory Data Analysis

EDA helps to understand the pattern within the data, pre-process the data for the ML part and find relevant parameters which influence the overall model efficiency, which includes calculation of Pearson correlation and visualization of heatmap between output and inputs also among the inputs. Fig. 6.1 (a) represents the correlation heatmap between variables and as well as with the output variable with a correlation value greater than 0.20. PLQY shows the highest positive correlation of 0.73 with the EQE_{max} while ΔE_{ST} shows a negative correlation of -0.39 with EQE_{max} , which is quite expected. Note that, this kind of correlation was not seen in earlier scientific literature, most likely due to the repetitive usage of the same input with varied output. Fig. 1 (b) represents further details into the relationship of PLQY with EQE_{max} . This figure suggests that although there is a one-to-one correlation between PLQY with EQE_{max} , a high PLQY does not guarantee high EQE_{max} .

Now, to analyze the effect of HOMO-LUMO offset, we find that even though there are systems with PLQY equal to 100%, like SpiroAc-TRZ, but high EQE_{max} ~37% become possible because of a high horizontal dipole ratio of 83%.³¹ High horizontal dipole ratio ensures good exciton transfer from HOST to GUEST. To find the actual effect of HOMO-LUMO offset, we argue that devices where LUMO offset (LUMO energy of HOST – LUMO energy of GUEST) is high, EQE_{max} is generally high if PLQY is large. This energy ordering further prevents any exciton transfer to the HOST from GUEST and improves the efficiency.

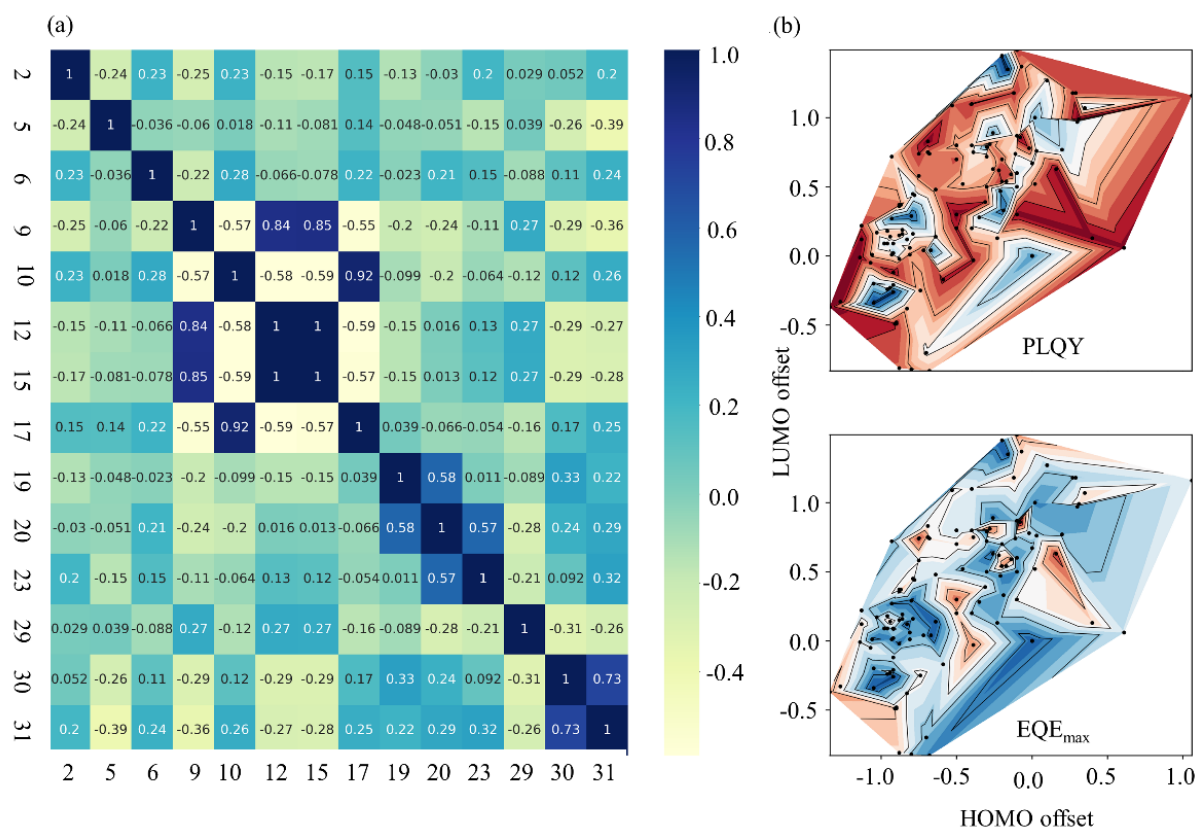


Figure 6.1: (a) Pearson correlation heatmap in between variables and with the EQE_{max} (index 31), only those variables are shown which have $|r| > 0.20$. (b) contour heatmap of PLQY and EQE_{max} with HOMO and LUMO offset.

Figure 6.2 represents the regression plot with the distribution of EQE_{max} with PLQY, ΔE_{ST} , -LUMO energy of HTL1 and -HOMO energy of ETL2. As we have mentioned earlier, a high value of PLQY does not guarantee a high value of EQE_{max}. PLQY has a very high distribution in the range of 80-100, but we found a very small distribution. Rather, PLQY distribution in the range of 60-80 produced a large distribution of EQE_{max} in the range of 10-20. $\Delta E_{ST} < 100$ meV always favors rISC and as a result, most of the high EQE_{max} systems have high distribution over the range 0.0-0.1 eV. However, there is also light distribution when $\Delta E_{ST} > 100$ meV. We believe that those systems may employ the spin-vibronic coupling mechanism to harness the excitons. The -LUMO energy of HTL1 is inversely correlated with the EQE_{max}. Higher LUMO energy is better for improved EQE_{max}. On the other hand, -HOMO energy of ETL2 is positively correlated with EQE_{max}, so that lower the HOMO energy, better is the EQE_{max}. HTL1 is connected to HIL/anode (in case of absence of HIL) and ETL2 is connected to the cathode. Lower HOMO energy contributes to the high triplet energy

of ETL2, which is favorable for electron transfer through the overall ETL layer and ceasing dissipation of excitons.

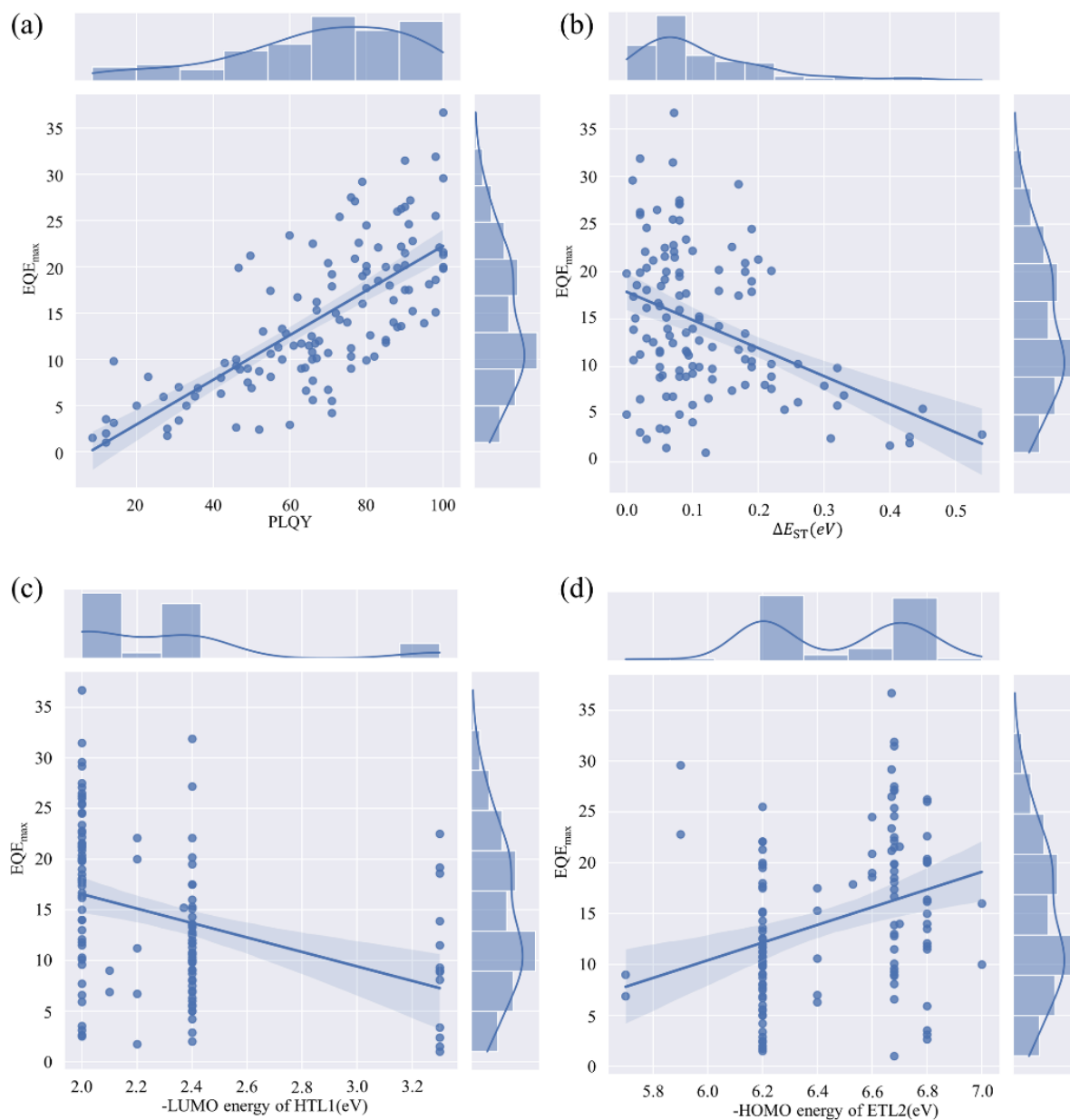


Figure 6.2: Regression plot of EQE_{max} vs (a) PLQY (b) ΔE_{ST} (c) -LUMO energy of HTL1 (d) -HOMO energy of ETL2.

6.3.2 Machine Learning

For the initial analysis of the data, we have first employed simple ML algorithms (Support Vector Regression, K-Nearest Neighbor and Decision Trees) to train the data and have tested the employed model against test data. The r^2 score and the

corresponding RMSE values for the models for both train and set are reported in Table 6.1.

Table 6.1: Performance metrics of SVR, DT and K-NN

ML Model	Reason for choice	r^2 score _{train}	r^2 score _{test}	RMSE _{train}	RMSE _{test}
Support Vector Regression (SVR)	Polynomial Regression	0.63 ± 0.05	0.34	4.72 ± 0.41	5.09
Decision Tree (DT)	Logic based approach	0.41 ± 0.15	-0.06	5.99 ± 1.05	6.46
K-NN (K=3) regression	Nonparametric method	0.39 ± 0.04	0.62	6.08 ± 0.54	3.88

With SVR, we have got a cross-validated r^2 score of 0.63 ± 0.04 for train set with a mean RMSE of 4.59, while for test set, we obtained r^2 score of 0.34 with RMSE of 5.09. It is quite clear that it highly overfits and thus performs very poorly for the test set. Although, in the high EQE_{\max} region, it performs well. However, in the low EQE_{\max} region, it fails quite miserably, even predicting a negative EQE_{\max} value, as evident from the Fig. S6.3. To extract further learning capability of SVR with more data, we have performed learning curve analysis. From Fig. 6.3, we can see that the improvement of the model stopped after 70 training examples and it reached the saturation. So, further improvement with increasing data points is not possible.

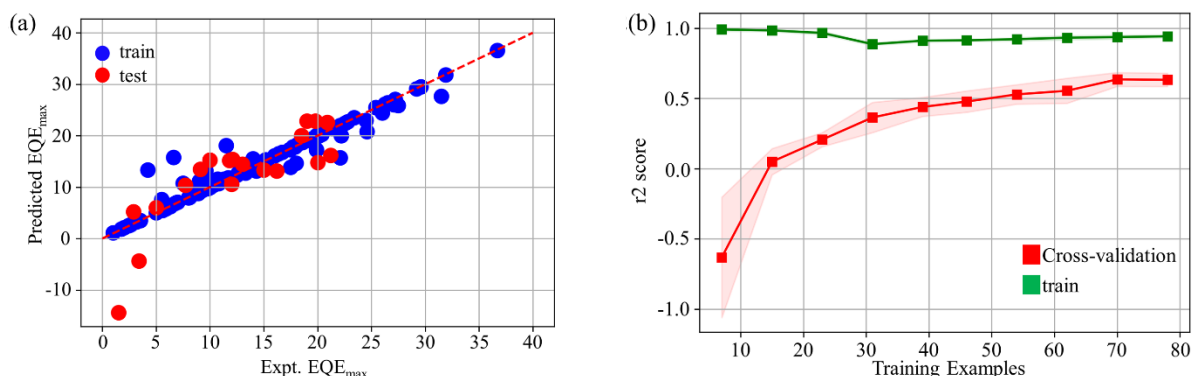


Figure 6.3: (a) r^2 score plot for SVR model (b) Learning curve for SVR model

In fact, the DT has also shown poor performance with the cross-validated r^2 score of 0.41 with a high variance of 0.15 for train set, while for test set it is -0.06 (Fig.

6.4(a)). Optimized DT has a maximum depth of 2. Because of such structure of the DT, outputs are parallel to X-axis with 4 distinct values (mean value of the samples of each leaf node). Basically, based on a given condition, a constant value has been assigned in each case. Such poor performance is also reflected in the RMSE values of $5.98 \pm 1.05/6.46$ for train and test set. With max. depth of 2, it has been decisive based on two input parameters: PLQY and -LUMO energy of HTL1 with feature importance of 0.89 and 0.11 (Fig. 6.4(b)).

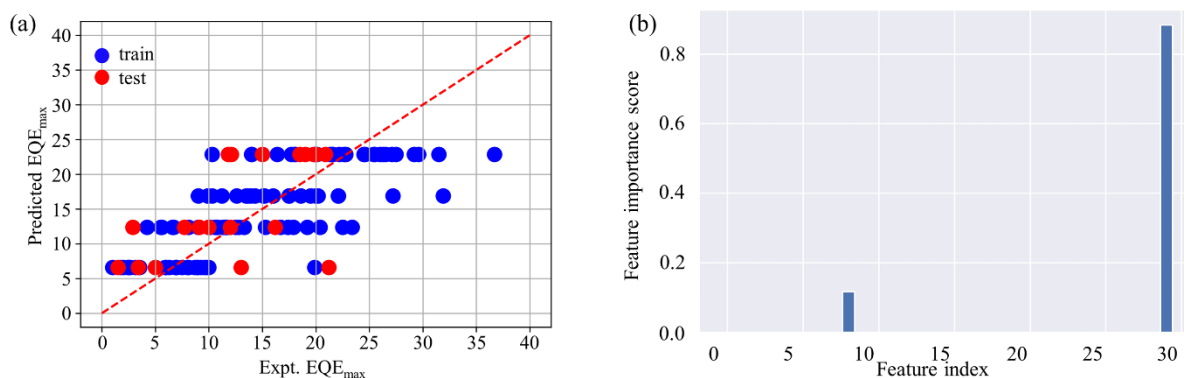


Figure 6.4: (a) r^2 score plot for DT regression model (b) Feature importance plot for the model

Now moving towards K-NN, we have scanned the optimum number of neighbors for regression and with neighbors=3, the model has performed the best (Fig. 6.5). With train set, it has produced cross-validated r^2 score of 0.39 ± 0.04 and 0.62 for test set and mean RMSE of $6.08 \pm 0.54/3.88$ over train/test set.

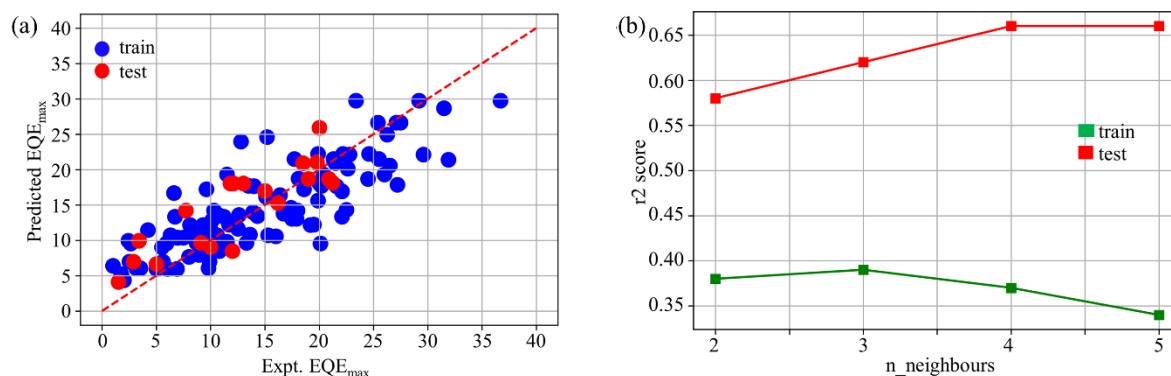


Figure 6.5: (a) r^2 score plot for K-NN regression model (b) Plot of hyperparameter tuning with $n_{\text{neighbour}}$ variation

As, we can see, all the above three models could not perform up to the expectations. We thus moved towards ensemble-based learning, where we have used DT as a base

learner (weak learner) model and through repetitive training, we have got better performance from these ensemble-based learning models. Figure 6.6 shows a schematic representation of the variations of ensemble-based learning. Generally, there are two major types of ensemble-based learning methods: (1) Bagging (2) Boosting. Bagging is parallel in nature and RF is an example of a bagging algorithm. With RF, we have got cross-validated r^2 score of 0.65 with a high variance of 0.12 for train set and for test set we have got very a high r^2 score of 0.74, which corresponds to mean RMSE of $4.59 \pm 0.37/3.18$ for train/test set. To get an insight into the employed model, we have plotted feature importance plot. It selects PLQY and ΔE_{ST} as the most important features with scores of 0.28 and 0.10 respectively. Note that, it has shown very little acceleration in the learning curve. In fact, the r^2 score for validation has improved by 0.02 going from 70 to 78 training examples.

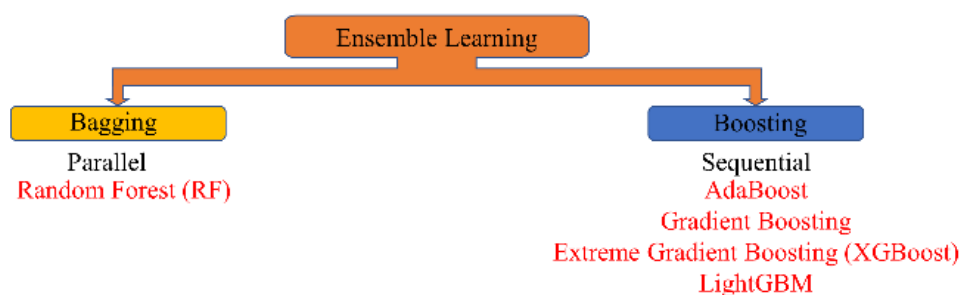


Figure 6.6: Schematic Representations of the variations of ensemble-based learning, their nature and used model under each class in this work

Furthermore, we have focused on boosting algorithms and have employed GB, AdaBoost, XGB and LightGBM model (Fig. 6.7-6.10).

Among them, GB has performed the best even surpassing the XGB efficiency (Figure 6.11). GB has provided a cross-validated r^2 score of 0.71, with a variance of 0.04 for train set. While for the test set, the r^2 score is 0.84. The model has also produced a low RMSE of $4.22 \pm 0.55/2.53$ for train/test set (Figure 6.12). A comparison of our work with related ML-based works on OLEDs is shown in Figure S10. Interestingly, XGB has performed with r^2 score of $0.70 \pm 0.03/0.70$ and RMSE of $4.30 \pm 0.46/3.44$ for train/test set (Fig. 6.10).

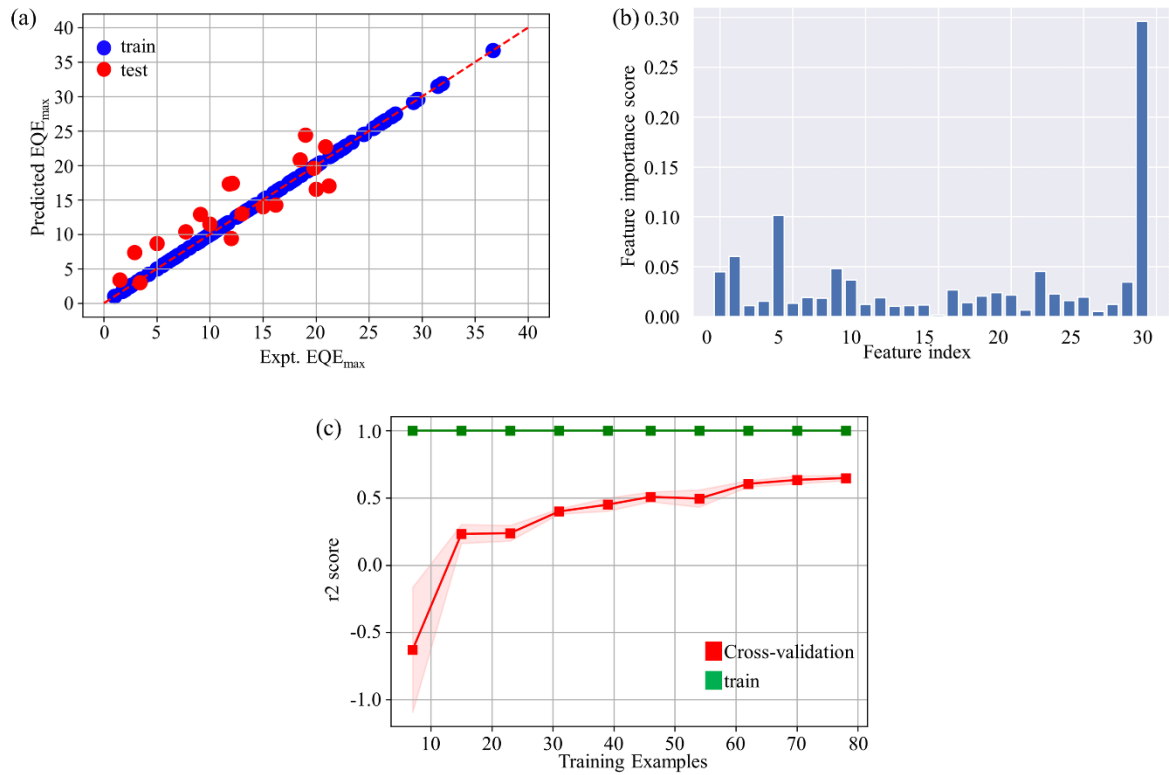


Figure 6.7: (a) r2 score plot for Random Forest regression model (b) Feature importance plot for RF model (c) Learning Curve for RF model

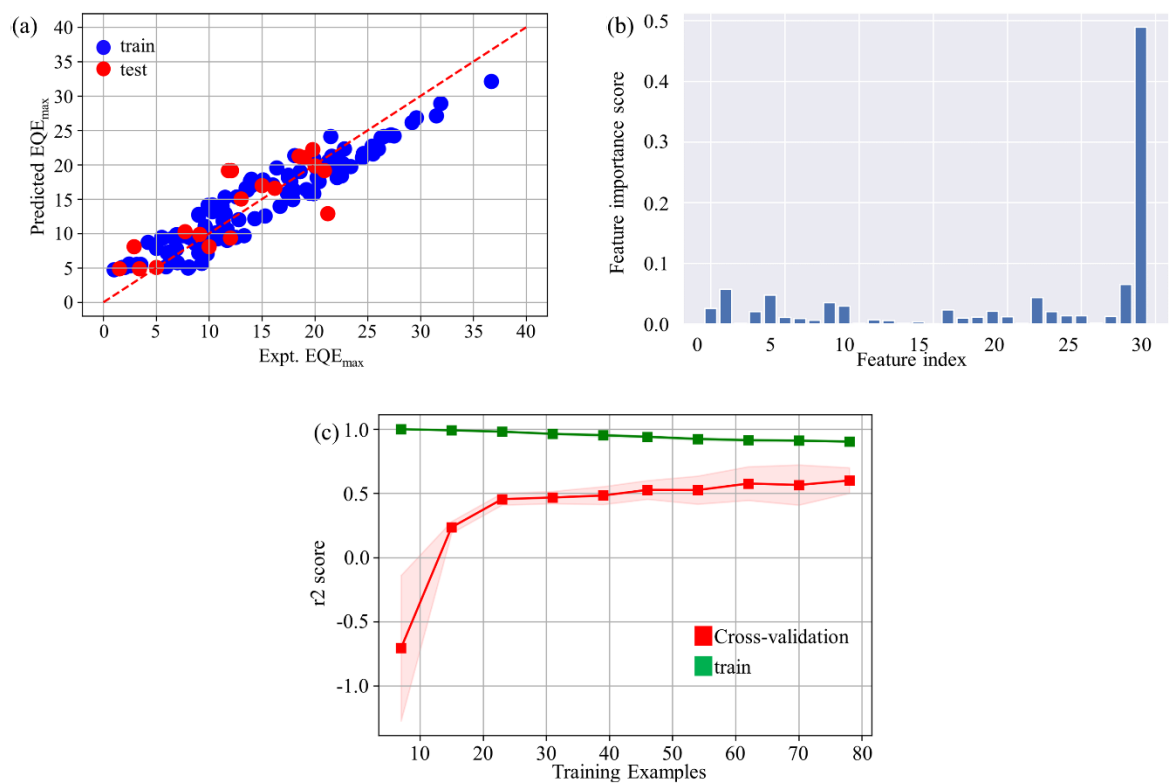


Figure 6.8: (a) r2 score plot for AdaBoost regression model (b) Feature importance plot for AdaBoost model (c) Learning Curve for AdaBoost model

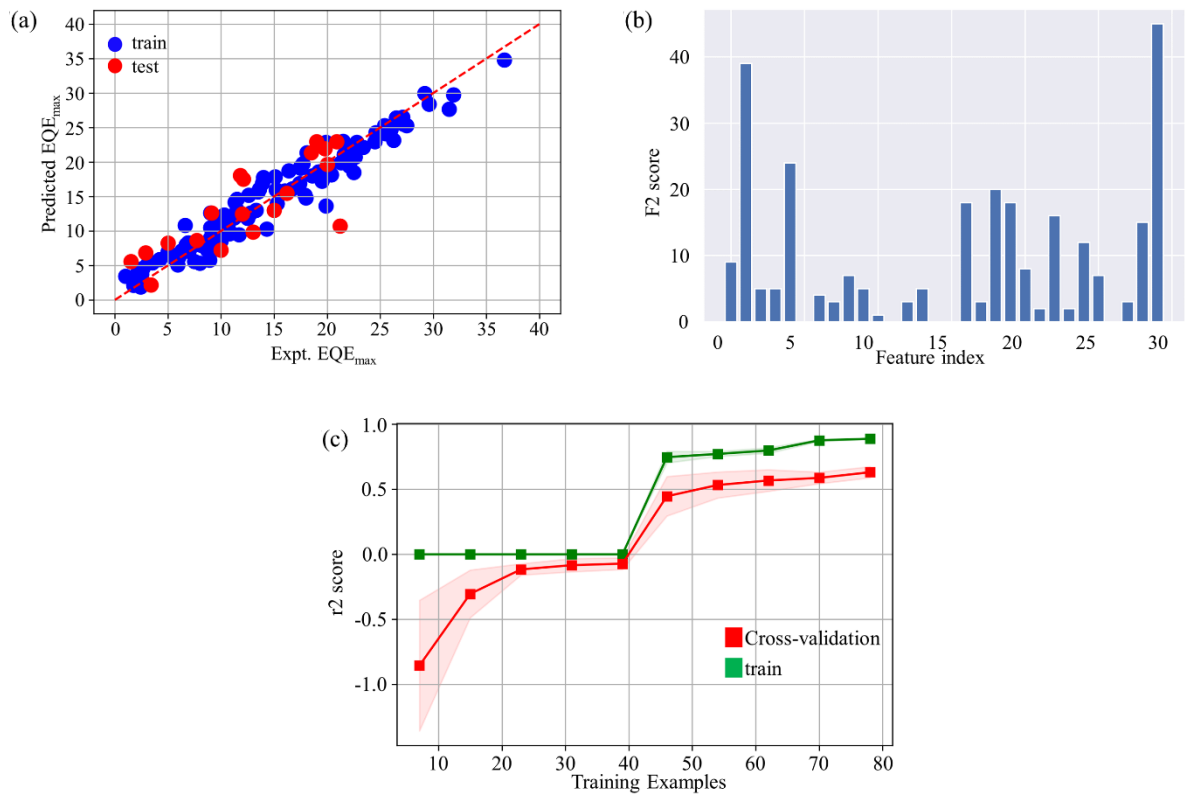


Figure 6.9: (a) r2 score plot for LightGBM regression model (b) Feature importance plot for LighGBM model (c) Learning Curve for LighGBM model

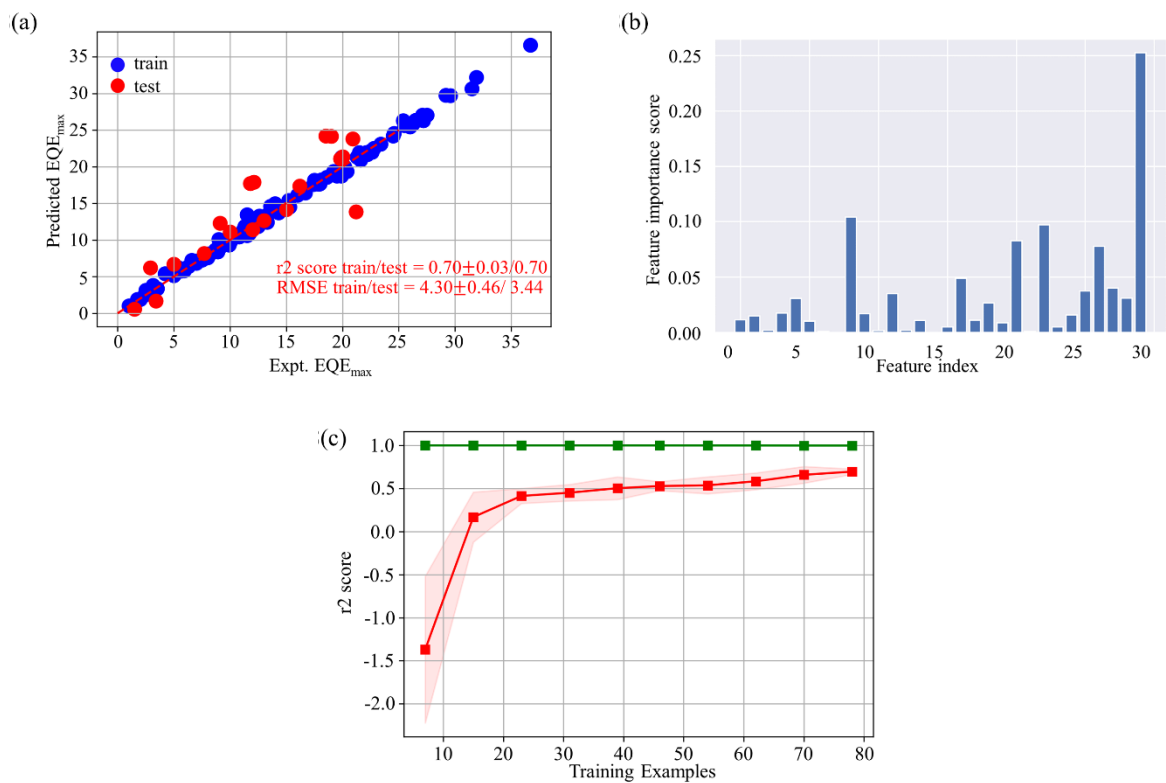


Figure 6.10: (a) r2 score plot for XGB regression model (b) Feature importance plot for XGB model (c) Learning Curve for XGB model.

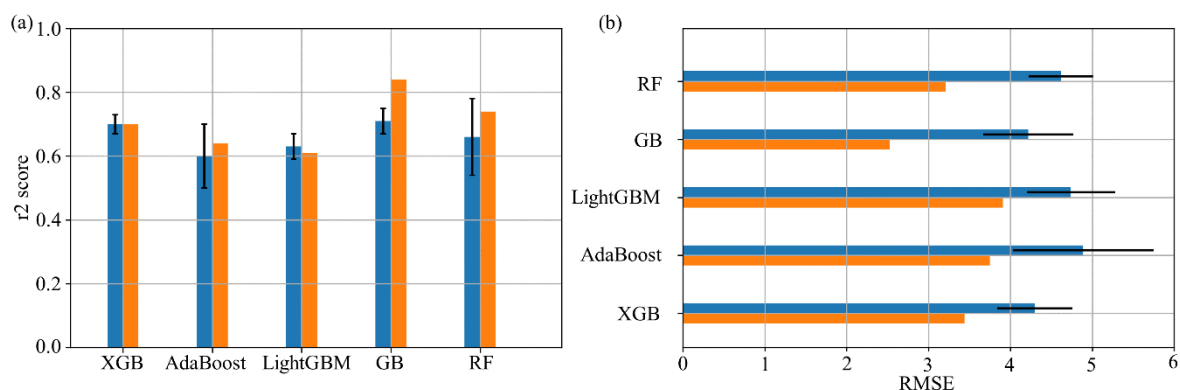


Figure 6.11: Comparison of GB, XGB, AdaBoost, LightGBM and RF with (a) r^2 score (b) RMSE. Blue bar indicates train set result (cross-validated); orange bar indicates test set result. Black line indicates the variance.

Generally, models with high performance are considered as black box. Therefore, we have performed again feature importance analysis for interpretability of the employed models. Feature importance score examines the effect of a certain feature on the reduction in the criterion used to split nodes in DTs.

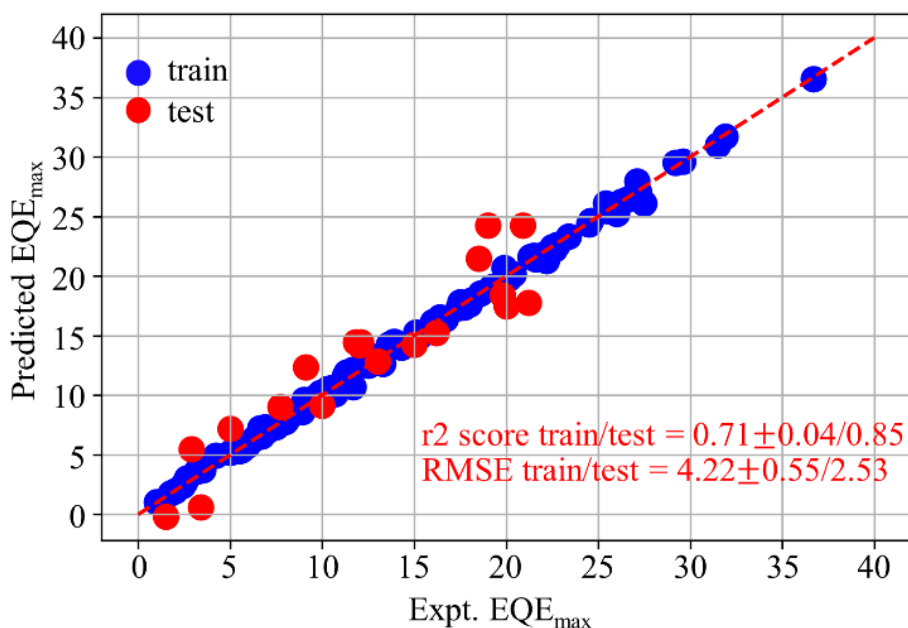


Figure 6.12: Train/ test metrics (r^2 score and RMSE) of GB Model. For train set, the evaluated metrics is the mean of cross-validation

In the case of XGB, PLQY has the highest score of 0.25 and -LUMO energy of HTL1 has the second-highest score of 0.10. While -LUMO energy of ETL1 and -HOMO energy of ETL2 ranks 3rd and 4th with scores of 0.097 and 0.078 respectively. Similarly,

for GB, PLQY ranks first with feature importance score of 0.54 and -LUMO energy of GUEST being 2nd with a score of 0.07 (Figure 6.13(a)). -LUMO energy of GUEST has positive correlation with the output, which indicates a lower LUMO energy is good for EQE_{max}. A low LUMO energy is good to hinder the reverse exciton transfer to the HOST and ceasing further dissipation of exciton. ΔE_{ST} ranks 3rd with feature importance score of 0.054. Lower ΔE_{ST} obviously guarantees an efficient rISC, which is important for better EQE_{max}. Apart from good performance, it still has better potential. Learning curve for both GB and XGB is still ascending. The validation for r^2 score has increased by 0.06 (0.65 to 0.71) when the number of training examples increased from 70 to 78 (Fig. 6.13(b)) for GB. The main point of this work is that with so many models employed, if one must rely on the best score among the employed models, learning curve for GB has the highest potential among the models. However, training more examples is beyond the scope of this work.

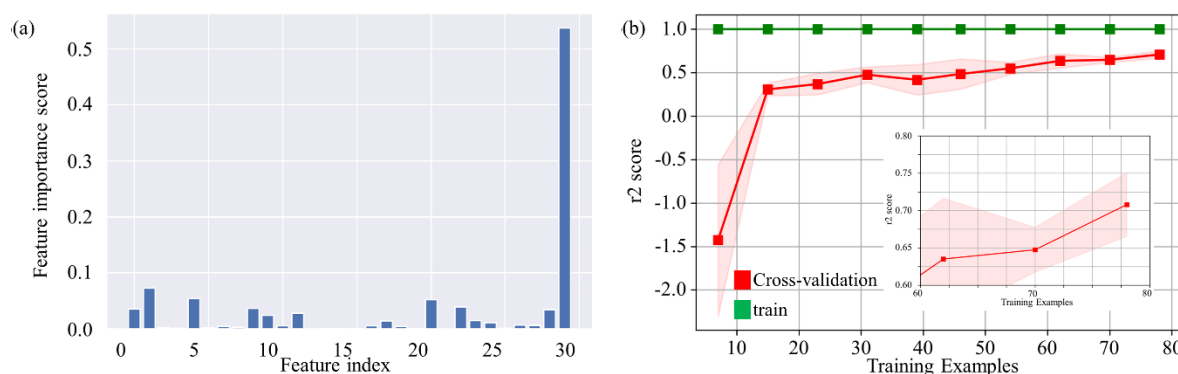


Figure 6.13: a) Feature importance plot (b) Learning curve for GB.

6.4 Conclusions

In this chapter, we have developed ML models for the prediction of EQE_{max} in TADF-based OLEDs, which are general to any TADF-based chromophore, irrespective of their emission range and device architecture. We have created a database of 123 TADF devices consisting of 30 features, which can be obtained from experiments (devoid of any further theoretical calculations). Initial data analysis has shown that among the features PLQY, ΔE_{ST} , -LUMO energy of HTL1 and -HOMO energy of ETL2 manifested a high correlation with EQE_{max}, with $|r| > 0.20$. We have employed very simple machine learning models involving SVR, K-NN and DT. These models have failed miserably to predict any better output. Subsequently, we have employed

ensemble-based learning models, which work on the gradual improvement of the weak learning models like DT. We have used both bagging (RF) and boosting (GB, AdaBoost, XGB, LightGBM) algorithms. Note that, while the bagging is parallel in nature and the boosting works on a sequential basis. Finally, among the employed ensemble-based models, GB has performed the best with r^2 score of $0.71 \pm 0.04/0.84$ and RMSE of $4.22 \pm 0.55/2.53$ for train/test set, which is quite good with respect to the current state-of-the-art (SOTA) (Figure S9). Being a tree-based model, it has given high importance to PLQY and -LUMO energy of GUEST with feature importance scores of 0.54 and 0.07. Even the learning curve is still upwards, which proves the model can perform better with more train data points, however, that is beyond the scope of this work. The main advantage of this work is that the experimentalists can easily deploy this model with features readily accessible to them with accessible cloud computation facility and further help the models by improving the database. The main point and we believe that this work will surely stand out in prediction of efficiency in the field of TADF-based OLEDs in very near future.

Table 6.2: Hyperparameters for the employed models

Model	Hyperparameters
SVR	'C': 0.01, 'degree': 3, 'gamma': 0.6, 'kernel': 'poly'
DT	'max_depth': 2, 'min_samples_leaf': 20
kNN Regression	n_neighbors=3
AdaBoost	'learning_rate': 1.0, 'n_estimators': 399
GB	'learning_rate': 0.2, 'max_depth': 20, 'min_samples_split': 0.5, 'n_estimators': 150
XGB	'learning_rate': 0.2, 'max_depth': 3, 'min_leaf_split': 0.1, 'min_samples_split': 0.1, 'n_estimators': 90, 'reg_alpha': 0.0766, 'reg_lambda': 1.0
LightGBM	'boosting_type': 'gbdt', 'learning_rate': 0.2, 'max_depth': 3, 'n_estimators': 90, 'reg_alpha': 0.02, 'reg_lambda': 1.0
RF	'bootstrap': False, 'max_depth': 20, 'max_features': 'sqrt', 'min_samples_leaf': 1, 'min_samples_split': 2, 'n_estimators': 500

Bibliography

- [1] A. Endo, K. Sato, K. Yoshimura, T. Kai, A. Kawada, H. Miyazaki, C. J. A. P. L. Adachi. **2011**, 98, 42.
- [2] S. Youn Lee, T. Yasuda, H. Nomura, C. Adachi *Applied Physics Letters*. **2012**, 101, 093306.
- [3] Y. Tao, K. Yuan, T. Chen, P. Xu, H. Li, R. Chen, C. Zheng, L. Zhang, W. Huang *Advanced Materials*. **2014**, 26, 7931-7958.
- [4] T. Hatakeyama, K. Shiren, K. Nakajima, S. Nomura, S. Nakatsuka, K. Kinoshita, J. Ni, Y. Ono, T. Ikuta. **2016**, 28, 2777-2781.
- [5] X. K. Chen, Y. Tsuchiya, Y. Ishikawa, C. Zhong, C. Adachi, J. L. Bredas *Adv Mater*. **2017**, 29.
- [6] M. K. Etherington, J. Gibson, H. F. Higginbotham, T. J. Penfold, A. P. J. N. c. Monkman. **2016**, 7, 1-7.
- [7] J. Gibson, A. P. Monkman, T. J. J. C. Penfold. **2016**, 17, 2956.
- [8] E. Hontz, W. Chang, D. N. Congreve, V. Bulović, M. A. Baldo, T. Van Voorhis *The Journal of Physical Chemistry C*. **2015**, 119, 25591-25597.
- [9] P. K. Samanta, D. Kim, V. Coropceanu, J.-L. Brédas *Journal of the American Chemical Society*. **2017**, 139, 4042-4051.
- [10] R. Gómez-Bombarelli, J. Aguilera-Iparraguirre, T. D. Hirzel, D. Duvenaud, D. Maclaurin, M. A. Blood-Forsythe, H. S. Chae, M. Einzinger, D.-G. Ha, T. Wu, G. Markopoulos, S. Jeon, H. Kang, H. Miyazaki, M. Numata, S. Kim, W. Huang, S. I. Hong, M. Baldo, R. P. Adams, A. Aspuru-Guzik *Nature Materials*. **2016**, 15, 1120-1127.
- [11] N. Meftahi, M. Klymenko, A. J. Christofferson, U. Bach, D. A. Winkler, S. P. Russo *npj Computational Materials*. **2020**, 6, 166.
- [12] C.-Y. Chan, L.-S. Cui, J. U. Kim, H. Nakanotani, C. Adachi *Advanced Functional Materials*. **2018**, 28, 1706023.
- [13] K. Zhao, Ö. H. Omar, T. Nematiram, D. Padula, A. Troisi *Journal of Materials Chemistry C*. **2021**, 9, 3324-3333.
- [14] Y. Shu, B. G. Levine *The Journal of Chemical Physics*. **2015**, 142, 104104.
- [15] M.-H. Lee *Physical Chemistry Chemical Physics*. **2020**, 22, 16378-16386.
- [16] M. Liu, Y. Seino, D. Chen, S. Inomata, S. J. Su, H. Sasabe, J. Kido *Chem Commun (Camb)*. **2015**, 51, 16353-16356.

- [17] S. Y. Lee, T. Yasuda, Y. S. Yang, Q. Zhang, C. Adachi *Angew Chem Int Ed Engl.* **2014**, *53*, 6402-6406.
- [18] C. Duan, J. Li, C. Han, D. Ding, H. Yang, Y. Wei, H. Xu *Chemistry of Materials.* **2016**, *28*, 5667-5679.
- [19] I. Lee, J. Y. Lee *Organic Electronics.* **2016**, *29*, 160-164.
- [20] Y. J. Cho, K. S. Yook, J. Y. Lee *Scientific Reports.* **2015**, *5*, 7859.
- [21] Y. Kitamoto, T. Namikawa, D. Ikemizu, Y. Miyata, T. Suzuki, H. Kita, T. Sato, S. Oi *Journal of Materials Chemistry C.* **2015**, *3*, 9122-9130.
- [22] Q. Zhang, B. Li, S. Huang, H. Nomura, H. Tanaka, C. Adachi *Nature Photonics.* **2014**, *8*, 326-332.
- [23] Y. J. Cho, B. D. Chin, S. K. Jeon, J. Y. Lee *Advanced Functional Materials.* **2015**, *25*, 6786-6792.
- [24] Y. Liu, G. Xie, K. Wu, Z. Luo, T. Zhou, X. Zeng, J. Yu, S. Gong, C. Yang *Journal of Materials Chemistry C.* **2016**, *4*, 4402-4407.
- [25] D.-Y. Chen, W. Liu, C.-J. Zheng, K. Wang, F. Li, S. L. Tao, X.-M. Ou, X.-H. Zhang *ACS Applied Materials & Interfaces.* **2016**, *8*, 16791-16798.
- [26] T. Takahashi, K. Shizu, T. Yasuda, K. Togashi, C. Adachi *Science and Technology of Advanced Materials.* **2014**, *15*, 034202.
- [27] D. R. Lee, S.-H. Hwang, S. K. Jeon, C. W. Lee, J. Y. Lee *Chemical Communications.* **2015**, *51*, 8105-8107.
- [28] K. Suzuki, S. Kubo, K. Shizu, T. Fukushima, A. Wakamiya, Y. Murata, C. Adachi, H. Kaji *Angewandte Chemie International Edition.* **2015**, *54*, 15231-15235.
- [29] R. Komatsu, H. Sasabe, Y. Seino, K. Nakao, J. Kido *Journal of Materials Chemistry C.* **2016**, *4*, 2274-2278.
- [30] W.-L. Tsai, M.-H. Huang, W.-K. Lee, Y.-J. Hsu, K.-C. Pan, Y.-H. Huang, H.-C. Ting, M. Sarma, Y.-Y. Ho, H.-C. Hu, C.-C. Chen, M.-T. Lee, K.-T. Wong, C.-C. Wu *Chemical Communications.* **2015**, *51*, 13662-13665.
- [31] T.-A. Lin, T. Chatterjee, W.-L. Tsai, W.-K. Lee, M.-J. Wu, M. Jiao, K.-C. Pan, C.-L. Yi, C.-L. Chung, K.-T. Wong, C.-C. Wu *Advanced Materials.* **2016**, *28*, 6976-6983.
- [32] W. Liu, C.-J. Zheng, K. Wang, Z. Chen, D.-Y. Chen, F. Li, X.-M. Ou, Y.-P. Dong, X.-H. Zhang *ACS Applied Materials & Interfaces.* **2015**, *7*, 18930-18936.
- [33] K. Shizu, J. Lee, H. Tanaka, H. Nomura, T. Yasuda, H. Kaji, C. Adachi *Pure and Applied Chemistry.* **2015**, *87*, 627-638.

- [34] D. R. Lee, M. Kim, S. K. Jeon, S.-H. Hwang, C. W. Lee, J. Y. Lee *Advanced Materials*. **2015**, *27*, 5861-5867.
- [35] G. Méhes, H. Nomura, Q. Zhang, T. Nakagawa, C. Adachi *Angewandte Chemie International Edition*. **2012**, *51*, 11311-11315.
- [36] I. H. Lee, W. Song, J. Y. Lee *Organic Electronics*. **2016**, *29*, 22-26.
- [37] K. Albrecht, K. Matsuoka, K. Fujita, K. Yamamoto *Angewandte Chemie International Edition*. **2015**, *54*, 5677-5682.
- [38] S. Y. Lee, T. Yasuda, H. Komiyama, J. Lee, C. Adachi *Advanced Materials*. **2016**, *28*, 4019-4024.
- [39] S. Y. Lee, T. Yasuda, I. S. Park, C. Adachi *Dalton Transactions*. **2015**, *44*, 8356-8359.
- [40] P. Data, P. Pander, M. Okazaki, Y. Takeda, S. Minakata, A. P. Monkman *Angewandte Chemie International Edition*. **2016**, *55*, 5739-5744.
- [41] H. Wang, L. Xie, Q. Peng, L. Meng, Y. Wang, Y. Yi, P. Wang *Advanced Materials*. **2014**, *26*, 5198-5204.
- [42] P. Rajamalli, N. Senthilkumar, P. Gandeepan, P.-Y. Huang, M.-J. Huang, C.-Z. Ren-Wu, C.-Y. Yang, M.-J. Chiu, L.-K. Chu, H.-W. Lin, C.-H. Cheng *Journal of the American Chemical Society*. **2016**, *138*, 628-634.
- [43] Y. Wada, K. Shizu, S. Kubo, K. Suzuki, H. Tanaka, C. Adachi, H. Kaji *Applied Physics Letters*. **2015**, *107*, 183303.
- [44] H. Kaji, H. Suzuki, T. Fukushima, K. Shizu, K. Suzuki, S. Kubo, T. Komino, H. Oiwa, F. Suzuki, A. Wakamiya, Y. Murata, C. Adachi *Nature Communications*. **2015**, *6*, 8476.
- [45] H. Hirai, K. Nakajima, S. Nakatsuka, K. Shiren, J. Ni, S. Nomura, T. Ikuta, T. Hatakeyama *Angewandte Chemie International Edition*. **2015**, *54*, 13581-13585.
- [46] H. Tanaka, K. Shizu, H. Miyazaki, C. Adachi *Chemical Communications*. **2012**, *48*, 11392-11394.
- [47] K. Wu, T. Zhang, L. Zhan, C. Zhong, S. Gong, N. Jiang, Z.-H. Lu, C. Yang *Chemistry – A European Journal*. **2016**, *22*, 10860-10866.
- [48] D.-G. Chen, T.-C. Lin, Y.-A. Chen, Y.-H. Chen, T.-C. Lin, Y.-T. Chen, P.-T. Chou *The Journal of Physical Chemistry C*. **2018**, *122*, 12215-12221.
- [49] G. Xie, X. Li, D. Chen, Z. Wang, X. Cai, D. Chen, Y. Li, K. Liu, Y. Cao, S.-J. Su *Advanced Materials*. **2016**, *28*, 181-187.

- [50] K. Shizu, H. Noda, H. Tanaka, M. Taneda, M. Uejima, T. Sato, K. Tanaka, H. Kaji, C. Adachi *The Journal of Physical Chemistry C*. **2015**, *119*, 26283-26289.
- [51] J. Lee, K. Shizu, H. Tanaka, H. Nakanotani, T. Yasuda, H. Kaji, C. Adachi *Journal of Materials Chemistry C*. **2015**, *3*, 2175-2181.
- [52] H. Tanaka, K. Shizu, H. Nakanotani, C. Adachi *Chemistry of Materials*. **2013**, *25*, 3766-3771.
- [53] Y. Xiang, S. Gong, Y. Zhao, X. Yin, J. Luo, K. Wu, Z.-H. Lu, C. Yang *Journal of Materials Chemistry C*. **2016**, *4*, 9998-10004.
- [54] Q. Zhang, H. Kuwabara, W. J. Potscavage, S. Huang, Y. Hatae, T. Shibata, C. Adachi *Journal of the American Chemical Society*. **2014**, *136*, 18070-18081.
- [55] J. Li, T. Nakagawa, J. MacDonald, Q. Zhang, H. Nomura, H. Miyazaki, C. Adachi *Advanced Materials*. **2013**, *25*, 3319-3323.
- [56] P. Chen, L.-P. Wang, W.-Y. Tan, Q.-M. Peng, S.-T. Zhang, X.-H. Zhu, F. Li *ACS Applied Materials & Interfaces*. **2015**, *7*, 2972-2978.
- [57] S. Wang, X. Yan, Z. Cheng, H. Zhang, Y. Liu, Y. Wang *Angewandte Chemie International Edition*. **2015**, *54*, 13068-13072.
- [58] W. Zeng, H.-Y. Lai, W.-K. Lee, M. Jiao, Y.-J. Shiu, C. Zhong, S. Gong, T. Zhou, G. Xie, M. Sarma, K.-T. Wong, C.-C. Wu, C. Yang *Advanced Materials*. **2018**, *30*, 1704961.
- [59] P. Rajamalli, N. Senthilkumar, P. Y. Huang, C. C. Ren-Wu, H. W. Lin, C. H. Cheng *Journal of the American Chemical Society*. **2017**, *139*, 10948-10951.
- [60] J. W. Sun, K.-H. Kim, C.-K. Moon, J.-H. Lee, J.-J. Kim *ACS Applied Materials & Interfaces*. **2016**, *8*, 9806-9810.
- [61] Y. Wada, S. Kubo, H. Kaji *Advanced Materials*. **2018**, *30*, 1705641.
- [62] Z. Cai, X. Wu, H. Liu, J. Guo, D. Yang, D. Ma, Z. Zhao, B. Z. Tang *Angewandte Chemie International Edition*. **2021**, *60*, 23635-23640.
- [63] W. Zeng, T. Zhou, W. Ning, C. Zhong, J. He, S. Gong, G. Xie, C. Yang *Advanced Materials*. **2019**, *31*, 1901404.
- [64] Z. Wang, X. Zhu, S. Zhang, L. Xu, Z. Zhao, G. He *Advanced Optical Materials*. **2021**, *9*, 2001764.
- [65] Q. Li, J. Hu, J. Lv, X. Wang, S. Shao, L. Wang, X. Jing, F. Wang *Angewandte Chemie International Edition*. **2020**, *59*, 20174-20182.
- [66] R. Furue, K. Matsuo, Y. Ashikari, H. Ooka, N. Amanokura, T. Yasuda *Advanced Optical Materials*. **2018**, *6*, 1701147.

- [67] J. Liang, C. Li, Y. Cui, Z. Li, J. Wang, Y. Wang *Journal of Materials Chemistry C*. **2020**, *8*, 1614-1622.
- [68] T. Ohsawa, H. Sasabe, T. Watanabe, K. Nakao, R. Komatsu, Y. Hayashi, Y. Hayasaka, J. Kido *Advanced Optical Materials*. **2019**, *7*, 1801282.
- [69] T. Yang, Z. Cheng, Z. Li, J. Liang, Y. Xu, C. Li, Y. Wang *Advanced Functional Materials*. **2020**, *30*, 2002681.
- [70] M. Y. Wong, E. Zysman-Colman *Advanced Materials*. **2017**, *29*, 1605444.
- [71] T. Huang, W. Jiang, L. Duan *Journal of Materials Chemistry C*. **2018**, *6*, 5577-5596.
- [72] Z. Yang, Z. Mao, Z. Xie, Y. Zhang, S. Liu, J. Zhao, J. Xu, Z. Chi, M. P. Aldred *Chemical Society Reviews*. **2017**, *46*, 915-1016.

7 Summary and Future Outlook

7.1 Retrospect

The past many years have witnessed an incredible growth in the field of triplet exciton harvesting. Due to its long lifetime and low energy, triplet exciton harvesting has huge potential to improve the efficiency and performance of organic optoelectronic devices, such as solar cells and light emitting diodes (room temperature phosphorescence or thermally activated delayed fluorescence) by enabling the use of photo generated excitons. Apart from that, triplet excitons can also be utilized for sensitization purposes, such as photodynamic treatment (PDT), photoinduced hydrogen synthesis from water, triplet-triplet annihilation (TTA), up conversion, and triplet energy transfer.

The past decade has also seen a huge growth in the theoretical exploration in the field of triplet exciton harvesting. This exploration can be divided into two major categories:

- (1) A better understanding of the mechanistic pathways of how systems harvest triplet excitons.
- (2) Searching the chemical space for better molecular design.

As we have described in the previous five work chapters, our contribution to this discipline was to conceptualise the mechanical pathways and create novel systems and provide a data-driven approach to screen OLED devices with good device efficiency. In the concluding chapter of the thesis, we recollect and summarize the key findings of our computational studies through a simple question-answer format. Also, in the next section, we mention some open questions that can be asked in the field of triplet exciton harvesting, which will provide a roadmap for future studies.

The first question that we asked is, “*What is the reverse intersystem crossing mechanism in a thermally activated delayed fluorescence molecule?*”

In this context, we have explored the intersystem crossing mechanisms of boron-based donor-spiro-acceptor organic molecule. Given that the donor and acceptor moieties are arranged approximately perpendicularly, the HOMO and LUMO are spatially separated, and the compound displays charge transfer (CT) transitions. Both the S_1 and T_1 excited states, which are CT in nature, localise the electron and hole wave functions on the acceptor and donor units, respectively. T_2 , which has locally excited structure (i.e., both electron and hole wave functions are localised on an acceptor unit) lies just above the T_1 state. As both S_1 and T_1 are CT states, the spin-orbit coupling matrix element between them is quite minimal. The rISC process from the T_1 state to the S_1 level is made possible by a nearby local excited triplet state (T_2), which is shown by our simulation of quantum dynamics and time-dependent density functional theory results. When there is less energy difference between the T_1 and T_2 states, the rISC is enhanced.

Once we explore the rISC mechanism, the second question we asked is, “*How simultaneously is room temperature phosphorescence and thermally activated delayed fluorescence possible?*”

We have answered the question from the lens of two different molecular architectures (mechanochromic luminescent material and PmDI derivatives) and provided microscopic insights into making better molecules.

One of the most intriguing prospects for the next generation of efficient OLEDs is the use of mechanochromic luminescent (MCL) materials, which alter their behaviour when subjected to external stimuli. Recently, mechanochromic luminescence was described for a donor-acceptor-donor (D-A-D) triad, containing two phenothiazine units, separated by a dibenzo[*a,j*]phenazine motif. The D units' conformational flipping determines the emissive routes that the triad will adopt, ranging from phosphorescence to TADF. In chapter 3, we have investigated the conformation-dependent photophysical behaviour of this trio using computations for the ground and excited states. Examining the ground state, excited states, and factors affecting the reverse ISC crossing rates associated with the relative orientation of the D and A units, we determine the effect of conformational changes on their photophysical properties.

Our results show that the axial orientation of both donor groups enhances the overlap between HOMO and LUMO. Wide singlet-triplet gaps are produced as a result, which fuels phosphorescence emission. Nevertheless, the equatorial orientation of the donor groups is reduced to make it simpler for rISC to activate the TADF of the conformers. The impact of different geometrical features on the photophysical properties of the conformers is also highlighted. In order to limit the population difference among conformers and enhance TADF efficiency, we also show how to functionalize the triad.

The second system, we looked at a pyromellitic diimide derivative (CzPhPmDI) that demonstrates both RTP and TADF. We have also looked at CzPhPmDI with a methyl spacer and a heavy atom replaced (on the donor and acceptor) for improved RTP and TADF emissions. In the ideal form of CzPhPmDI, the phenyl spacer is not quite perpendicular to the donor and acceptor, and the dihedral angle is very near to 60° . The singlet-triplet gap (ΔE_{ST}) first grows as the dihedral angle steadily increases (becoming increasingly perpendicular to both Cz and PmDI), as demonstrated by the dihedral angle-dependent examinations of excited state parameters (spacer is nearly perpendicular). When Me is substituted on the spacer (in CzMe₂PhPmDI), the spacer becomes perpendicular to both the Cz and PmDI groups. The ΔE_{ST} rises because S₁ and T₁ have different excitation properties. The spacer then becomes more coplanar with the Cz and PmDI units as a result, creating a twisted intramolecular charge transfer (TICT) state that ultimately leads to TADF with red-shifted emission. For effective RTP and TADF, Br substitution on PmDI enhances intersystem and reverse intersystem crossing, whereas heavy-atom substitution on the donor has no impact on the characteristics of the excited state.

We have not limited ourselves to light-emission applications. Triplet excitons can also help in organic photocatalytic reactions by sensitization. We know, thioxanthenes are an excellent class of triplet photosensitizers. But different thioxanthone derivatives show differences in their triplet harvesting ability. So, the third question we asked is, *“why do substitution with groups having a positive mesomeric effect on thioxanthone and 3 or 3' position harvest triplet excitons efficiently than unsubstituted thioxanthone or thioxanthone with similar substitution but at 2 or 2' positions?”*

Our results show that the S₀ to S₁ transition for thioxanthone and its derivatives has a strong oscillator strength since the S₁ and T₁ states are both expected to be of the type π - π^* . Major triplet exciton conversion is produced by the intersystem crossover

(ISC) channel between the S_1 ($^1\pi - \pi^*$) and high energy $^3n-\pi^*$ states. Moreover, the ISC channel has competition from the radiative and non-radiative channels from S_1 to S_0 , which reduces the effectiveness of triplet harvesting. Thioxanthenes with OMe (Me=Methyl) or F substitution at 2 or 2' sites are not energetically viable for the ISC channel, resulting in a slow intersystem crossing (ISC) quantum yield. With the unsubstituted thioxanthone and for isopropyl substitution at the 2' position, the S_1-T_1 gap is highly positive, which results in a lower triplet harvesting efficiency.

To have an application, we need to build technologies around triplet excitons and the dissipation of excitons in such devices is a challenging issue, which limits the overall device efficiency. Screening devices with good efficiency is still a major problem. In this context, the final question we asked is, “*How to screen devices with a higher efficiency, can we use a data-driven approach in this case?*”

Data-driven analysis is emerging as the fourth paradigm of research (the other three being computational, theoretical, and empirical). To predict the device efficiency (EQE_{max}), we employed ML models on 30 features of 123 examples, collected from the literature. Gradient Boosting (GB), an ensemble learning model, has been shown to be capable of predicting EQE_{max} , with a r^2 score of $0.71 \pm 0.04 / 0.84$ and a low RMSE of $4.22 \pm 0.55 / 2.53$ for the train/test set. The GB model is the most effective model that can highlight the effects of device architecture and anticipate TADF chromophores of any emissive range, according to the state-of-the-art (SOTA).

7.2 Prospects

Future research could spread in a variety of ways from this point. By exploring new types of experiments, speeding up the rate of discovery, and expediting data processing, artificial intelligence (AI) has the potential to completely transform the ongoing research in the field of triplet exciton harvesting. One of the areas where AI can play a role in this field is the molecular design. It can be difficult to find novel chemical compounds with desirable features, yet it has vital applications, like molecules with higher photocatalytic activity or molecules having a higher internal quantum efficiency (IQE). A variety of intriguing solutions have been developed to deal with this problem as a result of recent advancements in the creation of deep

generative models. A fresh approach to the issue of chemical synthesis is provided by deep generative models for graph-structured data. By optimizing differentiable models that produce molecular graphs directly, it is feasible to avoid costly search techniques in the discrete and huge space of chemical structures.